

UNIVERSITÀ DEGLI STUDI DI MILANO-BICOCCA

DOCTORAL THESIS

**Toward the first neutrino mass measurement
of Holmes**

Author:
Matteo BORGHESI

Supervisor:
Prof Angelo Enrico Lodovico
NUCCIOTTI

CORSO DI DOTTORATO IN FISICA E ASTRONOMIA

CICLO XXXIV

Department of Physics "G. Occhialini"

April 4, 2022

Per tutti i fenomeni di incapacità¹

¹come me

UNIVERSITÀ DEGLI STUDI DI MILANO-BICOCCA

Abstract

Department of Physics "G. Occhialini"

CORSO DI DOTTORATO IN FISICA E ASTRONOMIA, ciclo XXXIV

Toward the first neutrino mass measurement of Holmes

by Matteo BORGHESI

The absolute mass of neutrinos is one of the most important riddles yet to be solved, since it has many implications in Particle Physics and Cosmology. By tackling this issue, we will begin to shed light on a very crucial matter: what lies beyond the Standard Model (SM) of particle physics. In particular, its value will help to discriminate between many theories, from the ones related to the mass generation mechanisms to the one related to the cosmological evolution of large scale structure.

The only model independent method of measuring the neutrino mass is based on the kinematic analysis of the beta or the electron capture (EC) decay, which only assumes momentum and energy conservation. Many experiments are pursuing this goal, adopting a wide range of techniques and pushing each of them towards their technical limits.

Holmes is an ERC project started in 2014, which is currently being set up in the cryogenic laboratory of the University of Milano Bicocca. It will perform a direct measurement of the neutrino mass with a sensitivity of the order of 1 eV. In addition, it will prove the scalability of this technique to a next generation experiment that might go beyond the current expected sensitivity of the state of the art experiment, KATRIN.

In order to reach its goal sensitivity, Holmes will use 1000 low temperature microcalorimeters, each implanted with an activity of 300 Bq of ^{163}Ho , performing thus a calorimetric measurement.

In a calorimetric measurement of the electron capture (EC) decay of ^{163}Ho , all the energy is measured except for the fraction carried away by the neutrino. The energy measured, indicated as de-excitation energy, is mostly emitted in the form of Auger electrons from the relaxation of the excited daughter Dy atom.

The calorimetric spectrum of the Ho is composed of several lorentzian-shaped peaks, each one with energy equal to the binding energy of the electron captured. Although the neutrino is not detected, the value of its mass affects the shape of the de-excitation spectrum, reducing also the end-point of the spectrum by an amount equal to m_{ν_e} . The spectrum distortion is statistically significant only in a region close to the end-point, where the count rate is lowest and background can easily hinder the signal.

In terms of achievable statistical sensitivity, ^{163}Ho is one of the best candidate, given the combined effect of its low Q -value (2.833 keV) and the proximity of the highest energy peak to the end-point of the spectrum. ^{163}Ho also has a relatively short half life of $\tau_{1/2} \sim 4570$ years, which allows to embed a small number of nuclei in a small absorbing volume. Each single Holmes detector is composed of a ^{163}Ho ion-implanted gold absorber thermally coupled to a Transition Edge Sensor (TES). A TES is a sensitive thermometer, consisting of a superconductor Mo/Cu bi-layer film. This kind of detector works at very low temperatures (about 100 mK), so that an interaction in the absorber produces a detectable temperature rise proportional to the energy deposited.

The Holmes detectors not only need a fast recovery time, i.e. the time needed to cool down the thermometer to its base temperature, to reduce the amount of dead time but

also a quick time response to discriminate between two nearly coincident interactions. The latter is limited by the maximum sampling frequency set by the bandwidth of the acquisition system, which in turn is set by the number of detectors that need to be readout at the same time.

Given the target number of detectors and the single pixel activity, the detectors and the microwave multiplexing readout system will be pushed to their limits to meet the Holmes requirements.

During my PhD work I took care of various tasks, both hardware and software related. I tested the detector fabrication process and measured the resulting detector performances with the microwave multiplexing readout using external X-ray sources. I also studied the expected background due to cosmic rays and environmental radioactivity.

At the same time, I developed a modular and robust software for signal processing and data analysis, alongside new algorithms for the pile-up discrimination, the Holmes expected main source of background.

Chapter one briefly reviews the experimental efforts on the neutrino mass determination, with a spotlight on the state of the art experiments, while chapter two presents the Holmes experiment with its expected statistical sensitivity. Chapter 3 firstly introduces the physics behind the behavior of a Transition Edge Sensors, then focuses on the specific design and fabrication process of the Holmes detectors. Chapter 4 presents the analysis routines required to produce a clean calibrated spectrum from a raw dataset. Chapter 5 finally shows the measured detectors performances. The last part of the dissertation presents the expected background rate after the studies conducted with a dedicate measurements campaign.

Contents

Abstract	iii
1 Introduction	1
1.1 Neutrino masses and oscillations	1
1.2 Direct neutrino mass measurement via β^- decay	6
1.2.1 Spectrometric experiments	7
1.2.2 Calorimetric experiments	10
2 Holmes	13
2.1 ^{163}Ho for neutrino mass determination	13
2.2 EC decay of ^{163}Ho	14
2.3 Holmes and expected neutrino mass sensitivity	17
3 Transition Edge Sensors for Holmes	21
3.1 TES theory	21
3.1.1 Small signal approximation	22
3.1.2 Large signal and resistance models	27
3.2 Microwave Multiplexing readout	29
rf-SQUID and quarter wavelength resonator	30
μMUX multiplexing with flux ramp modulation	32
μMUX multiplexer chip for Holmes	34
3.3 Holmes detectors design	35
3.3.1 Modelling the thermal circuit	37
3.3.2 The heat capacity problem	37
3.4 Holmes array fabrication	38
3.4.1 Au deposition test	40
3.4.2 Si etching with KOH	42
3.4.3 ^{163}Ho production and embedding	43
4 Data reduction and signal processing	47
4.1 Data format with microwave multiplexing readout	47
4.1.1 Data type and dead time	47
4.1.2 Fast signals correction	49
4.2 First level data reduction	50
4.2.1 Evaluation of pulse information	50
4.2.2 Filters for event tagging	51
4.3 Energy estimation	53
4.3.1 Optimum filter	53
4.3.2 Arrival time correction	55
4.3.3 Gain drift correction	57
4.3.4 Energy calibration	59
4.4 Second level data reduction	61
4.4.1 Optimum Filter shape parameters	61

4.4.2	Wiener Filter and Pile-up discrimination	62
4.4.3	DSVP for discrimination of spurious events	65
5	Detectors performance	71
5.1	Experimental setup	71
5.1.1	Cryogenic setup	72
5.1.2	Warm Electronic setup	74
5.1.3	Holder setup	75
5.1.4	Calibration sources	77
5.2	TES time profile	78
5.3	Noise spectrum with a 32 channels array	82
5.4	Energy resolution	84
6	Background studies	87
6.1	Natural radioactivity and cosmic rays	88
6.1.1	Experimental setup	90
6.1.2	Detectors calibration	92
6.1.3	The coincidences problem	94
6.1.4	About the data analysis	95
6.1.5	Expected background rate	96
6.1.6	Muon induced background	99
6.1.7	^{40}K and neutrino mass sensitivity	100
6.1.8	Conclusion	102
6.2	Pile-up rejection	103
6.2.1	Simulations	104
6.2.2	DSVP and Holmes	106
6.2.3	DSVP time resolution with Wiener Filter	108
6.2.4	DSVP time resolution with an external calibration source	109
7	Conclusions	113

Chapter 1

Introduction

1.1 Neutrino masses and oscillations

Neutrinos are one of the most fascinating elementary particles. Each study conducted on them, from their discovery [1] to their emission due to the nuclear fusion nuclear in the stars [2] [3], has granted us a deeper understanding on the fundamental natural processes. The last two decades have seen a revolution in neutrino physics, and the demonstration of a non-vanishing neutrino mass from the observation of neutrino oscillation experiments is one of the major breakthrough.

This discovery boosted the interest on the topic, with the start of many ambitious experiments for different high precision measurements and the rate of published papers increased by almost an order of magnitude [4], but in spite of the enhanced experimental and theoretical efforts, there are still many unknowns about neutrinos and their properties. Among these, the value of their absolute masses, the neutrino mass ordering, the neutrino nature itself (Dirac or Majorana fermion), the magnitude of the CP violation phases and the possible existence of new neutrino species which do not participate in the standard weak interactions.

A complete review of these subjects is beyond the scope of this chapter. I will focus on the ones which are relevant for the topic of this thesis, i.e. the determination of the neutrino absolute masses.

When the flavor and mass eigenstates do not coincide, particles belonging to different families can interact with each other. In the Standard Model (SM), this phenomenon happens separately both in the quark and in the lepton sector, where the mixing probabilities are described by the elements of the CKM matrix V_{CKM} and the PMNS matrix U_{PMNS} respectively.

Unlike quarks, neutrinos do not have electric charge and their masses are extremely small compared to other particles; hence they are detected only as flavor states, allowing to observe the phenomenon of ‘neutrino oscillations’.

In the most general case, the so called neutrino flavor eigenstates are thus written as

$$\begin{pmatrix} \nu_e \\ \nu_\mu \\ \nu_\tau \\ \dots \end{pmatrix} = \begin{pmatrix} U_{e1} & U_{e2} & U_{e3} & \dots \\ U_{\mu1} & U_{\mu2} & U_{\mu3} & \dots \\ U_{\tau1} & U_{\tau2} & U_{\tau3} & \dots \\ \dots & \dots & \dots & \dots \end{pmatrix} \begin{pmatrix} \nu_1 \\ \nu_2 \\ \nu_3 \\ \dots \end{pmatrix} \quad (1.1)$$

where ν_i is a neutrino mass eigenstate with the physical mass m_i . with $i = 1, 2, \dots, 3 + n$. n was left different than zero because I wanted to stress out that even if the outcome from the study of the Z decay from the LEP collider clearly shows that there must be only three flavour species of neutrinos with masses below half of the Z mass weakly interacting with the bosons [5], recent experimental results and theoretical models implied the existence of

one or more neutrino species ν_4, ν_5, \dots , which mix with ν_1, ν_2, ν_3 to create sterile neutrinos in the flavour bases.

The expected mass scale of these new neutrinos varies a lot between these works. For example, LNSD [6], MiniBooNe [7] and reactor antineutrino anomalies [8] can be explained with one or two sterile neutrinos with masses $\mathcal{O}(1 \text{ eV})$, cosmological data from the CMB anisotropy and galaxy clustering indicates [9] one species of sterile neutrinos with masses below 1 eV while the type-I seesaw mechanism [10] introduce heavy sterile neutrinos to explain the small masses of the three ‘canonical’ ones. To further complicate this picture, many experimental results do not agree with each other and because the experimental setup varies a lot between these measurements, combining all the data is a daunting task and the results up to now have been inconclusive [11]. However, the number of dedicated experiments are growing, and the search for new neutrinos species is far from over.

If at least two neutrinos ν_i have non zero masses, then their superposition (the flavor eigenstate) have a non zero probability to change their flavor from α to β . The transition or ‘appearance’ probability, ignoring matter effects, can be written as

$$P(\nu_\alpha \rightarrow \nu_\beta) = \sum_i |U_{\alpha i}|^2 |U_{\beta i}|^2 + 2 \sum_{i < j} \left[\text{Re}(U_{\alpha i} U_{\beta j} U_{\alpha j}^* U_{\beta i}^*) \cos \Delta_{ij} - \text{Im}(U_{\alpha i} U_{\beta j} U_{\alpha j}^* U_{\beta i}^*) \sin \Delta_{ij} \right] \times \frac{1}{(UU^\dagger)_{\beta\beta} (UU^\dagger)_{\alpha\alpha}} \quad (1.2)$$

while the ‘disappearance’ probability is

$$P(\nu_\alpha \rightarrow \nu_\alpha) = 1 - \sum_{\alpha \neq \beta} P(\nu_\alpha \rightarrow \nu_\beta) \quad (1.3)$$

with $\Delta_{ij} \equiv \frac{\Delta m_{ij}^2 L}{(2E)}$, $\Delta m_{ij}^2 \equiv m_i^2 - m_j^2$ and L being the distance between the source and the detector and E the neutrino energy.

Eq (1.3) and (1.2) express indeed what the various oscillations experiments are measuring, with $\alpha, \beta = e, \mu, \tau$.

In general, due to the fact that for each experiment the neutrinos energy and L are fixed, only one mass scale is relevant each time, as shown in Table 1.1

Source	L[km]	E [GeV]	$\Delta m^2 [eV^2]$
atm ν ($\nu_e, \nu_\mu, \bar{\nu}_e, \bar{\nu}_\mu$)	10^4	1-10	$10^{-4} - 10^{-3}$
reactor ($\bar{\nu}_e$)	1	10^{-3}	10^{-3}
reactor ($\bar{\nu}_e$)	100	10^{-3}	10^{-5}
solar (ν_e)	10^8	$1 - 10^{-3}$	$10^{-11} - 10^{-10}$
accelerator ($\nu_\mu, \bar{\nu}_\mu$)	10^3	10	10^{-3}

TABLE 1.1: Δm^2 mass sensitivity, considering only vacuum oscillation.

In the standard three-flavor framework, the 3×3 PMNS matrix U is unitary and it can be parametrized in terms of three flavour mixing angles, $c_{ij} \equiv \cos(\theta_{ij})$ and $s_{ij} \equiv \sin(\theta_{ij})$ (for $ij = 12, 13, 23$) and three CP-violating phases δ, ρ and σ .

$$U_{PMNS} = \begin{pmatrix} 1 & 0 & 0 \\ 0 & c_{23} & s_{23} \\ 0 & -s_{23} & c_{22} \end{pmatrix} \begin{pmatrix} c_{13} & 0 & s_{13}e^{i\delta} \\ 0 & 1 & 0 \\ -s_{13}e^{-i\delta} & 0 & c_{13} \end{pmatrix} \begin{pmatrix} c_{12} & s_{12} & 0 \\ -s_{12} & c_{12} & 0 \\ 0 & 0 & 1 \end{pmatrix} \begin{pmatrix} e^{i\rho} & 0 & 0 \\ 0 & e^{i\sigma} & 0 \\ 0 & 0 & 1 \end{pmatrix} \quad (1.4)$$

The last two phases are called Majorana phases, they are related to the possible Majorana nature of the neutrino and can not be measured using eq (1.3) and (1.2). Currently, the three flavor states framework is able to describe the great majority of oscillation experiments data, Table 1.2 reports the global analysis on neutrino data [12].

parameter	best fit $\pm 1\sigma$
Δm_{21}^2 [10^{-5} eV ²]	$7.55^{+0.20}_{-0.16}$
Δm_{31}^2 [10^{-3} eV ²] (NO)	2.50 ± 0.03
Δm_{31}^2 [10^{-3} eV ²] (IO)	$2.42^{+0.03}_{-0.04}$
$\sin^2\theta_{12}/10^{-1}$	$3.20^{+0.20}_{-0.16}$
$\sin^2\theta_{23}/10^{-1}$ (NO)	$5.47^{+0.20}_{-0.30}$
$\sin^2\theta_{23}/10^{-1}$ (IO)	$5.51^{+0.18}_{-0.30}$
$\sin^2\theta_{13}/10^{-2}$ (NO)	$2.160^{+0.083}_{-0.069}$
$\sin^2\theta_{13}/10^{-2}$ (IO)	$2.220^{+0.074}_{-0.076}$
δ/π (NO)	$1.21^{+0.21}_{-0.15}$
δ/π (IO)	$1.56^{+0.13}_{-0.15}$

TABLE 1.2: Neutrino oscillation parameters summary determined from [12] in the three flavors scenario

The sign of Δm_{31}^2 remains unknown, and in the 3 flavors framework there are two possible scenarios: the so called normal order (NO) in which $m_1 < m_2 < m_3$ and inverted order (IO) $m_3 < m_1 < m_2$. As visible from Table 1.2, the mass ordering influences the fit results. It's worth pointing out that even if it's a challenging measurement, the sign of Δm_{31}^2 might be probed in the future by the most sensitive oscillation experiments.

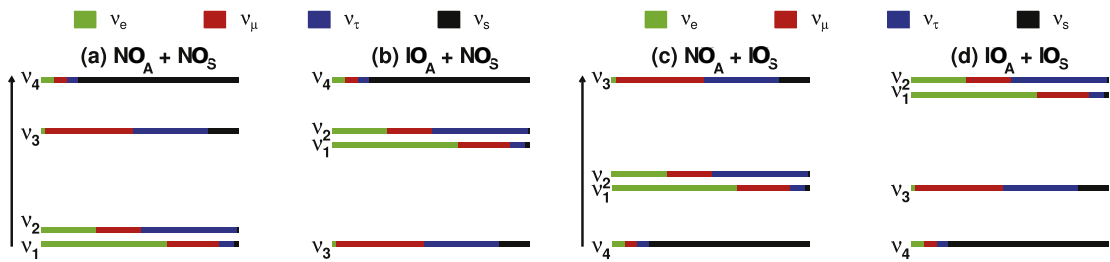


FIGURE 1.1: Four different scenarios of neutrino mass spectra in the three active (A) flavors plus one sterile (S) neutrino scheme. Picture taken from [13]

To summarize, neutrino oscillations unequivocally proves that at least two neutrinos have non-zero masses, raising the question on how to extend the standard model to include such a mass terms. The fact that neutrinos are the only leptons to have zero electric charges opens many possibilities, from extending the particle content of the standard model to right-handed neutrinos with a simple Yukawa mass term (Dirac neutrinos), to renouncing renormalizability with a Weingberg operator (Majorana neutrinos).

Yet, the neutrinos masses can not be derived from theory or neutrino oscillation experiments, and from their results it is only possible to evaluate an upper limit on their sums

$$\begin{aligned} \sum_i m_{\nu_i} &> 0.05 \text{ eV (NO)} \\ &> 0.1 \text{ eV (IO)} \end{aligned} \quad (1.5)$$

The neutrino absolute mass scale evaluation is one of the most compelling challenges in modern particle physics and astrophysics. It's value will help to discriminate between many of the theories which deal with the mass generation mechanisms. Its value is also of importance in many areas of Cosmology, from the evolution of the large scale structure (LSS) of the Universe [14] to cosmic rays with super- GZK energies (the Z-burst explanation) [15].

To assess the mass parameter we shall therefore rely on non-oscillation experiments. Some of them are strongly affected by uncertainties related to the theoretical model of the system they are investigating and are called model-dependent, while others assumes only energy and momentum conservation and are therefore called direct measurements. The former will be briefly summarized in the next sections.

Cosmological measurements

Due to their abundance as big-bang relics, neutrinos affect the large-scale structure and dynamics of the universe by means of their gravitational interactions, which hinder the structure clustering with an effect that is dependent on their mass. In the framework of Λ CDM cosmology, the scale dependence of clustering observed in the Universe can indeed be used to set an upper limit on the neutrino mass

$$M_\nu = \sum_i m_{\nu_i} \quad (1.6)$$

with m_{ν_i} the mass of the ν_i state.

Table 1.3 quote the data obtained by Planck [16], assuming three neutrino species with degenerate mass ordering ($m_i \sim m_j, \forall i, j$), a Fermi-Dirac distribution and zero chemical potential. The constraints are also reported for the combination of Planck data with different likelihood, priors and dataset in order to break the degeneracies of the many cosmological parameters

$M_\nu < 0.54 \text{ eV}$	(Planck TT + lowE)
$M_\nu < 0.26 \text{ eV}$	(Planck TT,TE,EE + lowE)
$M_\nu < 0.44 \text{ eV}$	(Planck TT + lowE+lensing)
$M_\nu < 0.24 \text{ eV}$	(Planck TT,TE,EE + lowE+lensing)
$M_\nu < 0.27 \text{ eV}$	(Planck TT,TE,EE+ lowE+lensing[Camspec])
$M_\nu < 0.60 \text{ eV}$	(Planck lensing + BAO + θ_{MC})
$M_\nu < 0.16 \text{ eV}$	(Planck TT+ lowE+BAO)
$M_\nu < 0.13 \text{ eV}$	(Planck TT,TE,EE+ lowE+BAO)
$M_\nu < 0.13 \text{ eV}$	(Planck TT+ lowE+lensing+ BAO)
$M_\nu < 0.12 \text{ eV}$	(Planck TT,TE,EE+ lowE+lensing + BAO)

TABLE 1.3: 95 % CL upper bound from the Planck collaboration

Considering the most stringent limit of $M_\nu < 0.12 \text{ eV}$ the inverted mass hierarchy, which requires $M_\nu > 0.1 \text{ eV}$, seems less plausible.

Neutrinoless double beta decay

The neutrinoless double beta decay ($0\nu\beta\beta$), if exists, is an extremely rare process. In such a process a virtual neutrino acts as a mediator between the vertices of two beta decays. Given the V-A nature of weak interactions, this process would require the coupling of a right-handed anti-neutrino in one vertex and of a left-handed neutrino in the other one, implying that neutrino is a Majorana particle. Thus the searches for $0\nu\beta\beta$ decay are searches for lepton-number violation whose observation would demonstrate beyond standard model physics.

The observables are the kinematic parameters of the two emitted electrons in the $0\nu\beta\beta$ and $2\nu\beta\beta$ decays. The latter is allowed by the SM and it represents the irreducible background for such measurements

$$\begin{aligned} (A, Z) &\rightarrow (A, Z + 2) + 2e + Q_{\beta\beta} \quad [0\nu\beta\beta] \\ (A, Z) &\rightarrow (A, Z + 2) + 2e + 2\nu_e + Q_{\beta\beta} \quad [2\nu\beta\beta] \end{aligned} \quad (1.7)$$

The $0\nu\beta\beta$ -decay signal is a monoenergetic peak at $Q_{\beta\beta}$ and the measured parameters is called the effective neutrino mass $\langle m_{\beta\beta} \rangle$

$$\langle m_{\beta\beta} \rangle = \left| \sum_i U_{ei}^2 m_i \right| \quad (1.8)$$

with U_{ei} the elements of the PMNS matrix 1.4.

Given the very small value of the neutrino mass, the phase space related to the process strongly suppress the probability of the decay, making it one of the most rare process that could occur in nature.

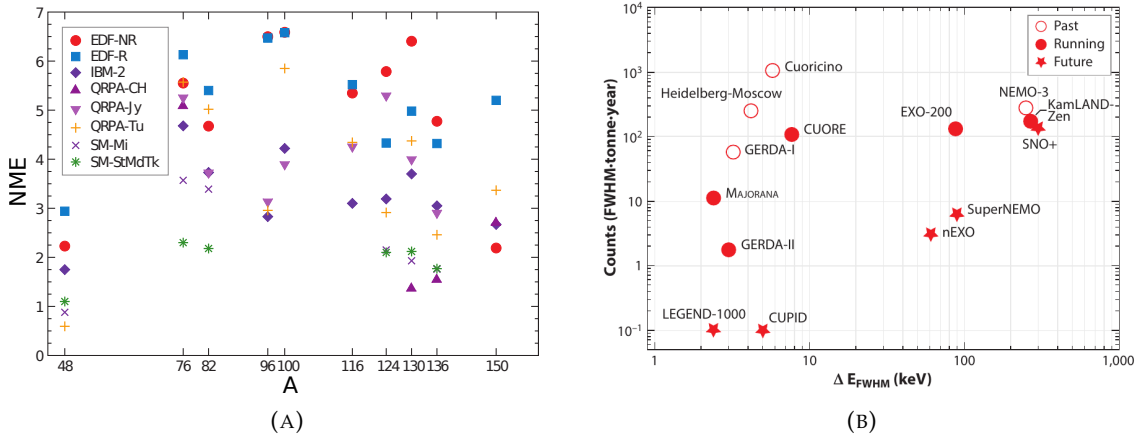


FIGURE 1.2: Pictures taken from [17]. (A) Status of the nuclear matrix element (NME) calculations for the various $0\nu\beta\beta$ isotopes and different approaches. (B) Background and energy resolution for the numerous experiments which are looking for the $0\nu\beta\beta$ decay.

Furthermore, the experimental difficulties are matched by the theoretical ones, among which the understanding the nuclear physics aspects of the decay. The latter is a hard nut to crack, mainly because it is a many-body problem with quarks inside a nuclear environment. Several approaches have been developed, and their results are summarized in Figure 1.2 (A) for the different isotopes used in $0\nu\beta\beta$ searches. The hope is that all the calculations will converge with future improvements.

Only few of the 35 isotopes capable of $2\nu\beta\beta$ are suitable candidate for Neutrinoless double beta decay searches. Many experiments are working to detect this rare decay using different isotopes and various measurement techniques to achieve an optimal energy resolution in combination with a low level of background. They measure the isotopes lifetime $T_{1/2}^{0\nu}$ which is proportional to $\langle m_{\beta\beta} \rangle$.

Table 1.4 shows their latest results

Isotope	$Q_{\beta\beta}$ [MeV]	$T_{1/2}^{0\nu}$ ($\times 10^{25}$ years)	$\langle m_{\beta\beta} \rangle$ [eV]	Experiment
^{48}Ca	4.263	$> 5.8 \times 10^{-3}$	$< 3.5 - 22$	ELEGANT-IV
^{76}Ge	2.039	> 8.0	$< 0.12 - 0.26$	GERDA
		> 1.9	$< 0.24 - 0.56$	Majorana Demonstrator
^{82}Se	2.998	$> 3.6 \times 10^{-2}$	$< 0.89 - 2.43$	NEMO-3
^{96}Zr	3.348	$> 9.2 \times 10^{-4}$	$< 7.2 - 19.5$	NEMO-3
^{100}Mo	3.035	$> 1.1 \times 10^{-1}$	$< 0.33 - 0.62$	NEMO-3
^{116}Cd	2.813	$> 2.2 \times 10^{-2}$	$< 1.0 - 1.7$	Aurora
^{128}Te		$> 1.1 \times 10^{-2}$	-	C.Arnaboldi et al.
^{130}Te	2.527	> 1.5	$< 0.11 - 0.52$	CUORE
^{136}Xe	2.459	> 10.7	$< 0.061 - 0.165$	KamLAND-Zen
		> 1.8	$< 0.15 - 0.40$	EXO-200
^{150}Nd	3.371	$> 2.0 \times 10^{-3}$	$< 1.6 - 5.3$	NEMO-3

TABLE 1.4: $\langle m_{\beta\beta} \rangle$ limits (90% CL) from [17]

1.2 Direct neutrino mass measurement via β^- decay

So far, the only model independent method of measuring the neutrino mass is based on the kinematic analysis [18] of the beta or the electron capture (EC) decay which, as already mentioned, only assumes momentum and energy conservation. In this section I will focus on the β^- -decay, because the EC, being the one studied by the Holmes experiment, will be treated in a separate chapter.

The decay mode for the β^- -decay is

$$\begin{aligned} (Z, A) &\rightarrow (Z + 1, A) + E^- + \bar{\nu}_e \\ n &\rightarrow p + e^- + \bar{\nu}_e \end{aligned} \quad (1.9)$$

where the latter equation is the basic underlying mechanism. It is a three body decay with the nucleus having a negligible recoil energy. Thus, the energy spectrum of the emitted electron (neutrino) is a continuous with the total energy released given by the Q value, i.e. the mass difference between the mother and daughter neutral atoms.

The transition rate to produce an electron is given by the Fermi Golden Rule

$$\frac{d^2N}{dt dE} = \frac{2\pi}{\hbar} |\langle f | H_{if} | i \rangle|^2 \rho(E) \quad (1.10)$$

where $|\langle f | H_{if} | i \rangle|$ is the transition matrix element, evaluated using the wavefunctions of the nucleons in the mother and daughter atoms and the wavefunctions of the electron-neutrino field, while $\rho(E)$ denotes phase space. The former is given by

$$|\langle f | H_{if} | i \rangle| = g^2 F(E, Z + 1) |\Phi_e(0)|^2 |\Phi_\nu(0)|^2 |M_{if}|^2 \quad (1.11)$$

with g an interaction coupling constant, $F(Z + 1, E)$ a correction function that takes into account the interaction between the emitted electron and the Coulomb field of the daughter nucleus, $\Phi_e(0)$ the wavefunction of the electron (neutrino) at $r = 0$ and M_{if} the nuclear matrix element, that is energy independent and has to be theoretically calculated.

As a consequence, the shape of the energy spectrum of the emitted electron in allowed transition is just given by the phase space

$$\frac{d^2N}{dt dE} = AF(E, Z + 1)pE(Q - E)\sqrt{(Q - E)^2 - m_{\bar{\nu}_e}^2}\theta(Q - E - m_{\bar{\nu}_e}) \quad (1.12)$$

neglecting nuclear recoil. A includes all the constant terms, θ is a heaviside function and $m_{\bar{\nu}_e}$ is the observable electron (anti) neutrino mass

$$m_{\bar{\nu}_e}^2 = m_{\nu_e}^2 = \sum_i |U_{ei}|^2 m_{\nu_i}^2 \quad (1.13)$$

As visible from (1.12), near the end-point, where the neutrino is non-relativistic, the shape of the spectrum changes with m_{ν_e} , allowing to measure the neutrino mass scale.

Eq (1.12) is complicated by the fact that the decaying atom or molecule might end up in a state of excitation energy E_j with probability P_j , resulting in a superposition of spectra with different end-point energies

$$\frac{d^2N}{dt dE} = AF(E, Z + 1)pE \sum_j (Q - E - E_j)\sqrt{(Q - E - E_j)^2 - m_{\bar{\nu}_e}^2}\theta(Q - E - E_j - m_{\bar{\nu}_e}) \quad (1.14)$$

From all β^- -decay nuclei, tritium is the most favored one, with the Q value of 18592.01(7) eV [19] and with the relatively simpler atomic structure, allowing to evaluate the nuclear matrix elements and the various excitation probability P_j .

I want to emphasize that even if direct measurements are theory-unrelated techniques to measuring the neutrino mass, many ‘practical’ effects could introduce potential bias in the results. For this reason, direct neutrino mass measurements call for a continuous crosscheck from different independent experiments to confirm both positive and negative findings.

The main results of the experiments that used the β^- -decay to assess the neutrino mass scale, can be divided into two categories: spectrometric experiments, where the radioactive source is placed outside the detectors, and calorimetric experiments, where the nuclei are embedded inside the detectors.

1.2.1 Spectrometric experiments

Spectrometers are the most sensitive technology in direct neutrino mass measurement to date, using tritium ^3H (indicated also as T) as β^- -decay nuclei. Their main advantages are the extremely high energy resolution (< 3 eV at 18 keV for the KATRIN spectrometer) combined with the ability to select only the electrons with energy close to the end-point, allowing to collect a high number of events while keeping the fraction of pile-up events negligible.

On the other hand, this kind of approach has fundamental intrinsic limits, mainly due to the fact that the emitting source is external to the detector, such as the effects of energy loss, source charging, backscattering from the substrate (if the source is deposited on a thin substrate layer) and the energy dependence of detection efficiency.

In addition, in MAC-E-Filters spectrometers, ^3H is not used in atomic form, but rather in its molecular form H_2 . A detailed treatment of the final state is necessary, and the molecular binding energies have to be considered alongside the the small nuclear recoil.

Two experiments used this technique: Mainz and Troisk. Their main difference was the source type: a monolayer of frozen T_2 for Mainz and a windowless gaseous tritium source for Troisk. After a few years of data taking, in the early 2000s they achieve an upper limit of $m_{\bar{\nu}_e} < 2.3 \text{ eV}$ [20] and $m_{\bar{\nu}_e} < 2.05 \text{ eV}$ [21] respectively, both at 95 % CL.

KATRIN

The Karlsruhe Tritium Neutrino (KATRIN)[22] is the ultimate spectrometer experiment that started its first science run in spring 2019. It aims to reach the unprecedented sensitivity on $m_{\bar{\nu}_e}$ of 0.2 eV, probing the quasi-degenerate range¹ of neutrino masses.

As its predecessors Mainz and Troisk, it uses the MAC-E-filters technique, in combination with a windowless gaseous molecular tritium source. All of its components, showed in Figure 1.3, has been build to reach the best achievable precision with this technique.

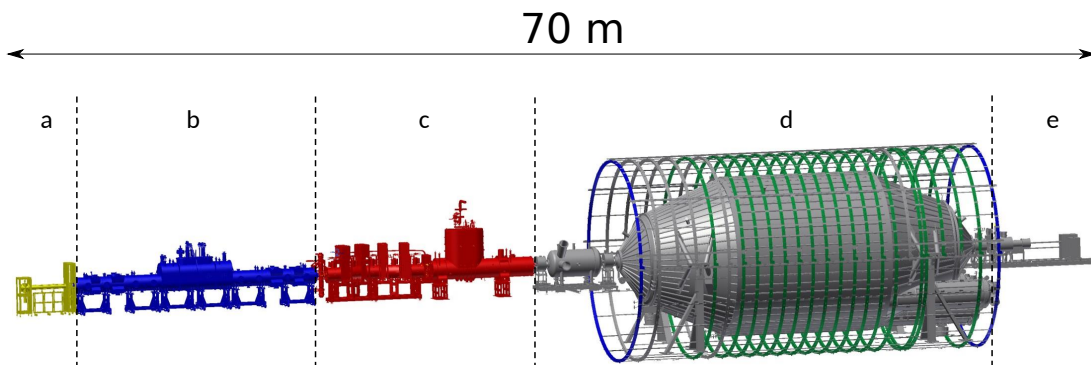


FIGURE 1.3: Scheme of the KATRIN beamline: a) rear section, b) windowless gaseous tritium source, c) transport section, d) spectrometer section e) detector section.

The magnetic field in the source adiabatically guides the electrons from the tritium source into the main spectrometer, with different electrodes to prevent other charged spurious elements to enter the vessel and a series of turbomolecular pumps alongside a cryo-pumping system to greatly reduce the amount of gas molecules that enters the spectrometer. The column density of the gas is continuously checked and it is taken into account in the final energy spectrum.

After that, a pre-spectrometer roughly select only the electrons in the energy interval few hundred electronvolt below the end-point. Then, the electron travel though an ultra-high vacuum (10^{-11} mbar) guided by a magnetic filed, collimated by its gradient and filtered by an tunable electrostatic barrier.

The surviving electrons are accelerated again and finally counted in a radially segmented silicon detector array with 148 pixels for background discrimination and event corrections. The tritium beta decaying spectrum is therefore measured in an integral mode and the differential spectrum must be reconstructed by scanning the potential.

Due to the fact that the electrostatic potential is known with a great level of precision, the energy resolution is given by the ratio of the magnetic field between its minimum and its maximum value, which in turn is related to the geometry of the spectrometer.

¹'Large' neutrino masses compared to their mass differences.

A dedicate measurement campaign proved that all the specifications have been met, but the background level was higher than anticipated. The main cause seems to be related to Rydberg atoms sputtered off the inner spectrometer surfaces by ^{206}Pb recoil following a α -decays of ^{210}Po . These ions are then excited by the black body radiation of the vessel, creating electrons that are indistinguishable from the ones emitted by the tritium source. This hypothesis was investigated [23] and seems plausible.

The first high-purity tritium campaign [24] started in 2019 and lasted for about a month (tritium throughput 4.9 g/day). Nevertheless, they achieved a new limit on the neutrino mass, with a best fit value of $m_{\bar{\nu}_e}^2 = (-1.0^{+0.9}_{-1.1}) \text{ eV}^2$, resulting in an upper value of $m_{\bar{\nu}_e} < 1.1 \text{ eV}$ (90% CL with Likhov and Tkachov method) or $m_{\bar{\nu}_e} < 0.8 \text{ eV}$ (90% CL with Feldman and Cousins method).

Project 8

Project 8 [25] is an ambitious experiment aimed to overcome the limitation imposed by the MAC-E-filters technique, achieving a statistical sensitivity the neutrino mass $m_{\bar{\nu}_e}$ of 40 meV (90% CL).

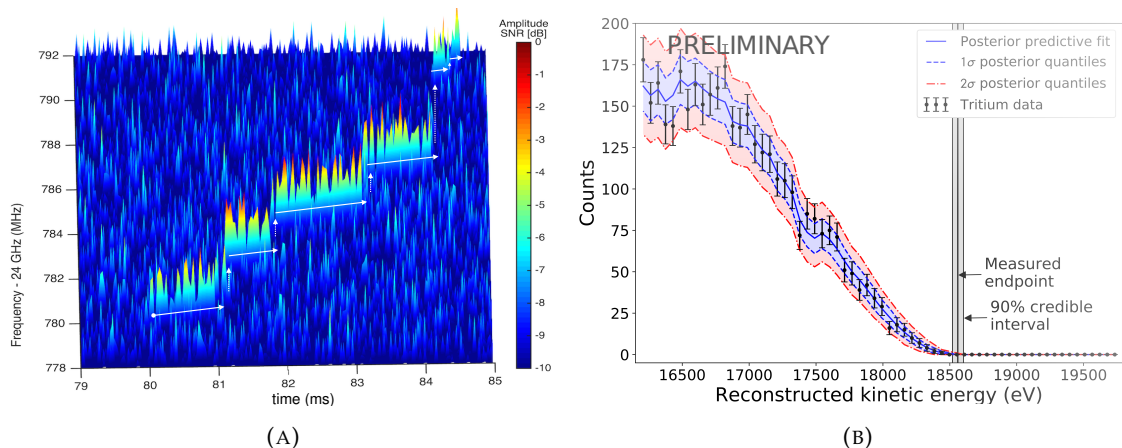


FIGURE 1.4: Images taken from [26] (A) An individual ^{83m}Kr conversion electron. The jumps are the electron that scatters of gas molecule, losing energy and changing pitch angle. The frequency of the first track gives the initial electron kinetic energy. (B) The preliminar energy spectrum measured during Phase II.

To do so, they developed a new technique called Cyclotron Radiation Emission Spectroscopy (CRES) [27] to measure the energy of the electron emitted by the tritium. If the Tritium source decays in a uniform magnetic field B , the electron emits cyclotron radiation, which depends on the kinetic energy E_k of the electron. Therefore an accurate measurements of the frequency f corresponds to a measurements of the electron energy

$$f = \frac{eB}{2\pi(m_e + E_k/c^2)} \quad (1.15)$$

The advantages of this technique are the event-by-event energy reconstruction and the fact that the tritium gas is transparent to cyclotron radiation (an electron with an energy of 18.6 keV in a $\sim 1\text{T}$ magnetic field radiates at approximately 26 GHz.), removing the need to extract the electron from the source. There are also many challenges, from the low readout noise required to measure a power of the order of few fW to the gas pressure of the source, that has to be optimized to allow the electron to travel several microseconds in

order to precisely measure its emitted radiation. Figure 1.4 shows the typical signal of a CRES event.

Project 8 will go through four different phases [28], each with a distinct and increasingly challenging scientific goal. Phase I was concluded in spring 2016 and demonstrated the CRES technique with a prototype setup. They measured the electrons emitted by a low pressure ^{83m}Kr in a small experimental volume. They achieved a remarkable energy resolution of 16 eV FWHM at 30.4 keV and 3.3 eV at the same energy changing the magnetic field configuration, limiting also the rate of observable events. They also preliminary estimate the background events rate with this technique, which is expected to be smaller than 10^{-7} events $\text{eV}^{-1} \text{s}^{-1}$ for an effective volume of 1000 m^3 .

Phase II performed the first CRES measurement of tritium decay using the same setup of phase I with a T_2 gas source (gas volume $\sim 10 \text{ cm}^3$). The measurement campaign started in September 2019 and was completed in 2020, with the full analysis of the data still underway.

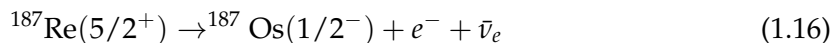
Phase III will change the readout setup, using a molecular tritium source in free space with phased array of antennas. The expected limit on neutrino mass in this phase is 2 eV. Phase IV will finally reach the target sensitivity of 40 mV. To do so, they planned to change the tritium source, from molecular to atomic tritium, enlarging also the experimental volume to 200 m^3 (10 m^3 of effective volume). One of the challenge is to avoid the recombination of atomic tritium into T_2 , with the target purity of the source gas T_2/T of $\sim 10^{-6}$. The complete design for the last phase is still to be defined.

1.2.2 Calorimetric experiments

In an ideal calorimetric experiment, the radioactive source is embedded in the detector and, if the excitation of atomic or molecular levels is negligible compared with the detector time response, only the neutrino energy escapes the detection, avoiding most of source-related effects that characterize the spectrometric experiments.

On the other hand the whole spectrum is acquired, posing important limits on the source intensity and therefore on the statistics that can be accumulated. The activity of the source is also limited by the relation between the detector size and its energy resolution.

After the pioneering experiment of Simpson with tritium [29], ^{187}Re was indicated [30] as a feasible alternative to tritium because its transition energy $Q = 2470.9(13) \text{ eV}$ [31] is one of the lowest known, increasing the fraction of useful events in the region close to the end point. ^{187}Re decays through β^- emission



with a unique first forbidden transition. Its nuclear matrix elements is computable, even if not straightforward as the one of tritium. The other characteristic that made this isotope appealing was its large isotopic abundance (62.8 %).

Two experiments² followed this approach, MANU and MIBETA. MANU started in 1985 using low temperature microcalorimeters with metallic rhenium absorbers. The thermometer was a NTD germanium. In 2001, as a result of a high statistics measurement they achieved an upper limit on the neutrino mass of $m_{\bar{\nu}_e} < 19 \text{ eV}$ (90% CL) [32]. MIBETA used instead AgReO_4 as absorber, a dielectric rhenium compound, achieving a better energy resolution and detector response compared to MANU (28.5 eV FWHM at ^{187}Re end-point, compared to the 96 eV of MANU at 5.9 keV). The fit of the acquired 7 months spectrum gave an upper limit on neutrino mass of $m_{\bar{\nu}_e} < 15 \text{ eV}$ (90% CL) [33].

²For an extensive review on this topic, see [4]

However, after those experiences it became clear that metallic rhenium absorbers do not behave as expected, presenting also many unwanted effects, such as the Beta Environmental Fine Structure (BEFS) [34], which spoil the neutrino mass sensitivity. As a result, a large scale neutrino mass experiment based on ^{187}Re beta decay is not foreseeable in the near future and the ^{163}Ho seems to be the best candidate for a sensitive calorimetric neutrino mass experiment.

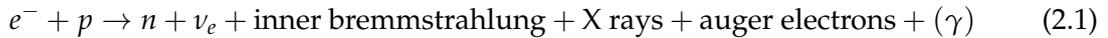
Chapter 2

Holmes

2.1 ^{163}Ho for neutrino mass determination

During the last decades, there has been an increasing interest on ^{163}Ho as a powerful means for neutrino mass estimation. It has a lower Q value ($Q = 2833 \pm 30(\text{stat}) \pm 15(\text{syst})$ eV [35]) than ^3H and lower half life ($T_{1/2} \sim 4570$ years) than ^{197}Re , and decays via Electron Capture (EC) on an atomic excited state of ^{163}Dy .

In an electron capture decay, an unstable nucleus capture an atomic electron with a non vanishing wave function at the origins which interacts with a proton to produce a neutron and emitting a neutrino accompanied by the emission of internal bremsstrahlung. The daughter atom is in an excited state, and the vacancy left in the electron shell by the capture electron is filled by subsequent emission of X-rays and auger electrons. If the nuclide is also left in an excited energy state, gamma radiation can be emitted. Overall, the whole process can be seen as:



Unlike the beta decay, the resulting neutrino energy spectrum is the same as a two body decay with the neutrino having energy equal to $E_\nu \simeq Q - E_b$, with E_b the electron binding energy. Better said, in each EC decay the emitted neutrino is recoiling against a series of states with a non-zero widths.

In particular, for the EC decay of the ^{163}Ho there is no gamma emission and the Dy atoms decays predominantly by Coster-Kroning and Auger transition rather than X-rays (the fluorescence yields are $\leq 1 \times 10^{-3}$ [36]).

Over the years four independent methods were proposed to estimate the neutrino mass from the ^{163}Ho EC: M/N capture rates [37], Inner Breemstrahlung end-point (IBEC) [30], the end-poin Single Electron Ejection (SEEEC) [38] and the calorimetric de-excitation spectrum end-point measurement [36].

The latter aroused interest, because in a calorimetric measurement all the energy of the decay E_c is measured but that of the neutrino

$$E_c = \text{nuclear recoil} + \text{inner bremsstrahlung} + \text{X rays} + \text{auger electrons} \quad (2.2)$$

obviate the complication induced by “atomic and molecular problems” related to current state of the art experiment in the direct neutrino mass determination.

As we will shortly see, the calorimetric spectrum is composed of several lorentzian-shaped peaks with energy equal to the binding energy E_b^H of the electron captured from the H -shell. The neutrino mass affects the shape of the de-excitation spectrum, reducing also the end-point of the spectrum by a quantity proportional to m_{ν_e} . The complexity lies in the fact that this spectrum distortion is statistically significant only in a region close to the end-point, where the count rate is lowest and background can easily hinder the signal.

Thanks to the remarkable progress made by the detector technologies, the calorimetric measurement is now the most promising approach and two collaborations are currently developing large arrays experiments to prove the feasibility of this technique: ECHo [39], using Magnetic Metallic Calorimeters (MMCs) and HOLMES [40], which instead is using Transition Edge Sensors (TESs). Both are very sensitive cryogenic thermometers that measure, with different techniques, the increase in temperature due to the energy released in the decay $\Delta T = E_c/C$, with C the heat capacity of the detectors.

The feasibility of this technique is also due to features of the chosen isotope. In fact, the relative short half-life of ^{163}Ho combined with the low Q value allow to embed the required amount of isotope in a small absorbing volume, leaving the heat capacity of the thermometers low and thus allowing to achieve an outstanding level of energy resolution compared to other detectors at this energy scale.

Every now and then other isotopes have been proposed as an alternative to the ^{163}Ho for their lower Q value (for instance [41]). However, this feature is always counter-balanced by others such as their extremely long half-life, making a future calorimetric experiment extremely challenging in practice, if not unfeasible at all.

2.2 EC decay of ^{163}Ho

The complex structure of the ^{163}Ho isotope, with its 67 protons, 96 neutrons and 67 electrons makes the prediction of the shape of the calorimetric EC spectrum extremely challenging. In this section, I will outline the main results of the different theoretical works ([42], [43], [44] to name a few) that have been made to tackle this issue, from the simplest, but still very useful, model to the most complete one, based on *ab initio* calculations [45] [46].

At first order, the EC ^{163}Ho decay can be seen as



H labels the H -shell from which the electron has been captured. The calorimetric spectrum results in a weighted sum of Breit-Wigner (BW) peaks, at $E_c = E_H$ and with natural widths Γ_H , as explained in eq (2.4)

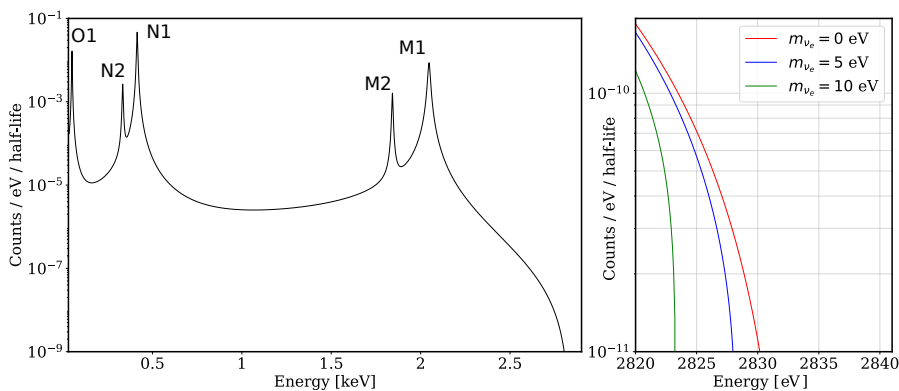


FIGURE 2.1: ^{163}Ho EC calorimetric spectrum per atom per half life, using eq (2.4) and peaks parameters from Table 2.1. O2 and P1 peaks have a negligible influence on the neutrino mass, and they are not depicted in this picture. On the right the effect of different values of m_ν on the shape of the spectrum at the end-point is shown.

$$\frac{d\lambda_{EC}}{dE_c} = \frac{G_F^2 \cos^2 \theta_C |\mathcal{M}|^2}{4\pi^2} (Q - E_c) \times \left[(Q - E_c)^2 - m_\nu^2 \right]^{1/2} \times \sum_H \phi_H^2(0) n_H B_H \frac{\Gamma_H/2\pi}{(E_c - E_H)^2 + \Gamma_H^2/4} \quad (2.4)$$

with $|\mathcal{M}|^2$ the nuclear matrix element, $\phi_H^2(0)$ the values of the squared wave functions at the origin of the electrons to be captured, $B_H - 1$ an $\sim 10\%$ correction for atomic exchange and overlap and n_H the electron occupancy in the H shell.

The tails of the Breit-Wigner peaks extend to the limit imposed by the Q value and, as in beta decay, near the end-point the spectrum becomes simply proportional to the phase space $(Q - E_c) \times \sqrt{(Q - E_c)^2 - m_\nu^2}$.

Actually, the true energy spectrum should be the coherent sum of three spectrum with different end-points

$$\frac{d\lambda_{EC}}{E_c} \propto \sum_j |U_{ej}|^2 (Q - E_c) \sqrt{(Q - E_c)^2 - m_j^2} \quad (2.5)$$

where m_j is the mass of the j -th neutrino while U_{ej} are the entries of the PMNS matrix. However, if the energy resolution ΔE is greater than the magnitude of the neutrino masses, eq (2.5) becomes eq (2.4). To prove it, we will evaluate the difference between the probabilities of finding an event close to the end-point, where the difference is maximal, of eq (2.5) and eq (2.4), and calculate the value of m_ν that makes this difference negligible. Calling m_L the mass of the lightest neutrino, the probability to find an event near the end-point for eq (2.5), P_{mj} , is given by

$$\begin{aligned} P_{mj} &\propto \int_{Q-m_L-\Delta E}^{Q-m_L} \sum_j |U_{ej}|^2 (Q - E) \sqrt{(Q - E_c)^2 - m_j^2} dE \\ &= \sum_j |U_{ej}|^2 \times \left[-1/3(Q^2 - 2QE_c - m_j^2 + E_c^2)^{3/2} \right]_{Q-m_L-\Delta E}^{Q-m_L} \\ &\simeq \sum_j |U_{ej}|^2 \times 1/3 \left[(m_L + \Delta E)^2 - m_j^2 \right]^{3/2} \end{aligned} \quad (2.6)$$

and the same goes for the probability of (2.4), $P_{m_\nu} = 1/3 \left[(m_L + \Delta E)^2 - m_\nu^2 \right]^{3/2}$. Now, if we impose that the difference between these two probability should be approximately zero and expand these equations around $m_j^2/\Delta E^2$ and $m_\nu^2/\Delta E^2$ respectively, we find the relation between the value that we measure, m_ν , and the true neutrino masses.

$$P_{mj} - P_{m_\nu} = 0 \rightarrow m_\nu^2 = \sum_j |U_{ej}|^2 m_j^2 \quad (2.7)$$

Eq (2.4) stresses out another advantage of the EC calorimetric measurement compared to the beta decay, that is the enhancement of the count rate near the end point by the proximity of the last atomic resonance. For the ^{163}Ho there are seven BW peaks, labeled in decreasing order of energy, M1, M2, N1, N2, O1, O2 and P1, with Table 2.1 showing the predicted value for the peaks parameters.

However, it has been pointed out [43] that other contributions can be not neglected to

Name	E_H [eV]	Γ [eV]	I_H	ref
M_1	2047	13.2	1	[47]
M_2	1842	6.0	0.0526	↑
N_1	414.2	5.4	0.2329	↑
N_2	333.5	5.3	0.0119	↑
O_1	49.9	3.0	0.0345	[48]
O_2	26.3	3.0	0.0015	-
P_1			0.0021	-

TABLE 2.1: Parameters used to plot the spectrum in Figure 2.1. I_H is given by $\phi_H^2(0)B_H$, and represent the relative peak intensity.

correctly describe the whole spectral shape: the so called- shake-up and shake-off. During the EC process, the wave function of the non captured electrons in the original and in the daughter atom are not identical and the mismatch between them can lead to the instantaneous creation of secondary holes H'



An electron expelled from the H' orbital could be ‘shaken up’ to an unoccupied atomic level or ‘shaken off’ into the continuum. The shake up signature is a peak at $E(H, H') \sim E(H) + E(H')$ while the shake off is a broad continuum. As we will see, while the shake-up can lead to complicated spectral features, the shake-off in principle could enhance the count rate in the endpoint region by a significant amount.

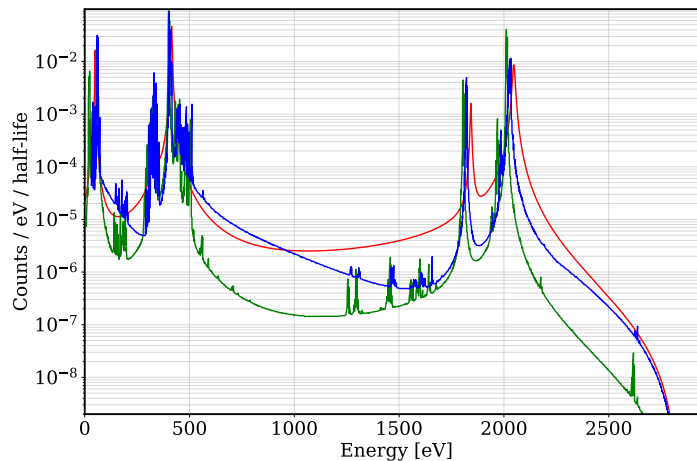


FIGURE 2.2: Comparison between the different differential calorimetric spectrum. In red the one from figure 2.1, in blue and green the ones evaluated with *ab initio* calculations with and without shake-off, respectively. The latter assume a constant lorentzian line width of 1eV.

This is indeed what is also underlined by *ab initio* calculation, which used both methods developed in quantum chemistry to calculate the many-body ground state and Green’s function methods to describe the electron capture process, resulting in a EC spectrum restricted to bound states calculated from first principles.

This calculation predict several additional features in addition to the 7 peaks, among these the asymmetric broadening of the resonances peaks with larger tails on the high energy side due to the shake-off and a shift of the energy of the resonances of few tens of eV (e.g. M1 resonance passes to 2028 eV).

In [46] the spectrum in blue was also compared to the one measured by the ECHO collaboration in [49], showing a good agreement between the theory and the measured data for the given experimental resolution. This is indeed a promising result.

2.3 Holmes and expected neutrino mass sensitivity

Frequentist Monte Carlo simulations have been performed [50] in order to address the statistical sensitivity of such a calorimetric experiment. They consists in the simulation of the spectra that would be measured by a large number of experiments carried out in a given configuration, taking into account both the natural background and the pile-up spectrum.

The latter is the expected energy distribution of multiple decays which occur within a time interval shorter than the time resolution of the detector and are recorded as a single decay with the energy given by their sum. As a good approximation, it is given by the convolution of the single spectrum with itself, multiplied by the fraction of unresolved pile-up events f_{pp} given approximately by $f_{pp} \sim \tau_R A_{EC}$, with τ_R the time resolution and A_{EC} the single detector activity.

The theoretical spectrum is given by

$$S(E_c) = \left[N_{ev} \left(N_{EC}(E_c, m_\nu) + f_{pp} (N_{EC}(E_c, 0) * (N_{EC}(E_c, 0))) + B(E_c) \right) \right] * R_{\Delta E}(E_c) \quad (2.9)$$

with $N_{EC}(E_c, m_\nu)$ given by eq (2.4) with parameters from Table 2.1. $B(E)$ the background spectrum, taken as a constant $B(E) = bT$, with b the average bkg count rate for single detector and $T = N_{det} \times t_M$ is the experimental exposure given the number of detectors N_{det} . N_{ev} is the total number of events, given by $N_{ev} = N_{det} A_{EC} t_M$ while $R_{\Delta E}(E_c)$ is the gaussian response function of the detector with a given energy resolution ΔE (FWHM).

I want to point out that now that a more accurate description of the ^{163}Ho EC spectrum is available, the simulation will be redone, however, due to the fact that the end-point region between the simpler and the *ab initio* spectra are very similar, a significant change in the results is not expected.

The set of fake-experimental spectra was obtained by fluctuating the spectrum (2.9) according to Poisson statistics. Each spectrum is then fitted using also eq (2.9) and leaving $m_\nu^2, Q, N_{ev}, f_{pp}$ and b as free parameters.

The 90 % CL m_ν statistical sensitivity $\Sigma_{90}(m_\nu)$, is given by the resulting distribution of m_ν , following a procedure explained in [51].

To assess the various dependencies of the neutrino mass sensitivity, the initial parameters were changed within a reasonable range of values. The simulations confirmed (Figure 2.3) that to reach the crucial sub-eV sensitivity on the neutrino mass a large number of events is required

$$\Sigma_{90}(m_\nu) \propto N_e v^{-1/4} \quad (2.10)$$

Once N_{ev} is fixed, the dependence on the pile-up fraction and on the energy resolution is shown in Figure 2.4. The plot suggests that the impact of the energy resolution is smaller than that of pile-up. In addition, in presence of a high level of pile-up the experiment is less sensitive to the energy resolution. Thus, for a fixed measuring time and a fixed

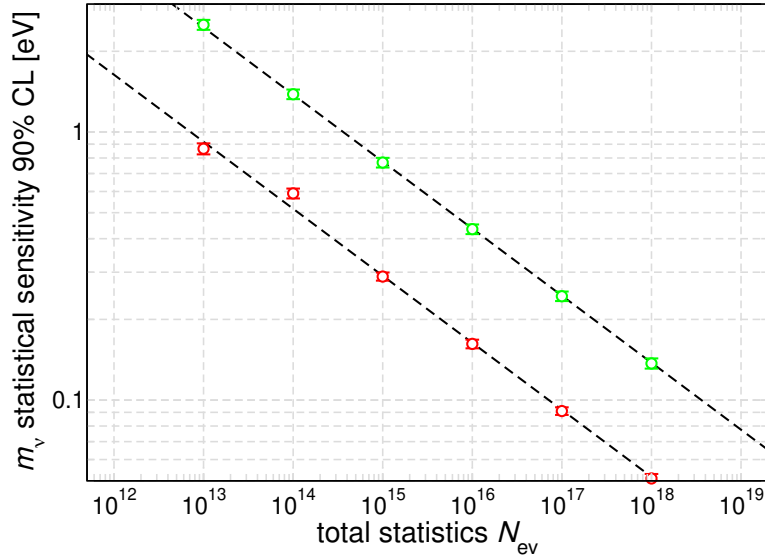


FIGURE 2.3: *Left* Monte Carlo estimated statistical sensitivity for $\Delta E = 1$ eV, $\tau_R = 1\mu s$, and for both $f_{pp} = 10^{-3}$ and 10^{-6} (from top to bottom). The dashed lines are the extrapolated curves using a $N_{ev}^{-1/4}$ scaling law.

number of detectors, it always pays out to increase the single detector activity as high as technically possible, even at the expense of an increasing pile-up level.

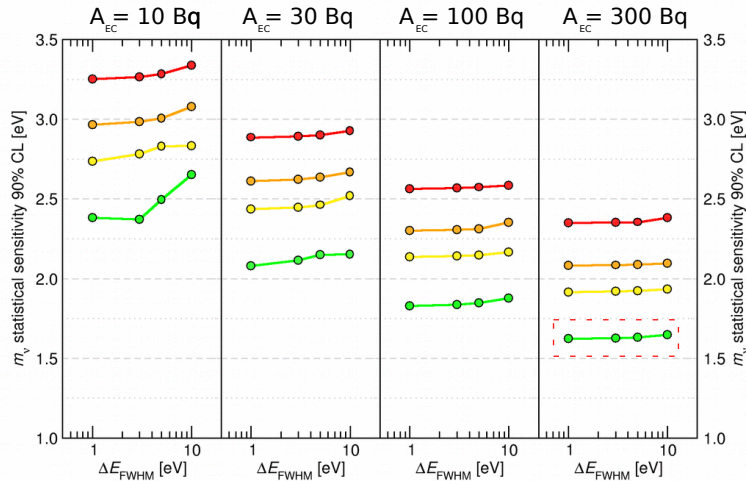


FIGURE 2.4: The results obtained from the simulations on the neutrino mass sensitivity by varying the single pixel activity A_{EC} , the τ_R and the ΔE of the detectors while keeping the N_{det} and t_m fixed, about 3000 detector \times year. With the various color are indicated the values for the τ_R parameter: red = 10 μs , orange = 5 μs , yellow = 3 μs and green = 1 μs .

These ideas were the starting point of the Holmes experiment. The ERC project Holmes began in 2014, and it is now being set up in the cryogenic laboratory of the University of Milano Bicocca.

It will perform a direct measurement of the neutrino mass with a sensitivity of the order of 1 eV. Most important, it will prove the feasibility of this technique to a next generation

experiment that might go beyond the current spectrometers sensitivity.

To reach the goal sensitivity, Holmes will use 1000 low temperature microcalorimeters, each implanted with an activity (A_{EC}) of 300 Hz, that will record about 10^{13} events in three years.

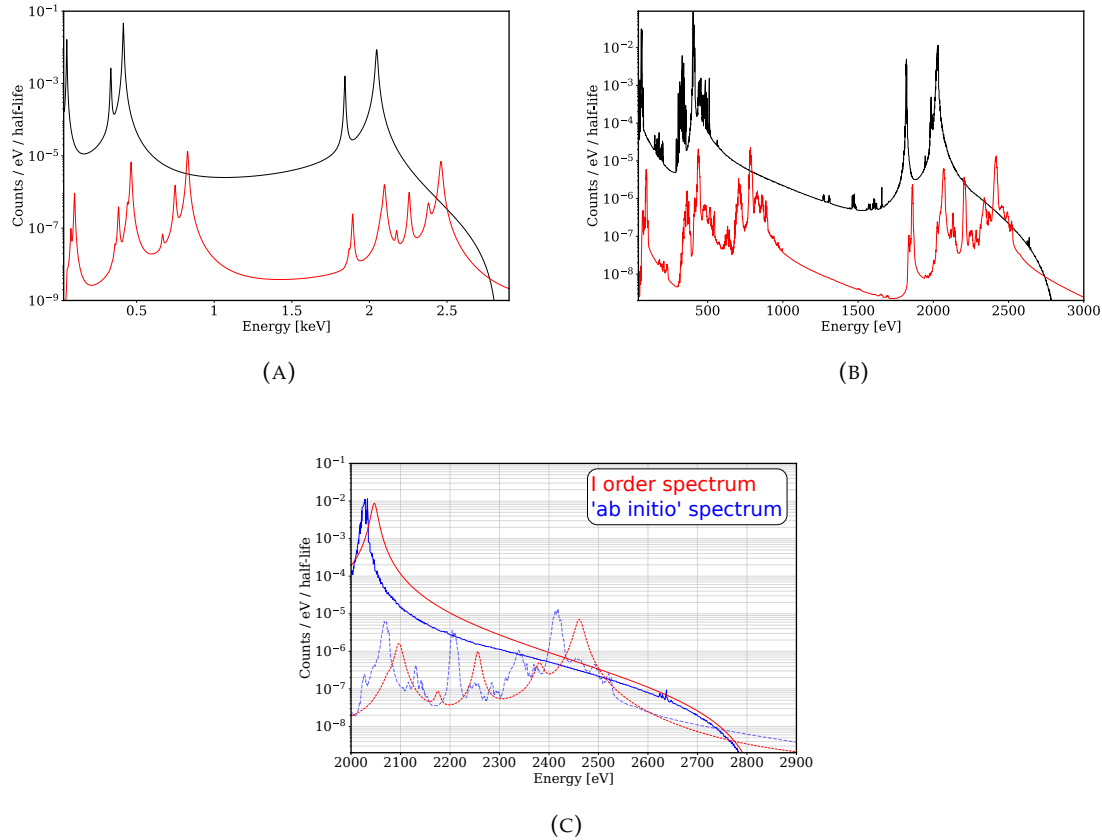


FIGURE 2.5: (A) and (B): single (black) and pile-up (red) spectra for the first order spectrum (eq (2.1)) and full theoretical spectrum respectively. The pile-up was normalized by considering a pile-up fraction $f_{pp} = 10^{-3}$, which correspond to a time resolution of $3 \mu\text{s}$. (C) Comparison between the two spectra above the M1 peak, using the above parameter. The dotted lines are the corresponding pile-up.

Figure 2.4 shows the expected sensitivity as a function of the detector energy resolution and the pile-up fraction for a given target activity. We can see that for the various activity there is a strong dependency of $\Sigma_{90}(m_\nu)$ on the detector time resolution, therefore developing strong pile-up reduction techniques alongside high performing detectors, both in terms of energy resolution and time response, is mandatory for the success of the Holmes experiment.

From a theoretical point of view, many different things could spoil the neutrino mass sensitivity of a calorimetric experiment such as Holmes.

As we saw in section 2.2, the EC spectrum of ^{163}Ho is rich in interesting structures, some of which may still be undiscovered. It's worth stressing out that the *ab initio* calculations have come a long way in evaluating most of them, at least the most relevant one.

Regardless of these features, near the end point region no resonance or shake off peak is present, and the spectrum shows the signature dependence of the decay rate on a root

term proportional to the neutrino mass

$$\left. \frac{d\lambda_{EC}}{dE_c} \right|_{E_c \sim (Q - m_\nu)} \propto K(E) \times (Q - E_c) \times \left[(Q - E_c)^2 - m_\nu^2 \right]^{1/2} \quad (2.11)$$

If the energy region in which the neutrino mass estimation is performed (ROI) is chosen to be sufficiently small, $K(E)$ can be approximated with a polynomial of order 1 (2) and the same goes for the pile-up spectrum and natural background. The fit parameters will pass from 5, $Q, m_\nu, f_{pp}, bkg, N_{ev}$, to 6 (8) with the task of constraining them consequently becoming more challenging, but yet not unfeasible. As a result, the unknown features of the EC spectrum, if present at all, should not impair the neutrino mass determination.

Unpredicted background peaks in the region of interest can worsen the neutrino mass sensitivity. As it will be explained in section 6.1.7, the only peaks that can reasonably be present are the one from the EC decay of ^{40}K but, in order to produce a statistically significant alteration in the neutrino mass estimation the contamination of potassium should be unreasonably high, therefore we do not expect such problem.

Pile-up peaks in the ROI also represent a threat because their shape cannot be precisely predicted. However, as shown in Figure 2.5, even with the shake-up no such peaks are predicted in the region between 2650 and 2900 eV.

The Holmes collaboration is now almost ready to perform the first low dose implantation on a 2×32 array. The main goal of this phase will be to access the variation in the detectors performance due to amount of Ho nuclei inside their absorbers. As a result, the maximum activity per detector will be defined and the deployment of the 1000 detector will start.

Chapter 3

Transition Edge Sensors for Holmes

3.1 TES theory

A microcalorimeter is a thermal detector that can be operated at cryogenic temperatures and measures the energy deposition via conversion to heat.

When an energy deposition E occurs inside the detector, there will be an increase in temperature proportional to the energy released $\Delta T = E/C$ where C is the heat capacity of the detector. It can be shown that the RMS energy fluctuations in a thermally isolated heat capacity C at temperature T due to the exchange of energy with a thermal bath also at T are given by

$$\Delta E \propto \sqrt{k_b T^2 C} \quad (3.1)$$

This quantity, sometimes referred as the thermodynamic limit, suggests the motivation for the use of Low Temperature Detectors (LTD): the suppression of thermal noise. The precision of the measurement improves when C and T are kept small, allowing the energy deposited by photons and particles to be measured with great precision. Among all the

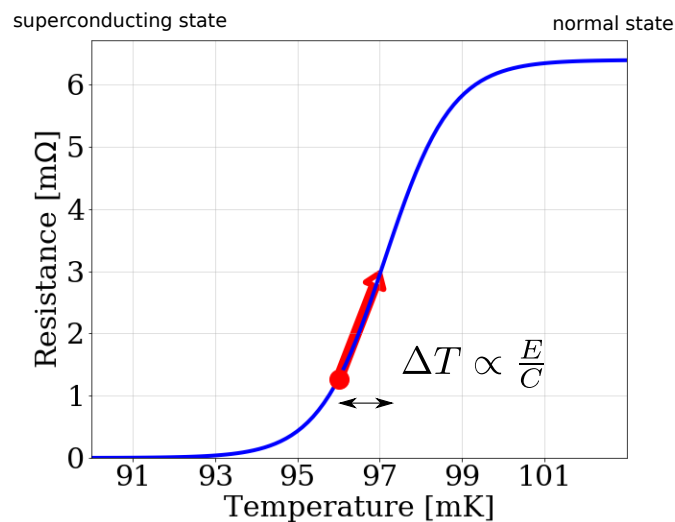


FIGURE 3.1: Transition shape of a TES similar to the ones adopted by Holmes

types of LTDs, superconducting Transition Edge Sensors (TES) combine the superior resolving power of wavelength dispersive techniques (the energy of single photons can be measured with resolving powers $E/\Delta E > 10^3$ in the case of x-rays and gamma-rays) with a large collection capability, a relatively high speed and established multiplexing schemes. In particular, the success of the microwave multiplexing techniques made this device suitable for a calorimetric neutrino mass experiment such as Holmes, for which the activity

per detector must be set to maximize the number of recorded events while keeping a feasible fraction of pile-ups.

A superconducting Transition Edge Sensor is a sensitive thermometer, consisting of a type I superconductor film operated in the narrow temperature region between the resistive and the superconducting state. When an energy deposit occurs, the temperature change is converted into a resistance variation of the film (Figure 3.1). When voltage-biased, thanks to the steep dependence of the resistance on T , an increase of R causes a measurable drop in the bias current, which is the actual measured physical quantity. Therefore, a measurement of the current variation is a measurement of the energy.

Altogether, the detector of Holmes is made of a structure that can absorb the interacting radiation and convert its energy into heat (the absorber), a structure that transduce heat into a measurable signal (the TES thermometer) and another structure that isolates them from the outside world, temporarily confining the energy in a finite body to be precisely measured (the Si_2N_3 membrane) and allowing to recover the idle temperature after an event.

In this chapter I will describe the functioning of each of the detector components alongside the multiplexing system (section 3.2) that will allow to read as many as 1000 detectors operated at temperature of a few tens of mK.

I will also focus on the characterization of the particular features of the single Holmes detector (section 3.3). In the last part (3.4), I will describe the various phases that the detectors array have to undergo to be suitable for a calorimetric neutrino mass measurement.

3.1.1 Small signal approximation

Predicting the TES response is important not only from a design point of view but also for defining the initial conditions that guarantee the best performance, while understanding its behavior during the measurement.

The complexity of the physics of a metal across its transitions from resistive to superconducting state limits the ability to predict the behavior of the detector. In order to fully describe the TES response it is necessary to know the shape of the surface $R(I, T, B)$, where R is the resistance, T is the temperature, I is the current and B is the local magnetic field¹. In the small signal approximation, which holds when the resistance shift due to an absorbed photon is small compared to the quiescent TES resistance, R_{tes} can be linearized with a first order Taylor expansion. In this case, the complexity of the resistive transition is enclosed in these two logarithmic derivatives

$$\begin{aligned}\alpha &\equiv \left. \frac{\partial \log R}{\partial \log T} \right|_{I_0} = \frac{T_0}{R_0} \left. \frac{\partial R}{\partial T} \right|_{I_0} \\ \beta &\equiv \left. \frac{\partial \log R}{\partial \log I} \right|_{T_0} = \frac{I_0}{R_0} \left. \frac{\partial R}{\partial I} \right|_{T_0}\end{aligned}\tag{3.2}$$

that can be evaluated at a particular bias point and as a consequence it is possible to write an analytical solution to the differential equations that describe the electrical and thermal circuit of the detector.

Figure 3.3 compares the TES response at different photon energies in the analytical small signal approximation (dotted line) vs the numerical solution which takes into account a more complex shape for the R_{tes} . Even if the small signal approximation can not be used to precisely predict the detector response, this model gives useful information about the parameters of the signal (signal height, rise time, decay time...) and, most importantly, the noise spectrum and the expected energy resolution.

¹Usually the latter dependence is negligible, therefore I will neglect it from now on

In the following I am going to describe quantitatively the shape of the current signal as predicted by the Irwin-Hilton model [52], which uses the small signal approximation and consider the TES thermometer and the absorber as a single body with one heat capacity and one thermal conductance though the thermal bath G .

In order to voltage bias the TES, the circuit shown in Fig 3.2 is used. It is composed of a shunt resistor R_{SH} in parallel with the TES resistance and the inductance L . The Thevenin-equivalent circuit is shown in Figure 3.2 b), with $R_L = R_{SH}$.

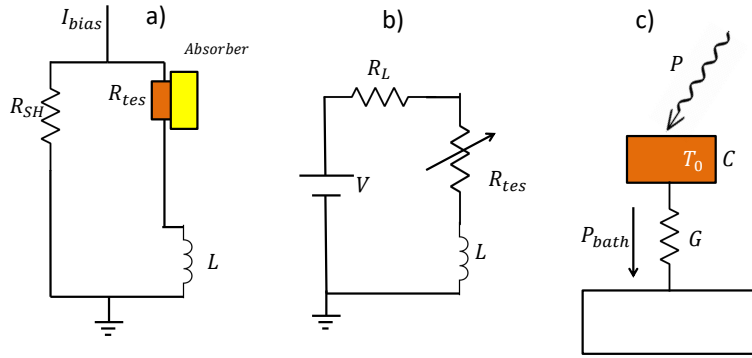


FIGURE 3.2: a) the TES bias circuit. b) The thevenin-equivalent circuit of a). c) A schematic view of the thermal circuit of the TES used in this section.

Ignoring the noise terms, the response of the TES is governed by two coupled differential equations describing the electrical and thermal circuit:

$$\begin{aligned} C \frac{dT}{dt} &= -P_{bath} + P_J + P \\ L \frac{dI}{dt} &= V - IR_L - IR_{tes} \end{aligned} \quad (3.3)$$

where C is the heat capacity (given by the sum of both the TES and the absorber), T is the temperature of the TES (the state variable), P_{bath} is the power flowing from the TES to the thermal bath, P_J is the Joule power dissipation and P is the signal power. In the second equation L is the inductance, V is the Thevenin-equivalent bias voltage, I is the electrical current flowing through the TES and $R_{tes}(T, I)$ is the electrical resistance of the TES.

The thermal and electrical circuits of a TES are coupled due to the cross terms in the thermal-electrical differential equations. In other words: a temperature signal in a TES is translated to an electrical current signal by the change in the resistance of the TES. In turn, the electrical current signal in the TES generates a Joule power dissipation in the TES itself. This process is called negative electrothermal feedback (ETF) in voltage-bias condition ($R_L \ll R_{tes}$), because the feedback acts when the resistance increases and the current drops in the TES branch of the circuit. In this regime, the reduction in Joule power $P_J = V^2/R_{tes}$ due to the resistance increase acts as a restoring force. One of the striking and useful consequence of the negative ETF is that the TES is maintained stable against thermal runaways because when the temperature is increased, the drop in Joule power restores the device at its original working point.

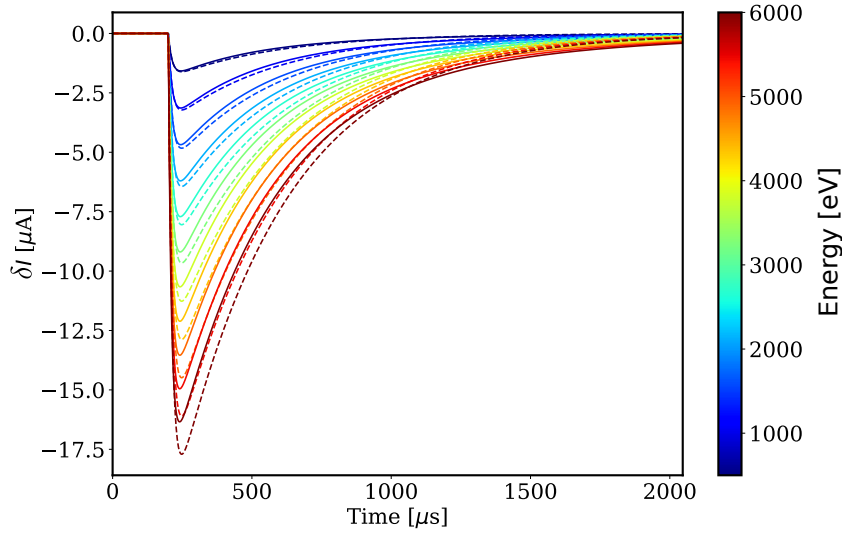


FIGURE 3.3: Comparison between the TES response at different photon energy in the analytical small signal approximation (3.14) (dotted line) vs the numerical solution of (3.3) which takes into account a more complex shape for the R_{tes} . The TES parameters are taken from one of the Holmes measured detectors.

Several nonlinear terms complicate the equations (3.3):

$$\begin{aligned} P_{bath} &= K(T^n - T_{bath}^n) \\ R_{tes} &= R_{tes}(T, I) \\ P_J &= I^2 R_{tes} \end{aligned} \quad (3.4)$$

where $n = \beta + 1$, β is the thermal conductance exponent while G is the differential thermal conductance $G \equiv \frac{dP_{bath}}{dT}|_{T_0} = nKT_0^{n-1}$. In the small-signal limit these terms can be linearized around the steady state values R_0, T_0, I_0 .

$$P_{bath} \sim P_{bath_0} + G(T - T_0) = P_{bath_0} + G\delta T \quad (3.5)$$

$$R_{tes}(T, I) \sim R_0 + \frac{\partial R}{\partial T}|_{I_0}\delta T + \frac{\partial R}{\partial I}|_{T_0}\delta I \quad (3.6)$$

With α and β defined in (3.2) describing the TES logarithmic sensitivity to a temperature change (α) and to a current change (β).

The equation (3.6) becomes

$$R(T, I) \sim R_0 + \alpha \frac{R_0}{T_0}\delta T + \beta \frac{R_0}{I_0}\delta I \quad (3.7)$$

Finally P_J can be expanded as

$$P_J \equiv I^2 R \sim P_{J_0} + 2I_0 R_0 \delta I + \alpha \frac{P_{J_0}}{T_0}\delta T + \beta \frac{P_{J_0}}{I_0}\delta I \quad (3.8)$$

Substituting (3.4), (3.8), (3.5) and (3.7) into eq (3.3) and substituting the small-signal value for the state variables $T \rightarrow \delta T = T - T_0$, $I \rightarrow \delta I = I - I_0$ we obtain the linearized

differential equations:

$$\begin{aligned}\frac{d\delta I}{dt} &= -\frac{R_L + R_0(1 + \beta_I)}{L}\delta I - \frac{\mathcal{L}_I G}{I_0 L}\delta T + \frac{\delta V}{L} \\ \frac{d\delta T}{dt} &= -\frac{I_0 R_0(2 + \beta_I)}{C}\delta I - \frac{(1 - \mathcal{L}_I)}{\tau}\delta T + \frac{\delta P}{C}\end{aligned}\quad (3.9)$$

Where

$$\mathcal{L}_I \equiv \frac{P_{J_0} \alpha_I}{G T_0} \quad (3.10)$$

$$\tau \equiv \frac{C}{G} \quad (3.11)$$

$\delta P = P - P_0$ represents small-power signals around a steady-state power load P_0 and $\delta V = V_{bias} - V_0$ represents small changes in the voltage bias around the steady-state value V_0 . Note that when $\mathcal{L}_I \gg 1, \beta$ the TES is in the so called strong EFT regime.

It is convenient to introduce other definitions before showing the solutions of (3.9) in case of a delta-function pulse (such as an instantaneous energy deposition in the absorber)

$$\begin{aligned}\tau_I &\equiv \frac{\tau}{1 - \mathcal{L}_I} \\ \tau_{el} &\equiv \frac{L}{R_L + R_{dyn}}\end{aligned}\quad (3.12)$$

$$\tau_{\pm} = \left(\frac{1}{2\tau_{el}} + \frac{1}{2\tau_I} \pm \frac{1}{2} \sqrt{\left(\frac{1}{\tau_{el}} - \frac{1}{\tau_I} \right)^2 - 4 \frac{R_0 \mathcal{L}_I (2 + \beta_I)}{L\tau}} \right)^{-1} \quad (3.13)$$

Finally, the solution of (3.9) are:

$$\begin{aligned}\delta I(t) &= \left(\frac{\tau_I}{\tau_+} - 1 \right) \left(\frac{\tau_I}{\tau_-} - 1 \right) \frac{C \Delta T}{(2 + \beta_I) I_0 R_0 \tau_I^2} \frac{(e^{-t/\tau_+} - e^{-t/\tau_-})}{(1/\tau_+ - 1/\tau_-)} \\ \delta T(t) &= \left(-\left(\frac{1}{\tau_I} - \frac{1}{\tau_+} \right) e^{-t/\tau_-} + \left(\frac{1}{\tau_I} - \frac{1}{\tau_-} \right) e^{-t/\tau_+} \right) \frac{\Delta T}{(1/\tau_+ - 1/\tau_-)}\end{aligned}\quad (3.14)$$

where τ_+ and τ_- represent the time constants for the TES response.

Noise and expected energy resolution

The response of a TES is affected by the thermodynamic fluctuations of its state variables. These noise sources set intrinsic limits to the energy resolution of a TES. The analysis of the noise is complicated by the nonlinear behavior of many circuit's elements. Therefore, some simplifications have to be done.

Following [52], I will report the expression for three important noise sources in the TES circuit. The noise for the TES resistance was obtained through a so-called nonlinear equilibrium ansatz (NLEA) that incorporates the effects of a current-dependent resistance ($\beta \neq 0$) but does not incorporate the effect of a temperature dependence resistance ($\alpha = 0$).

First, the detector responsivity, that is the current and temperature fluctuation amplitudes due to a power fluctuation amplitude, has to be calculated in the case of a small, sinusoidal

power load of the TES circuit at angular frequency ω :

$$\begin{aligned} s_I(\omega) &= -\frac{1}{I_0 R_0} \frac{1}{(2 + \beta_I)} \frac{(1 - \tau_+ / \tau_I)(1 - \tau_- / \tau_I)}{(1 + i\omega\tau_+)(1 + i\omega\tau_-)} \\ s_T(\omega) &= \frac{1}{G} \frac{\tau_+ \tau_-}{\tau^2} \frac{(\tau / \tau_+ \tau / \tau_- + \mathcal{L}_I - 1 + i\omega\tau)}{(1 + i\omega\tau_+)(1 + i\omega\tau_-)} \end{aligned} \quad (3.15)$$

Then, the noises of the main sources can be expressed in terms of power-spectral-density:

- The Johnson noise associated with the TES electrical resistance placed at a temperature T_0 .

$$S_{I_{TES}}(\omega) = 4k_B T_0 I_0^2 R_0 \frac{\xi(I)}{\mathcal{L}_I^2} (1 + \omega^2 \tau^2) |s_I(\omega)|^2 \quad (3.16)$$

where $s_I(\omega)$ is the responsivity (3.15). $\xi(I)$ is a parameter characteristic of the resistance, which takes into account its nonlinearity with respect to current variation; in the quadratic approximation $\xi(I) = 1 + 2\beta$.

- The Johnson noise due to the load resistor

$$S_{I_L}(\omega) = 4k_B T_L I_0^2 R_L \frac{(\mathcal{L}_I - 1)^2}{\mathcal{L}_I^2} (1 + \omega^2 \tau_I^2) |s_I(\omega)|^2 \quad (3.17)$$

where T_L is the temperature of R_L .

- The thermal fluctuation noise (TFN)

$$S_{I_{TFN}}(\omega) = 4k_B T_0^2 G \times F(T_0, T_{bath}) |s_I(\omega)|^2 \quad (3.18)$$

This is the noise term due to thermodynamic fluctuations across the thermal conductance G . $F(T_0, T_{bath})$ is a unit-less function that typically lies between 0.5 and 1 and that includes the nonlinear correction to the power spectral density due to the nonlinear thermal conductance $G(T)$.

Finally, the total spectral power density is given by

$$S_I(\omega) = S_{I_{TES}}(\omega) + S_{I_L}(\omega) + S_{I_{TFN}}(\omega) \quad (3.19)$$

Now it is possible to evaluate the energy resolution in terms of the FWHM. Following the limit in which $R_L \simeq 0$ and in the strong electrothermal regime, the energy resolution can be expressed as [52]

$$\Delta E_{FWHM} = 2\sqrt{2 \ln 2} \sqrt{\frac{4k_B T_0^2 C}{\alpha_I} \sqrt{\frac{n\xi(I)F(T_0, T_{bath})}{1 - (T_{bath}/T_0)^n}}} \quad (3.20)$$

However, there are additional unexplained noise sources that degrade the performance of a TES from this intrinsic limit (3.20). I will just enunciate them.

The *Internal thermal fluctuation noise* (ITFN) is due to the thermal circuit model, in particular it takes into account the distribution of the heat capacities and conductance inside the TES. The *Excess electrical noise* has the same frequency dependence as the TES Johnson noise and tends to be worse for lower detector normal resistance and when biased lower in the transition. It is also a strong function of the applied magnetic field. There is no universally accepted theoretical explanation for this noise.

Lastly, the *Excess low frequency noise*, sometimes with a $1/f$ dependence. It is often correlated with strong excess electrical noise.

3.1.2 Large signal and resistance models

Recently, two models have been developed to describe distinctly different observed TES behavior, depicting at the same time the resistive mechanism underlying the superconducting thermometer operating in its transition region².

One is based on the resistively shunted junction (RSJ) model by Kozorezov et al [54], called the *weak-link model*, applicable to smaller devices where the length of the thermometer is few times the superconducting coherence length, while the other [55] is related to the concept of Phase Slip Center (PSC) observed in whiskers, micro-bridges and nanowire, which I will refer to as *PSL two fluid model*, and it is applicable to larger devices.

To assess the length scale, [53] shows that for MoCu with Mo leads square TESs (the same as the one of Holmes), devices below $80 \mu\text{m}$ tends to follow the weak-link explanation, while above $80 \mu\text{m}$ the measured value are consistent with the *PSL two fluid model*. The Holmes TESs being, as we will see, $125 \times 125 \mu\text{m}^2$ devices, should fall in the latter classification.

The idea behind the *PSL two fluid model* is that in the thermometer localized regions called Phase Slip Lines (PSLs) may exist, in which the current is carried by both a normal and a superconducting current. The PSL is the 2D analogue to PSC [56], spatially localized region in mono-dimensional superconducting wire in which the phase of the superconducting order parameter is increasing at different rates on the two sides of the PSC.

A simplified version of this model, proposed by [57] [58], express the TES resistance as

$$R_{tes}(I, T) = c_R R_n \left(1 - c_I \frac{I_c(T)}{I} \right) \quad (3.21)$$

where c_R and c_I are two phenomenological parameters (considered constant), R_n is the normal resistance of the TES and I_c is the critical current that from the standard G-L theory has the form

$$I_c(T) = I_{c0} \left(1 - \frac{T}{T_c} \right)^{3/2} \quad (3.22)$$

where I_{c0} is the value of I_c at zero temperature.

Equation (3.21) describes only a small portion of the real R_{tes} curve, because the coefficients are fixed. To give a description of the whole transition, while giving an explanation on the underlining mechanism, a more complex model is required.

This was initially developed by Skocpol-Beasley-Tinkham [55] [59] for superconducting filaments and later extended by Bennet to voltage-biased two dimensional films, i.e. Transition Edge Sensors [60]. Here I will just present the main achievements of this model, alongside with its predictions.

When a current I is flowing through the TES, a number n_{ps} of equally spaced PSL will appear, resulting in a voltage drop equal to

$$V_n = \frac{2n_{ps}\Gamma_{Q^*}}{L} R_n (I - c_I I_c(T)) \tanh\left(\frac{L}{2n\Gamma_{Q^*}}\right) \quad (3.23)$$

with Γ_{Q^*} the length scale of the phase-slip, c_I the fraction of the total current carried by the local super current and L the length of the device. When the local super current at any

²Further details can be found in [53]

time exceed I_c , a new phase-slip is formed. Thus, for n_{ps} there exist a maximum current given by

$$I_{max,n} = I_c \frac{\cosh[L/(2(n_{ps} + 1)\Gamma_{Q^*})] - c_I}{\cosh[L/(2(n_{ps} + 1)\Gamma_{Q^*})] - 1} \quad (3.24)$$

When the TES is voltage biased and in thermal equilibrium, there are specific values of I_t (the bias current) or T for which the equations

$$\begin{aligned} (I_t - I)R_s &= V_n(I, T) \\ IV_n(I, T) &= k(T^n - T_b^n) \end{aligned} \quad (3.25)$$

predict both the existence of bi-modal current distribution, in which the current switches between distinct current states and the possibility of discrete variations of the TES current due to a sudden change of the PSL number n_{ps} .

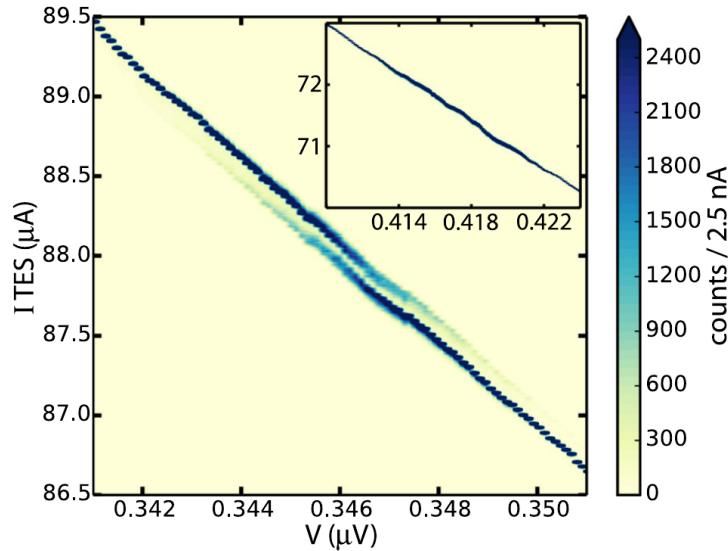


FIGURE 3.4: (From [60]) Example of a measured IV characteristic of a TES measured in the region of 38% R_n . At each bias voltage, 130000 measurements of the current are histogrammed to show the distribution of currents. The inset shows the IV in the region of 57% R_n .

The model also predicts that the current separation between states of different n_{ps} is larger at low resistance values and the existence of larger excursion of α_I at resistance values where the number of PSL changes.

As shown in Figure 3.5, the latter was observed in our detectors, with the consequent sudden change in the amplitude of the signal.

However, it was also observed another phenomenon which I can also be related to the PSL model: a sudden variation of the signal amplitude even when it is not related to an abrupt variation of the idle current. This variation lasts for several minutes, during which the signal amplitudes vs idle currents shows a different slope compared to the rest of the measurement (see chapter 4.3.3, Figure 4.9).

This might be due to the thermal drift of the bath temperature: the detector sometimes can end up in a stable state for which the path that follows after the energy deposition can substantially differ from the usual one due to the sudden variation of n_{ps} during the resistance change.

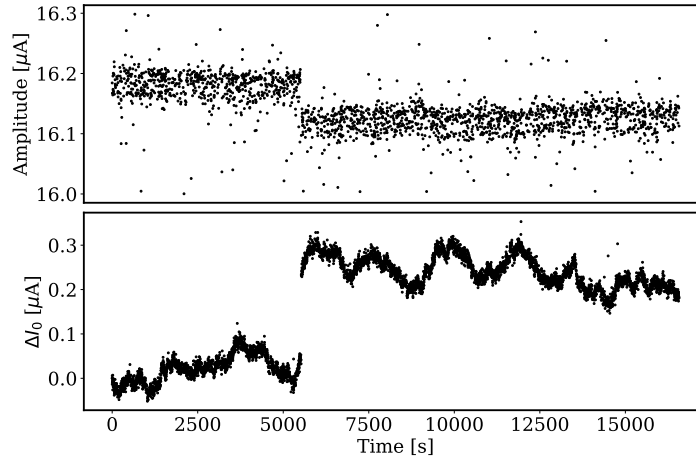


FIGURE 3.5: Example of a measured step change of the detector idle current probably due to a variation of n_{ps} . *Bottom*: each point represent the TES idle current on which the signal rise measured at different time. The oscillating behavior is expected due to the detector thermal drift. *Top*: The resulting signal amplitude due to a X-ray interaction in the absorber at the same instants. The signal amplitude changes abruptly with the idle current due to the different detector starting condition, resulting in a signal with different shape.

As a final note, I want to point out that even if the *PSL two fluid model* seems to be the correct one to describe the physics behind the detector behavior, for simplicity I used another empirical relation characterizing the R_{tes} curve to simulate the TES response given by Cabrera [61], which so far described correctly the Holmes measured signal shape for a large class of detector geometries over a relative large energy range (see chapter 6.2)

$$R_{TES}(T, I) = \frac{R_N}{2} \left[1 + \tanh \left(\frac{T - T_C + (I/A)^{2/3}}{2 \log(2) T_W} \right) \right] \quad (3.26)$$

with A and T_W given by the known α and β and the idle conditions.

3.2 Microwave Multiplexing readout

A calorimetric neutrino mass experiment, like Holmes, requires a very fast signal time profile, around few hundreds of microsecond, in order to facilitate the pile-up rejection while reducing the dead time. This calls for a readout that can satisfy both the requirements of a large bandwidth and a high multiplexing factor, i.e. the number of detectors that can be readout with a single readout element. In fact, without multiplexing the number of pairs of wires required to operate the TESs are of the order of few thousands [62] for the final Holmes configuration, resulting in unmanageable heat load at the cryogenic stage.

Microwave SQUID multiplexing (μ MUX) has the potential to meet those requirements compared to other readout techniques like time or frequency division multiplexing. With the μ MUX technique, the complexity is moved at the warm stage outside the cryostat, where it is possible to leverage high-bandwidth commercial components and implement many functions using software defined radio (SDR) techniques.

To explain how it works, at fist I will briefly present its two main components, the rf-SQUID and the quarter wave resonator, then I will focus on the particular features of the ones used in Holmes.

rf-SQUID and quarter wavelength resonator

For the typical operating resistance of the Holmes detector ($\mathcal{O}(2 \text{ m}\Omega)$), the current signal is of the order of few tens of microamps with noise fluctuations around $(100\text{-}200) \text{ pA}/\text{Hz}^{1/2}$. A low noise, low power and low impedance amplifier such as an rf-SQUID is required to preserve the signal in such small currents.

A rf-SQUID (Superconducting Quantum Interference Device) consists of a superconducting loop interrupted by a single insulating tunnel barrier, called a Josephson junction. These devices are sensitive magnetometers which measure the magnetic flux, with a noise of few $\mu\Phi_0/\text{Hz}$, where $\Phi_0 = 2 \times 10^{-15} \text{ Wb}$ is called the quantum magnetic flux, that results in a current noise of around $20\text{-}40 \text{ pA}/\text{Hz}$, well below the TES current noise of Holmes [62].

The dissipationless rf-SQUID used in Holmes is depicted in Figure 3.6.

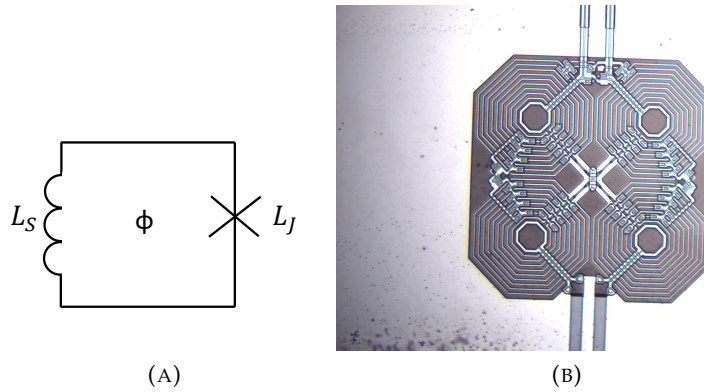


FIGURE 3.6: (A)Simplified scheme of the rf-SQUID. (B) picture of the Holmes rf-SQUID part of the readout chip $\mu\text{Mux}17\text{a}$. The orientation of the lobes alternates around the SQUID making it insensitive to first order gradients and to uniform magnetic fields.

When the self-inductance of the circuit L_S is such that $L_S/L_J < 1$ [63], this device acts as a sensitive magnetometer. If a variable magnetic flux Φ crosses the circuit 3.6, a voltage difference will appears on both side on the Josephson Junction and an AC current I will flow due to the tunnel effect

$$\begin{aligned} \frac{2eV}{\hbar} &= \frac{d\phi}{dt} \\ I &= I_c \sin(\phi) \end{aligned} \quad (3.27)$$

I_c is the critical current of the superconductor and ϕ is the phase difference of the Cooper's pairs wave function across the junction. In the small signal limit³, the junction acts as an inductance

$$L(\phi) = L_J \sec(\phi) ; L_J \equiv \frac{\hbar}{2eI_c} = \frac{\Phi_0}{2\pi I_c} \quad (3.28)$$

³i.e. low power probe tone

The phase difference of the Copper's pairs wave function ϕ becomes proportional to the magnetic flux

$$\begin{aligned}\phi &= \frac{2e}{\hbar} \int \left(\frac{d\Phi}{dt} \right) dt \\ &= 2\pi \frac{\Phi}{\Phi_0}\end{aligned}\quad (3.29)$$

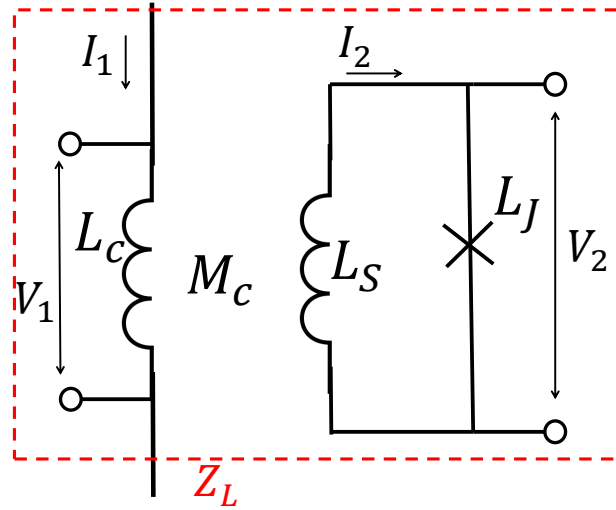


FIGURE 3.7: Example of a circuit used to readout the rf-SQUID

As a consequence, the impedance Z_L (and in particular the inductance) of a typical circuit branch used to readout the rf-SQUID (Fig 3.7) varies with the magnetic flux:

$$\begin{aligned}Z_L &= i\omega L(\Phi) \\ L(\Phi) &= L_c - \frac{M_c^2}{L_s} \frac{(L_s/L_j)\cos(2\pi\Phi/\Phi_0)}{1 + (L_s/L_j)\cos(2\pi\Phi/\Phi_0)}\end{aligned}\quad (3.30)$$

In order to measure the variation of the inductance $L(\Phi)$, i.e. to measure the magnetic flux, the impedance Z_L is coupled to a quarter wavelength resonator, as showed in Figure 3.8.

An ideal quarter wavelength resonator is a dissipation-less transmission line that allows the transmissions of only signals with frequency $f_1 = \frac{v_p}{l}$, where l is the length of the line and v_p is its phase velocity.

In the circuit 3.8, similar to the one used in the μ MUX, a quarter wave resonator having an impedance Z_1 contributes to the total circuit impedance Z as

$$Z = Z_1 \left(\frac{Z_L + iZ_1 \operatorname{tg}\left(\frac{\omega l}{v_p}\right)}{Z_1 + iZ_L \operatorname{tg}\left(\frac{\omega l}{v_p}\right)} \right)\quad (3.31)$$

The resonator is capacitively coupled with a capacitance C_c to a feed-line, along which all the frequencies different from f_1 will be transmitted unaffected by the presence of the resonator.

If Z_L is the impedance of the SQUID readout circuit in Fig 3.7, it is possible to measure the variation in the magnetic flux that passes through the rf-SQUID by observing the variation

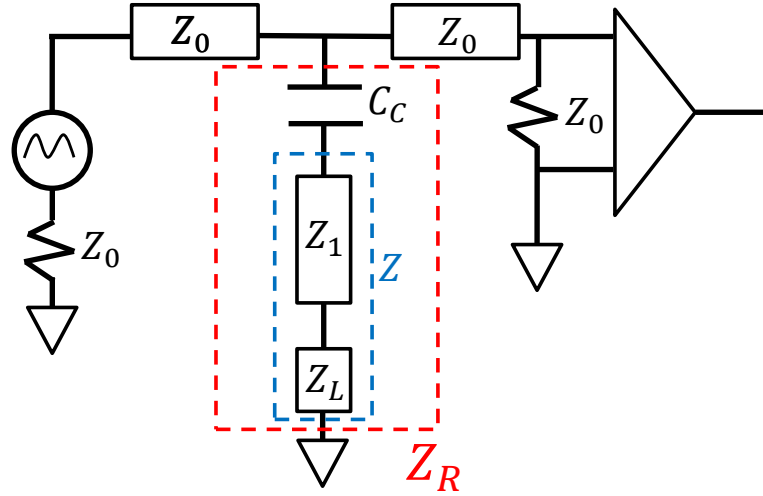


FIGURE 3.8: Circuit of a quarter-wave resonator.

in the resonant frequency of the circuit, as shown in Figure 3.9. The total impedance Z_R of the circuit branch is

$$Z_R = \frac{1}{i\omega C_c} + Z_1 \frac{i\omega L(\Phi) \cot(\omega \frac{L}{v_p}) + iZ_1}{Z_1 \cot(\omega \frac{L}{v_p}) - \omega L(\Phi)} \quad (3.32)$$

therefore, assuming $1/(\omega C_c) \gg Z_1$ and $2\pi f_1 L \ll Z_1$, the resonant frequency f_0 of the resulting circuit becomes sensitive on the magnetic flux

$$\begin{aligned} f_0(\Phi) &= \frac{f_1}{1 + 4f_1 C_c Z_1 + 4f_1 L / Z_1} \\ &\sim f_1 - 4f_1^2 C_c Z_1 - \frac{4f_1^2 L_c}{Z_1} + \frac{4f_1^2 \lambda M_c^2}{Z_1 L_S} \cos\left(2\pi \frac{\Phi}{\Phi_0}\right) \end{aligned} \quad (3.33)$$

where M_c is the mutual inductance of Figure 3.7 while $\lambda = L_S / L_j$ of eq (3.30).

In conclusion, if a probe signal $V_{in} = V_0 e^{i\omega t}$ is sent into the circuit shown in Figure 3.8, a magnetic flux variation in the SQUID is evaluated by measuring the phase variation of the output signal of the circuit V_{out}

$$V_{out} = V_0 e^{i(\omega t + \delta)} \quad (3.34)$$

$$\delta = \delta(\Phi) = \arctan\left(\frac{Z_R(\Phi)}{2Z_0}\right) \quad (3.35)$$

As will be explained in the next section, the idea of this readout system is that a current variation in the TES is translated into a flux variation in the SQUID and finally into a phase variation of the RF-wave used to probe the resonator

μ MUX multiplexing with flux ramp modulation

The μ MUX readout chip is a device composed of a series of quarter wave resonators each one coupled to a rf-SQUID. Each resonator is designed to ring at a unique frequency. A SQUID is inductively coupled to a single TES circuit. In order to probe the resonators, a

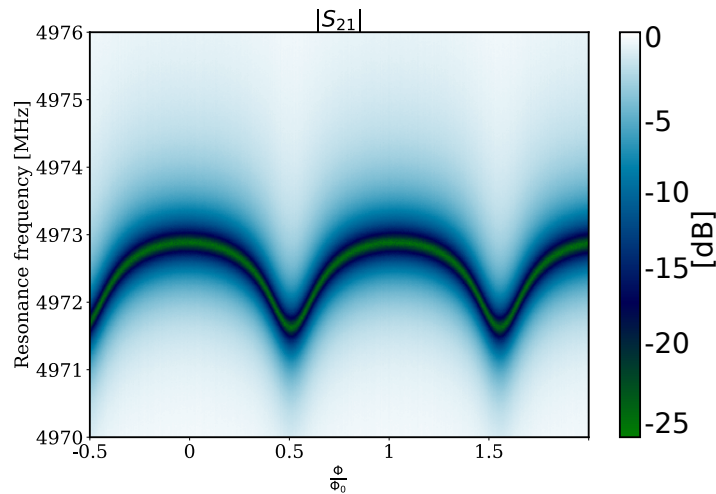


FIGURE 3.9: Example of the variation in the resonant frequency of one of the Holmes resonator due to a change in the magnetic flux of the corresponding SQUID. The transmission function S_{21} was acquired with a vector network analyzer.

comb of gigahertz signals matching the resonators frequencies is sent through the feedline in order to measure the phase difference between the output and the input.

However, as shown in Figure 3.9, the SQUID response to the variation of the magnetic flux is a non-invertible function. Therefore a method called flux ramp modulation is used to linearize the SQUID response.

In this scheme, depicted in Figure 3.10, a common flux ramp signal is applied to all SQUIDs. The flux ramp is a sawtooth signal resetting at a frequency of f_{ramp} and with an amplitude that is set so that the SQUID will oscillate of a quantity equal to an integer number of flux quanta $n\Phi_0$, forcing the SQUIDs to make identical and periodic oscillation for each ramp period. For the Holmes setup, the ramp amplitude have been chosen so that it produces a two Φ_0 SQUID oscillations per ramp.

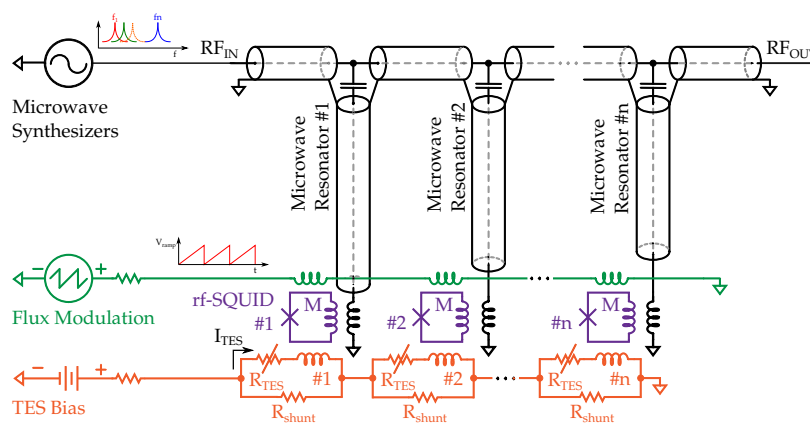


FIGURE 3.10: The circuit diagram of the Holmes multiplexed readout.

If the slew-rate of the applied ramp exceeds that of any input signal, a variation in the SQUID input signal, i.e. a variation in the TES current, will look like an offset of the phase in the periodic ramp-induced SQUID oscillation.

Note that to prevent artifacts in the demodulated data from unwanted transient behavior caused by the ramp reset, a fraction of each oscillations (~ 0.5) at the beginning of the ramp period is discarded.

Calling $S(t, \phi_i)$ the periodic SQUID response due to the flux ramp, the phase shift ϕ_i within the i^{th} - ramp period is proportional to the flux(current) variation in the TES

$$\phi_i = 2\pi \frac{\Phi_i}{\Phi_0} \quad (3.36)$$

The current $I(t)$ flowing through the TES is thus sampled at each ramp period ($I(t) \rightarrow I_i$) performing a simple Fourier measurement between $S(t, \phi_i)$ and $S(t, 0)$. Considering a purely sinusoidal SQUID response $S(t, 0) = \cos(2\pi n_{\Phi_0} f_{\text{ramp}} t)$, ϕ_i is measured as

$$I_i \propto \phi_i = \arctan \left(- \frac{\sum S(t, \phi_i) \sin(2\pi n_{\Phi_0} f_{\text{ramp}} t)}{\sum S(t, \phi_i) \cos(2\pi n_{\Phi_0} f_{\text{ramp}} t)} \right) \quad (3.37)$$

To sum up, with the flux ramp modulation microwave multiplexing it is possible to read out multiple detectors with a single line by coupling many resonator with different resonant frequency in the GHz range to a rf-SQUID, which in turn is inductively coupled to a specific detector. The warm electronics will be responsible to acquire the resulting rf-signal and split it into the various resonators frequencies while evaluating for each channel $S(t, \phi_i)$ and ϕ_i (I_i) with 3.37. The sampling frequency f_{samp} of the TES signals is thus given by the frequency of the ramp f_{ramp} .

μ MUX multiplexer chip for Holmes

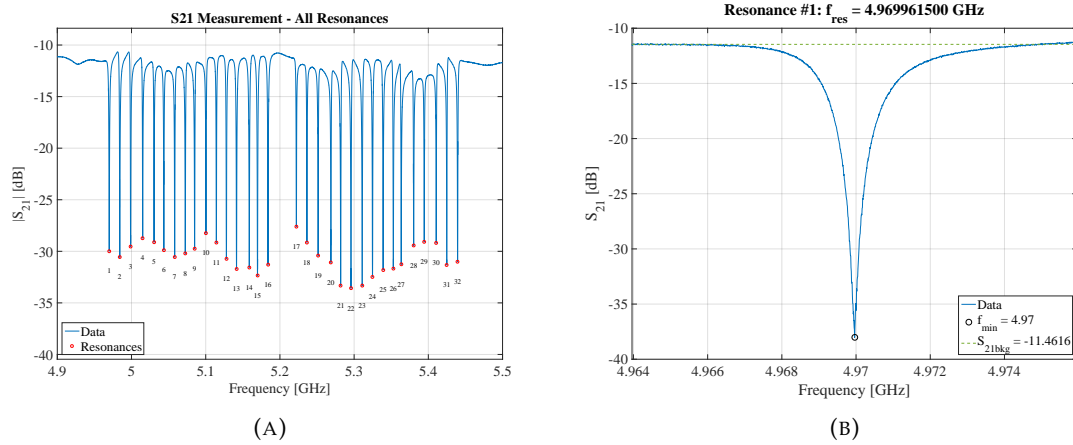


FIGURE 3.11: (A) Transmission function S_{21} for the chip μ Mux17a; each resonance dip is marked with a dot. One resonator was damaged and therefore its resonance is missing. (B) zoom on the first resonance of the chip.

The number of detectors that can be read simultaneously using one acquisition system (in the case of Holmes, a ROACH2, see 5.1.2) called the multiplexing factor N_{det} , is limited by the bandwidth BW of the acquisition system itself

$$N_{\text{det}} = \frac{BW}{f_{\text{sample}} \times n_{\Phi_0} \times K \times 2} \quad (3.38)$$

where n_{Φ_0} is the number of SQUID oscillations per ramp and K is a "guard factor" proportional to the resonance spacing, intended to avoid crosstalk between adjacent resonances

$$K = \frac{f_{res_{n+1}} - f_{res_n}}{BW_{res}} \quad (3.39)$$

f_{ramp} , thus f_{samp} , must be set in order to have a reasonable number of samples on the rise time of the TES pulse, $\mathcal{O}(10)$, while avoiding spoiling intrinsic energy resolution of the detector. In fact, if f_{ramp} is closer to the bandwidth of the resonator, the amplitude of the SQUID oscillations becomes lower, degrading the signal to noise ratio.

As a multiplexing chip, Holmes uses the $\mu\text{mux}17a$, a 33-channel multiplexing chip that has been developed and fabricated at the National Institute for Standard and Technology (NIST, Boulder, Co, USA).

It presents a total bandwidth of $BW = 550$ MHz, a resonance bandwidth of $BW_{res} \simeq 2$ MHz and $K = 7$, i.e. a resonance spacing of 14 Mhz.

With the target sampling frequency of 500 kHz and the required number of SQUID oscillations of two, the multiplexing factor is around $N_{det} \sim 39$. The performance of the multiplexing chip in terms of noise and signal reconstruction can be found in 5.

3.3 Holmes detectors design

In this section I will outline the final detector design of the Holmes detectors (see Figure 3.12, 3.13), which was identified after an intensive measurement campaign [64]. A sidecar geometry is adopted, in which the absorber is placed alongside the TES to avoid proximity effect with the thermal sensors which would modify the transition shape of the resistance.

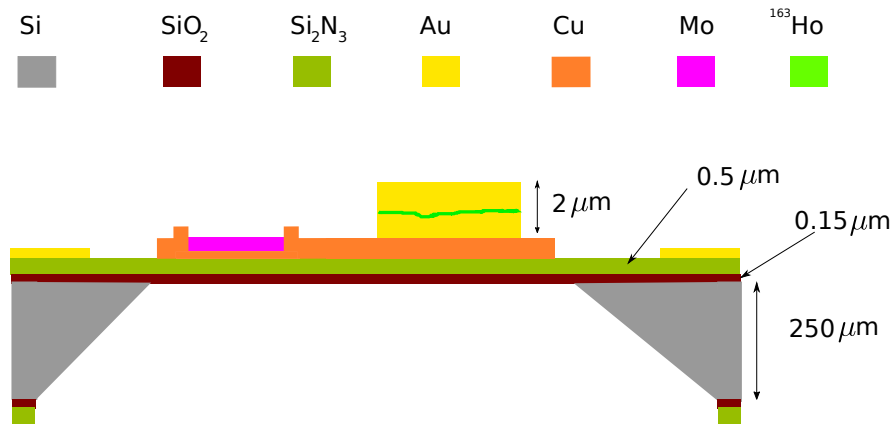


FIGURE 3.12: Sideview of the Holmes detector design. The thickness of the different material is reported. The figure is not to scale.

The TES thermal sensor is made of a superconductor-normal metal bilayer Molybdenum-Copper. With this structure, the Mo critical temperature T_c is suppressed from its bulk value of ~ 920 mK to 100 mK. The bilayer has a surface of $125 \times 125 \mu\text{m}^2$ and it is shaped using copper bars orthogonal to the current flow. This provides numerous advantages: first of all it allows to tune the normal resistance R_n and the dynamic range of the sensors to meet the required value, then it has been shown that these bars reduce also the excess electrical noise [65].

An ideal absorber should combine high stopping power, low heat capacity and good thermalization properties. Therefore, for Holmes a $200 \times 200 \times 2 \mu\text{m}^3$ gold absorber is chosen. When the Holmium decays, the de-excitations products (auger electrons and X-rays, which are converted typically by photoelectric effect to a single hot photoelectron) relaxes by electron-electron and electron-phonon scattering with the surrounding. The probability that the electrons (photons) from the ^{163}Ho decay are stopped is predicted to be 99.99% (96.73%) for the chosen thickness.

The relaxation process lasts for a fraction of nanoseconds and leads to a partitioning of the energy between electrons and phonons. Due to the fact that the Au absorber is deposited on top of a copper structure with a bar connecting it to the thermometer, the absorber temperature is strongly linked to the sensors one via the electron system, ensuring the thermal equilibrium between the two.

The detector thermal isolation is necessary to tune the signal time profile, matching the bandwidth of the readout system. Holmes achieve the thermal isolation by placing the detector on top of a suspended Si_2N_3 membrane, which strongly limits the phonon transport to the heat bath, avoiding the escape of hot phonons during the thermalization process which would result in signal loss, while providing mechanical strength.

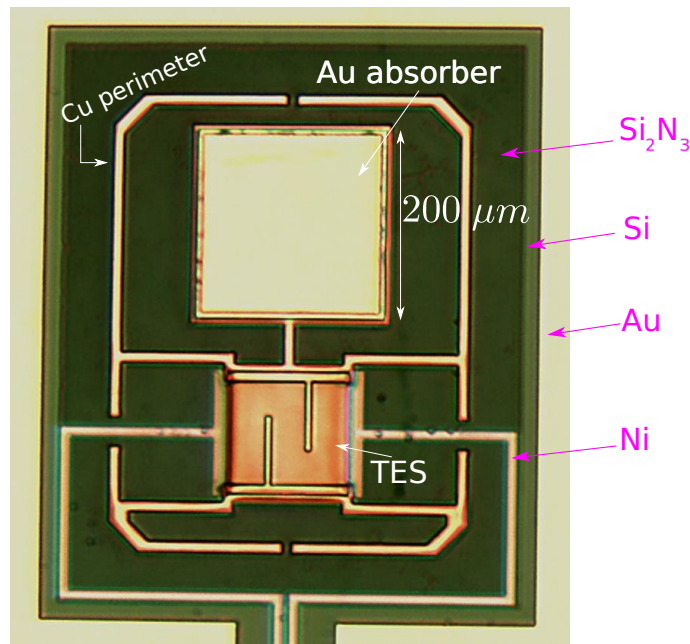


FIGURE 3.13: Topview of the Holmes detector design.

The thickness of the membrane is $\sim 500 \text{ nm}$, which is close to the predicted value for the 3D-2D phonon propagation crossover of $\lambda_c \simeq \hbar c_t / (2k_B T) \sim 300 \text{ nm}$ for a transversely sound velocity c_t of 6200 m/s [66] at a temperature T .

Due to the target single pixel activity, the Holmes detectors should have a fast recovery time to reduce the experimental dead-time. In the 2D regime, the power flows to the heat bath from the perimeter of the radiating body, therefore an additional perimeter is created out of a thin copper trace. This has been demonstrated to increase the G value while having a negligible effect on heat capacity, i.e. the energy resolution [67].

The thin gold layer deposited in the surroundings of the detectors is wire-bonded to a cold thermal bath. This, in combination with the Si_2N_3 membrane and the copper perimeter, should ensure a thermal conductance of the value of $\sim 600 \text{ pW/K}$.

3.3.1 Modelling the thermal circuit

As many others microcalorimeter designs, the Holmes detector response have been experimentally shown to behave in a more complex manner than the one predicted by the one body model of section 3.1.

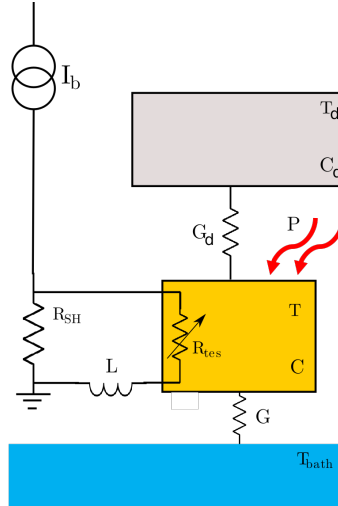


FIGURE 3.14: TES two-body 'dangling' model scheme.

With the detector design described in the previous section, the thermal circuit depicted in Figure 3.14 predicts the measured TES signal shape in a more realistic manner. In this new model, sometimes indicated as the *dangling model* [68], an extra heat capacity C_d is connected to the TES heat capacity C through a thermal conductance G_d . The electrothermal differential equations to be solved now are

$$\begin{aligned} C \frac{dT}{dt} &= -K(T^n - T_b^n) - K_d(T^{n_d} - T_d^{n_d}) + P_J + P \\ C_d \frac{dT_d}{dt} &= K_d(T^{n_d} - T_d^{n_d}) \\ L \frac{dI}{dt} &= V - IR_L - IR_{tes} \end{aligned} \quad (3.40)$$

The main consequence is that the TES signals are now described by three time constants instead of two. Solving eq (3.40) numerically, with R_{tes} given by (3.26) and with the detector parameters close to the expected ones, results in simulated pulses very close to the ones observed over the whole dynamic range of the detector (see Figure 6.18).

I want to stress out that even if the TES time profile is described by eq (3.40), the measured noise spectrum doesn't show any significant bump. This is probably related to the level of the Holmes readout noise, in combination with the fact that $C_d/C < 0.5$ [68]. As a consequence, the noise spectrum of the Holmes detectors are described well with the one body noise spectrum of eq (3.19).

3.3.2 The heat capacity problem

At the time of the writing of this thesis, the ^{163}Ho is not implanted inside the gold absorber. The total detector heat capacity is thus expected to be $C = C_{abs} + C_{tes} \simeq 0.8$ pJ/K at 100 mK, with C_{abs} the absorber heat capacity of 0.55 pJ/K and $C_{tes} \sim 0.25$ pJ/K. In chapter 5 I will prove that our current detectors have indeed met the Holmes requirements in terms

of energy resolution, resulting an energy resolution FWHM of ~ 4 eV at ~ 6 keV, a factor two lower than the one required for achieving a neutrino mass sensitivity of $\mathcal{O}(eV)$.

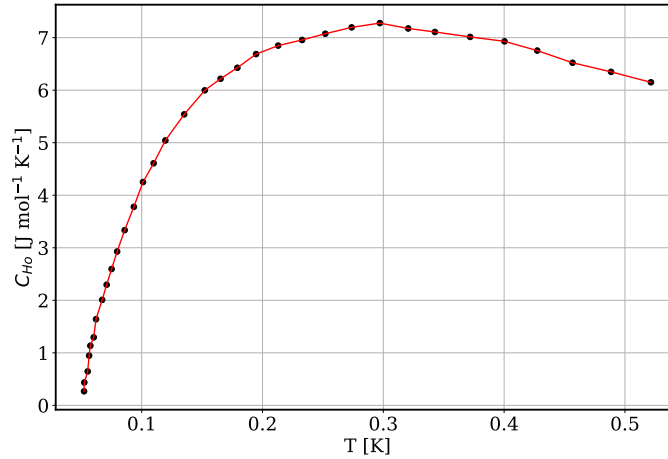


FIGURE 3.15: Specific heat of bulk Holmium metal versus temperature from [69]

However, hyperfine interactions in rare-earth elements such as Holmium, have shown that their heat capacity do not decrease with temperature as the other metals commonly do, but feature a peak at low temperature. This phenomenon is called Schottky anomaly, and it has been measured in a pure metallic Ho sample [69], resulting in the trend showed in Figure 3.15.

With the Holmium implanted, the detector heat capacity will be $C = C_{abs,Au} + C_{tes} + C_{abs,Ho}$. If the $C_{abs,Ho}$ should have the same temperature trend and magnitude as the the bulk metallic Holmium, the absorber heat capacity would be soon dominated by the Holmium atoms rather than the gold one, resulting in degradation of the energy resolution that, in the worst case scenario, could be worsen by roughly a factor of 2 for an Holmium activity per pixel of 1 Bq. The predicted difference in the signal shapes can be seen in Figure 3.16.

Even if this effect was not observed in [70] with Ho implanted in gold, the recent work [71] made by the Echo collaboration seems to suggest otherwise, at least to some extent.

In principle, $C_{abs,Ho}$ depends on the implantation process, on the absorber material and on the chemical species of the implanted ^{163}Ho , pure metallic Ho or Ho oxide. Therefore, the $C_{abs,Ho}$ is a crucial parameter that has to be assessed for our specific implantation setup.

3.4 Holmes array fabrication

The Holmes detectors have to undergo different fabrication steps in order to have the ^{163}Ho implanted inside the gold absorbers. The detector arrays used for preliminary test measurements initially had pixels with different geometries and were fabricated at NIST with $2 \mu\text{m}$ thick gold absorbers while the membrane suspension was achieved with a Silicon DRIE etching procedure.

The first stage of the Holmes measurement campaign is now approaching, for which the detector array fabrication have to undergo a different fabrication procedure, as illustrated in Figure 3.17. The detectors production will be split in two steps: the first one will be carried out at NIST, where a first $1 \mu\text{m}$ thick of gold will be deposited, in the second

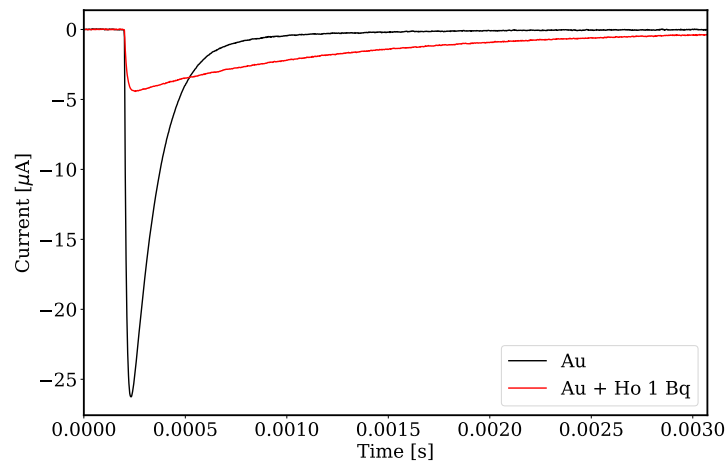


FIGURE 3.16: Simulated signal with $E = 3000$ eV with and without the Holmium inside the absorber. The heat capacity was evaluated considering the implanted isotope (1 Bq) as bulk Holmium metal, using the data from [69]

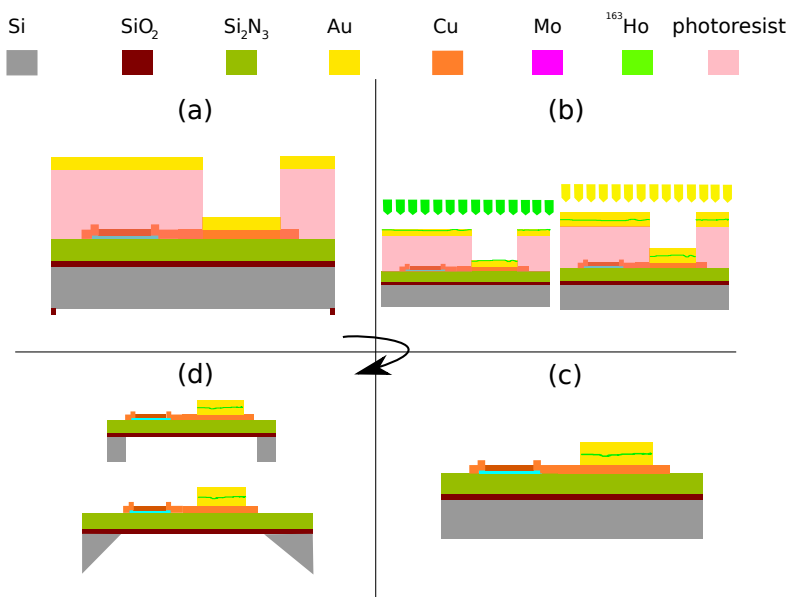


FIGURE 3.17: Scheme of the Holmes array fabrication procedure. Image (A) depicts the detector fabricated at NIST, while (B), (C), (D) the fabrication process that will be performed by the Genova groups.

step, which will be realized in Genova, the detectors will be finalized by embedding the ^{163}Ho and depositing the final $1\ \mu\text{m}$ gold layer. Finally, the detectors thermal isolation is achieved through the membrane release, that will be performed with a KOH or DRIE silicon etching.

The delicate steps of the fabrication chain have been intensively tested, and the results are reported in the following sections.

3.4.1 Au deposition test

After the step (A) in Figure 3.17, the detector array will be located at the end of the custom ion implanted inside a UHV chamber called the Target Chamber to perform a simultaneous ^{163}Ho implantation and gold deposition. The purpose of the target chamber is twofold: it will allow to control the ^{163}Ho concentration by co-evaporating gold while implanting, permitting also to compensate the unavoidable sputtering action of the implanting ^{163}Ho nuclei, and it will permit to deposit the final $1\ \mu\text{m}$ of gold in situ, avoiding to oxide the implanted holmium.

The target chamber performance in terms of gold deposition was tested separately from the custom ion implanter. The gold deposition rate has to be estimated alongside the uniformity of the process, optimizing at the same time the ion beam parameters.

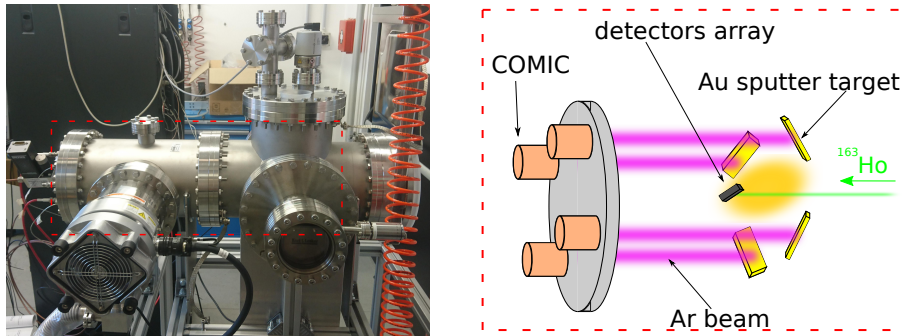


FIGURE 3.18: *Left:* Picture of the Target Chamber. *Right:* Scheme of the configuration of the 4 sputtering sources for the Au deposition.

To achieve a uniform gold deposition over the whole array, 4 Compact Microwave and Coaxial (COMIC [72]) source of ions are placed in high vacuum ($\sim 10^{-8}$ mbar). Each COMIC source is made of 4 antennas distributed inside a magnetic cylinder, creating an electric field that in combination with the decreasing magnetic field allows to ignite an argon plasma.

Different electrodes set an extraction voltage around 10 kV to create 4 focused Ar ion beams, one for each COMIC, hitting four different ultra pure gold target. These targets are tilted respect to the beams planes so that the spattered gold diffused preferentially toward the target (Figure 3.18). The gold deposition rate is measured with a quartz microbalance located near the target.

All the high voltage biased components are inside the vacuum box. The gas distribution along the different COMIC sources is done by a stainless steel ring which divides the total flux.

The system parameters (the argon flux, the COMIC microwave power, the extraction voltage) must be tuned to achieve a high and stable current. We manage to achieve a total current of $\sim 250\ \mu\text{A}$, which results in a gold deposition rate at the target of $52 \pm 4\ \text{nm/h}$ ($39 \pm 2\ \text{nm/h}$ at the microbalance). With this deposition rate, around 20 hours are needed to deposit the target $1\ \mu\text{m}$ of gold, which is suitable for the expected implantation rate of ^{163}Ho .

To test the uniformity of the gold deposition, the gold was sputtered for ~ 22 hours on a $1 \times 1\ \text{cm}^2$ silicon slab with a shadow mask with 9×9 holes on top, as depicted in Figure 3.20. This produces as many gold sputtered circular islands on the silicon underneath. The thickness in the center of the circles were measured with a profilometer. The spread of the measured thickness was about 40 nm RMS, which would result in a nearly uniform thickness for all the absorbers of the detector array.

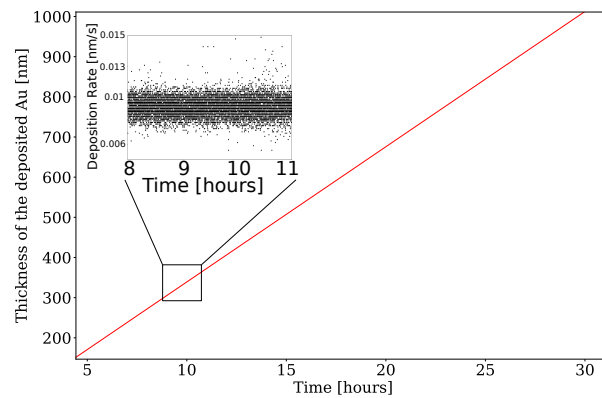


FIGURE 3.19: Time profile of the thickness of the gold deposited on the target.

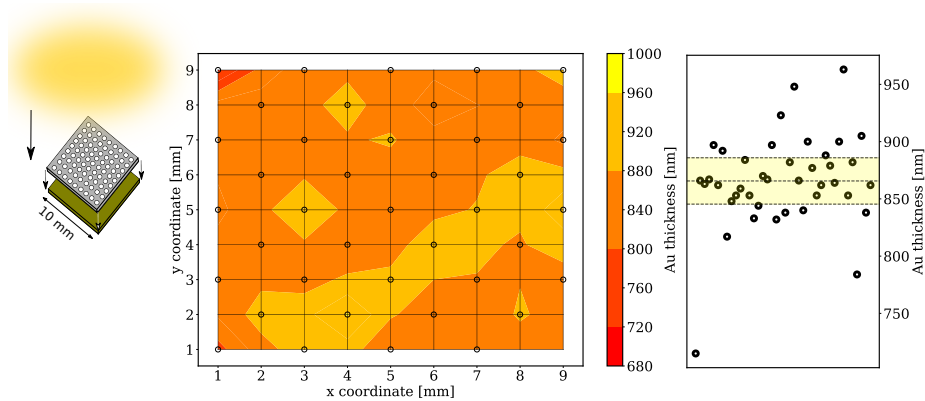


FIGURE 3.20: Thickness profile of the gold deposited on the dummy Si slab.

Following the uniformity test, the deposition procedure was tested on Holmes-like arrays. The $7\ \mu\text{m}$ thick photoresist mask was successfully removed by a lift-off procedure, dipping the array in acetone ($40\ ^\circ\text{C}$) for 24 hours. At this point, the gold deposited remains only on the absorber, which were inspected with a high resolution optical microscope. The crowning at the border was minimal, a sign that the symmetrical positions of the 4 COMIC sources produce a nearly perpendicular ‘beam’ of sputtered gold over the array.

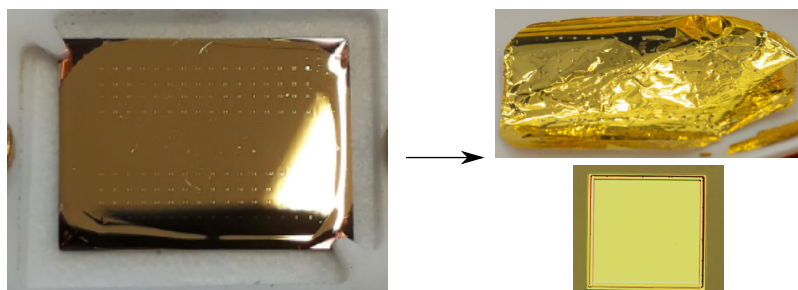


FIGURE 3.21: *Left*: The chip array after the sputtering process, with the gold deposited both on the photoresist mask and on the absorbers. *Right top*: the thin layer of gold removed after the lift-off. *Right bottom*: Zoom on a dummy detector-like absorber used for testing the entire procedure. No crowning was present.

3.4.2 Si etching with KOH

The most suited technique for the membrane release is the Deep Reactive Ion Etching (DRIE), because it etches the Silicon wafer in the $\langle 100 \rangle$ direction producing vertical walls. This allows the detectors to be closely packed in the array, increasing the ^{163}Ho implantation efficiency. However, this technique requires specialized machinery that is not available in our laboratories. At the time of this thesis the DRIE etching is currently under an optimization phase in an external facility (Trustech).

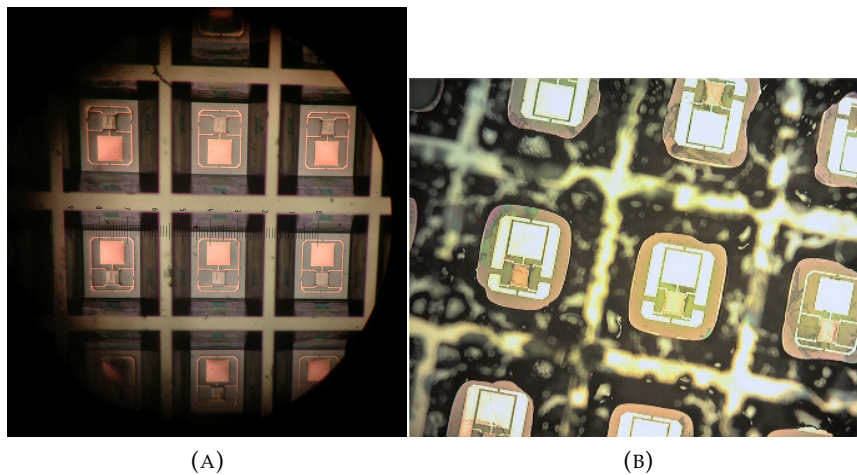


FIGURE 3.22: (A) Back of the detector chip after the KOH etching, where the typical trapezoidal profile can be seen. The etched areas are uniform and smooth between the detectors. (B) Back of the detector chip after the DRIE etching at Trustech. This was a preliminary run, and the etched areas are strongly inhomogeneous and unfinished. Further optimization runs are required to reach the same level of quality and reliability of the KOH.

At the same time, in Milano we tested an alternative technique for the membrane release: the KOH silicon etching. It is a process widely used in microfabrication which uses a water solution of potassium hydroxide to etch the silicon with a rate in the $\langle 100 \rangle$ direction hundreds of times greater than the $\langle 111 \rangle$. Given the results and reliability of the KOH process, this will be Holmes' baseline in case the DRIE process will not be finalized properly.



FIGURE 3.23: Teflon detector holder used for the KOH etching. The detector chip back after the etching procedure can be seen.

A new detector array was thus designed to set the detectors further apart to accommodate the expected trapezoidal hole from the etching procedure, with a larger SiO mask under the silicon wafer. A Teflon holder (Figure 3.23) was produced to expose the silicon wafer to the solution while securing with rubber O-ring the detector top-side of the array. A small hole was drilled on top of the holder, to allow a gentle cooling of the chip during

the etching and to avoid sudden pressure variations due to the fluctuations of the sample temperature.

The solution was made by dissolving KOH pellets in de-ionized water (33% concentration by weight), mixing the solution with a magnetic stirrer and then adding isopropyl alcohol (IPA). It has been shown that even if IPA plays no active part in the chemical reaction, it has the effect of reducing the etching rate on the $\langle 110 \rangle$ plane, increasing at the same time the smoothness of the $\langle 100 \rangle$ surface.

The solution and the Teflon holder were put in a beaker (Figure 3.24) and warmed to 60-70 degree °C on a hot plate. The temperature was kept below the boiling point to avoid that the turbulent motion in the solution may damage the thin SiN membrane. In this temperature range, the silicon etch rate was $\simeq 40 - 45 \mu\text{m/h}$, consistent with the expected one, between 25 and $50 \mu\text{m/h}$.

The extension of the etched area and its quality were randomly checked on different detectors with a microscope (Figure 3.22 (A)), showing good uniformity and quality.

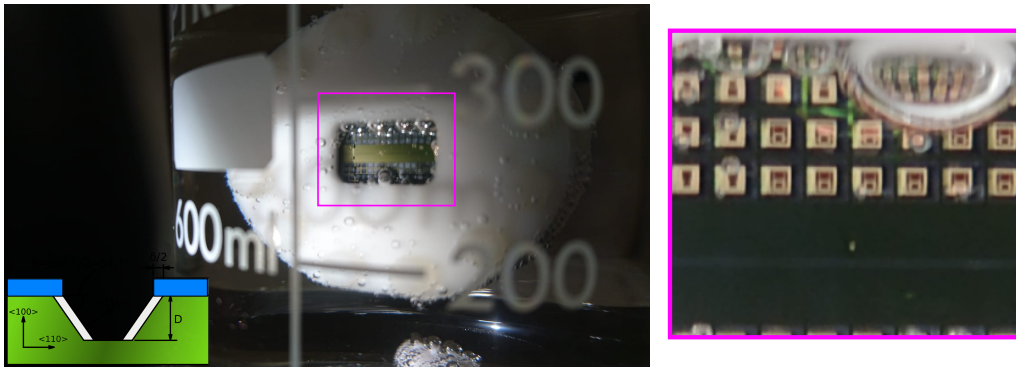
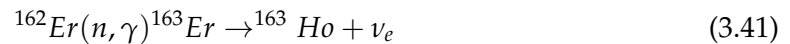


FIGURE 3.24: Picture of the array during the KOH etching process. The hydrogen bubbles can be seen coming off the surface and the detectors begins to be seen on the back (the Si_2N_3 membrane is transparent), a sign that the etching procedure was close to be complete.

3.4.3 ^{163}Ho production and embedding

Since the ^{163}Ho can not be found in nature, it has to be produced via thermal neutron irradiation. The holmium for Holmes was produced irradiating enriched $^{162}\text{Er}_2\text{O}_3$ powder at the ILL nuclear reactor in Grenoble, France (thermal neutron flux $\sim 1.3 \times 10^{15} \text{ n/s/cm}^2$



with the decay $^{163}\text{Er} \rightarrow ^{163}\text{Ho} + \nu_e$ being an EC process ($T_{1/2} \sim 75 \text{ min}$). In order to remove any potentially harmful contaminants to Holmes, both the original Er oxide and the resulting Ho oxide have undergone multiple chemical purification processes at the Paul Scherrer Institute (PSI). As a result, a total of approximately 200 MBq of ^{163}Ho is now available and stored in Genova.

To embed the Ho nuclei in the TES absorbers, a custom ion implanter will be used (Figure 3.25). The system is designed to perform a mass separation of the ^{163}Ho from other contaminants.

The sputter ion source in Figure 3.26 (Danfysik Model 921 A) is the most critical component of the implanter.

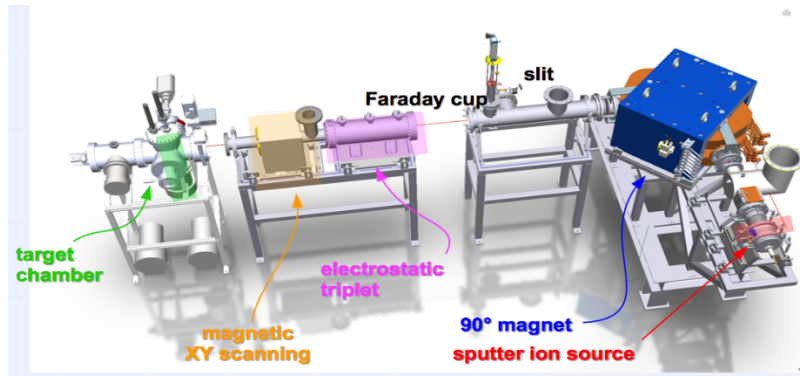


FIGURE 3.25: The HOLMES custom ion implanter.

Its purpose is to create a stable Holmium ion current. To do so, various components are necessary. First, 4 hot tantalum wires emit electrons by thermionic emission. These electrons are accelerated by a “discharge” potential and travel through an argon gas, making multiple collisions with the neutral atoms. At a specific value of argon pressure and electrons kinetic energies, the frequency of these collisions greatly increases and as a result one or more electrons are ripped off the argon atoms, creating an argon plasma. The plasma is accelerated by a sputtering potential towards an electrode disk, upon which a proper target made of Holmium is located.

The argon ions sputter off the target the Holmium atoms and other materials that make up the target. The tension applied to the sputtering electrode must be kept at a few hundred volts to avoid melting the target. At this impact energy the sputtering yield is typically 0.1-1 sputtered particle per ion.

Since the majority of sputtered particles have zero net charge, the Holmium needs to be ionized in order to be accelerated and extracted from the sputter ion source. They thus travel through the plasma, making collisions with the ions and electrons and acquiring a positive charge. The plasma parameters and the voltages must be carefully tuned to reduce the probability that the sputtered Ho atoms hit the colder surface of the chamber, where they would stick before being ionized, reducing the overall extraction efficiency.

Once the Ho atoms are ionized, they are accelerated by an extraction voltage between 30-50 kV (resulting in 1-10 nm of implantation depth), leaving the ion source in an ion beam alongside the argon ions and other contaminants present on the target and on the chamber itself.

After that, the ions pass through a small magnet that can bend the beam along the z axis for alignment before entering the magnetic selector. The latter is a dipole magnet ($B_{max} = 1$ T) that bends the ion beam in order to separate and select the mass of ^{163}Ho from the other contaminants, mainly from the ^{166m}Ho isotope. This isotope is a byproduct of the ^{163}Ho production process, that decays with a low energy beta spectrum ($Q_{\beta^-} = 1854$ keV, $\tau_{1/2} = 1200$ year) that represents a background to the EC spectrum of the ^{163}Ho .

Before finally entering the target chamber, where the detectors array is placed, the beam crosses a tunable slit that cuts the beam tails, further reducing the probability that other contaminants may reach the detectors. Then, it passes through a focusing electrostatic triplet and a magnetic XY scanning which allows the ^{163}Ho beam to hit the desired part of the array.

At the time of this thesis, the electrostatic triplet, the magnetic XY scanning and the target chamber have not yet been installed on the implanter. The latter have finished the commissioning testing in Milano.

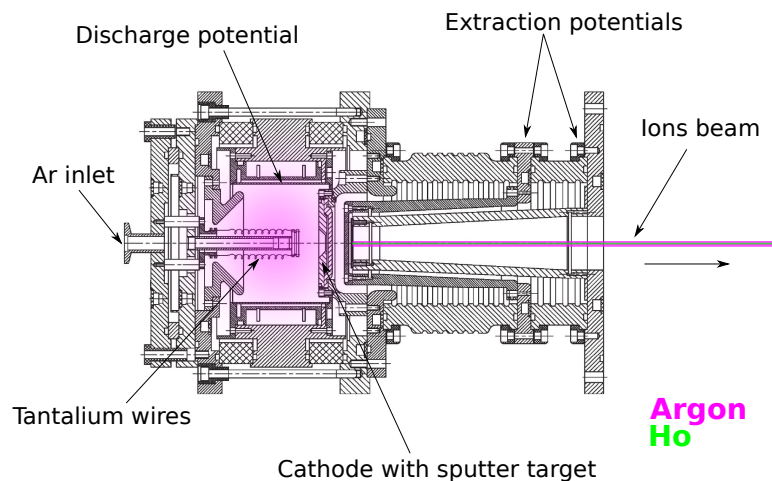


FIGURE 3.26: Scheme of the components of the implanter ion source.

Many efforts were put to install the refrigeration system with de-ionized water, to safely set up the grounding all the various high voltage components and, most important, to optimize the beam parameters.

After that a stable Argon current was achieved, various measurements were made using a faraday cup behind the slit to calibrate the dipole magnet, as shown in Figure 3.27, using sputter target of Cu or Cu/Ti/ Au. The relative abundance of the various isotopes matches the expected one.

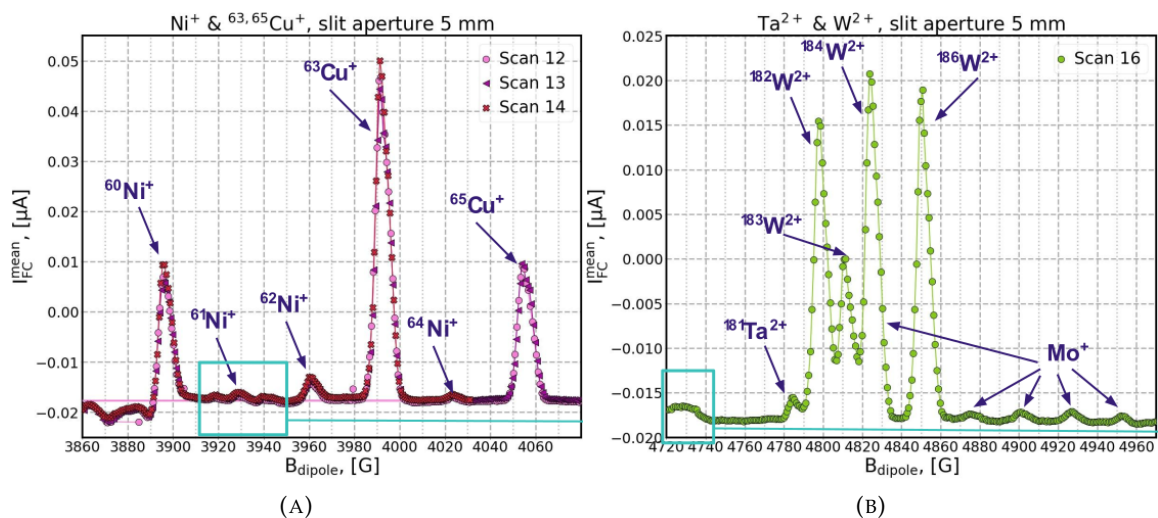


FIGURE 3.27: Example of a dipole scan measurement made during the test with a dummy sputter target.

Currently the experimental efforts are put to build up the most suitable target for the Ho sputtering. The fact that the extraction of the holmium depends on the chemical composition of the target as well as the many parameters of the source makes this task extremely challenging. With the targets tested so far, the natural holmium extracted (^{165}Ho) was way less than what expected and the intensity of the ^{165}Ho seems to rapidly decrease over time.

The most probable hypotheses are related to the high temperature reached by the sputter target inside the sputter ion source. The Holmium atoms located on the surface of the target may have undergone a sublimation process and they might have not being properly ionized inside the source. On the other hand, they could have drifted inside the bulk of the target, reducing the probability of being sputter off by the incoming argon atoms.

Both of these phenomenon are related to the composition of the sputtering target, an element that still has to be correctly identified.

Once the proper target will be defined, a preliminary low dose (≤ 1 Bq) implantation will be made to assess the variation in the detector performance due to the additional holmium heat capacity. The electrostatic triplet and the magnetic XY scanning are not mandatory for the success of this stage.

Chapter 4

Data reduction and signal processing

The analysis of pulses from microcalorimeters designed for X-rays requires great care, because their excellent intrinsic energy resolution can hardly be achieved without an accurate analysis. In this chapter I will present the procedures that I have employed to get from the raw measured data to a "clean" and calibrated energy spectrum.

Because these techniques can be useful to a wider range of applications, the focus of the following chapter will be to present these algorithms in general terms, while their application for the Holmes neutrino mass measurements will be discussed in chapters 5 and 6.

Firstly, it's important to understand how the signals from a TES microcalorimeter are acquired and recorded. Therefore, the first section is devoted to this end while the other sections concern the actual signal processing.

4.1 Data format with microwave multiplexing readout

In a voltage biased TES, a temperature variation of the sensor produces a change in the current flowing through the detector. The small current drop produced by an energy deposition in the absorber (few $\mu\text{A}/\text{keV}$ with the Holmes detectors) is demodulated and amplified thanks to the microwave multiplexing technique. Overall, a microwave tone is assigned to each detector and the value of the detector's current at a time t is translated into a phase shift of its microwave tone at the time t .

The room temperature electronics is responsible to probe every tone associated with a detector, as well to unwrap the frequency shift in order to reconstruct the original current drop and, finally, to record the signal if it meets the trigger conditions.

In the current version of the software, two types of triggers can be used: a derivative trigger and a random trigger. In both cases, a user defined number of samples before and after the trigger is fired, is digitised by a 16-bit analogue to digital convert (ADC) and recorded, alongside the trigger's timestamp.

4.1.1 Data type and dead time

It is possible to categorize the acquired signals into three main classes:

- **Clean events:** records presenting only one pulse rising on a constant baseline. This includes signals of interest but also background events, cross-talks, nearly-coincident pile-up events etc.
- **Multiple events:** records which present two or more distinguishable pulses inside the recorded window, the first of which is rising on a constant baseline.
- **Dirt events:** records with one or more pulses rising on a non-constant baseline due to a previous *multiple event*, to a long tailed *clean event* or due to a trigger malfunction.

At the moment it is not possible to accurately estimate the energy for the last two classes of recorded events, therefore those records are discarded, increasing the dead time of the measurement.

Each recorded window (event) is composed of N samples, divided by N_{base} pre-trigger samples and N_{pulse} after-trigger samples. N_{base} is the number of samples that allows to precisely estimate the baseline value. A larger value of N_{base} will only increase the chance to trigger a *dirt event* and it will also unnecessary increase the disk space. In our current setup, 100 samples are enough.

N_{pulse} is chosen as the number of samples necessary for the signal to fully recovery, that is the time necessary to cool-down the detector after the energy deposition. Up to a certain value, the longer this number will be, the better the optimum filter (see 4.3.1) will perform, i.e. the better the signal's energy will be estimated. Due to the fact that our detector response can be classified as nonparalyzable (the samples of an already recorded signal are not acquired again), N_{pulse} should also be set as low as possible to reduce the chance of triggering *multiple events*, thus a tradeoff must be made between energy resolution and dead time. As a rule of thumb, we set N_{pulse} greater than three times the exponential decay time constant of the signals.

As shown in Table 4.1, The dead time of the Holmes detectors will vary according to the amount of the implanted Holmium and to the detector's response time.

We are currently working in refining the procedures that allow us to tune the detector decay time at the target value of $70 \mu s$, which correspond to a thermal conductance to the heat bath of $\sim 600 \text{ pW/K}$. So far, as explained in section 5.2, the detectors decay time is slower than expected and varies between the different pixels in the array. Therefore, the dead time is reported for the best and worst case scenario.

We are currently studying the performance of a different implementation of the optimum filter based on [73] in order to recover the amplitude of most of the *dirt* and *multiple events*. From our preliminary results, it seems that the decay time can be reduced by at least a factor of two [74].

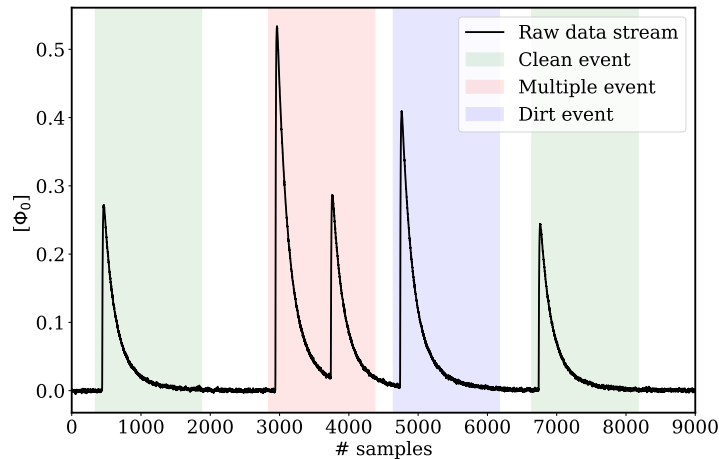


FIGURE 4.1: Simulated raw pulses. Examples for the possible triggered pulses family are presented.

Detector activity [Hz]	N	Detector DT [μ s]	Dead time [%]	$\% \Sigma m_\nu$
1	1024	70	0.2	0.06
	1536	400	0.4	0.2
10	1024	70	2	0.6
	1536	400	4	2
300	1024	70	49	16
	1536	400	72	28

TABLE 4.1: Holmes expected dead time for different detectors time response and activity. $\% \Sigma m_\nu$ is a percentage factor that represents the loss in the neutrino mass sensitivity respect to the zero dead time (the sensitivity scales as $N_{ev}^{-1/4}$, where N_{ev} is the number of recorded events).

4.1.2 Fast signals correction

With the microwave multiplexing readout, the samples of the signals are phase shifts whose values are proportional to the detector's current. All the pulses have the same polarity, so the phase shifts monotonically increases (decreases) during the rise time of the pulse and is decreasing (increasing) during the decay time, depending on the polarity of the bias.

Since it is not possible to distinguish a phase shift of more than π from a negative one of less than $-\pi$, and since the typical pulse will traverse more than 2π , the data must be unwrapped before being stored. If consecutive samples differ by more than π , the unwrapping algorithm subtract 2π and if they differ by less than $-\pi$, it adds 2π .

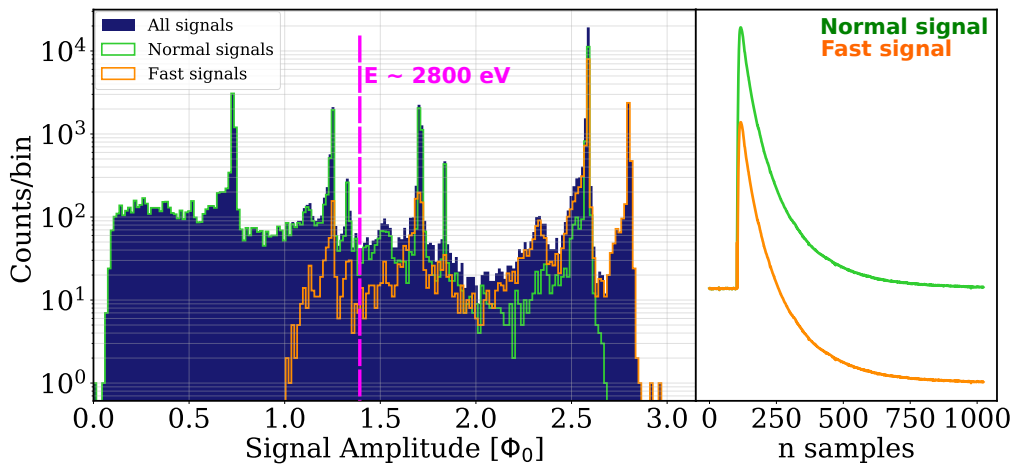


FIGURE 4.2: *Left*: Example of the distribution of the *fast signals* with the variation of the pulse amplitude obtained illuminating the TES with X-rays from an external fluorescence sources (5.1.4). As one can see, the ratio between the number of *fast signals* and normal signals is energy-dependent. *Right*: The normal pulse and the *fast signal* time profile is shown.

However, if the current slew rate during a pulse produces phase shift between samples that are $> 2\pi$, the unwrapping algorithm will fail [75]. This produces what we call a *fast signal*, whose probability of happening depends on the detectors and readout properties,

on the time difference between the actual energy deposition and the first recorded sample and on the energy of the events.

The latter is the most critical: discarding those events will not only increase the dead time, but it will also distort the energy spectrum, introducing a systematic error in the measurement. Therefore, the correction of *fast signals* is mandatory.

The first step is to identify those events, which is easily done by looking at the last samples of the window: these samples for a *fast signal* will differ for about an integer number¹ respect to the pretrigger samples. Secondly, the derivative of the *fast signals* is evaluated, from which the erroneous sample, i.e. the sample for which the unwrapping failed, is identified and its value is increased by the integer value evaluated before. Finally, the true signal shape is obtained by the cumulative sum of the corrected derivative. All these operations are fast and they are executed before the first level data reduction is applied.

4.2 First level data reduction

I will refer to data reduction as those classes of algorithms that identify and remove as many undesirable events as possible from a given dataset. Some of these have already been presented in section 4.1.1, and were labeled as *dirt events* and *multiple events*. The remaining spurious events are categorized as *clean*, and include all those pulses which are not the signals of interest.

I have divided the data reduction algorithms into two levels, depending on the complexity of the algorithm involved. The first level data reduction is composed by offline filters which require a small amount of input information and use low computational power. In addition to *dirt events* and *multiple events*, these filters are used to identify the so called *empty events* and *strange events*. The first ones are noise samples that are acquired using the random trigger and they are used to evaluate the noise spectrum of the detector.

Strange events, on the other hand, describe a wider category of pulses, which also includes events that are not caused by an energy deposition in the detector's absorbers but are related to the readout chains, such as cross-talk signals.

4.2.1 Evaluation of pulse information

Each record is processed in order to extract a few initial quantities that provide useful information about the pulses. While there are several parameters that can be evaluated from each acquired pulse, in this section the straightforward ones are presented, which are the input quantities to the first level data reduction filters.

- **The baseline** [\bar{B} , σ_B , B_{Mm}]. The pretrigger samples carry information about the detector's physical state before the energy deposition. This information can be used to remove *dirt events* as well as to correct the gain drift of the detector. There are three quantities related to the pretrigger samples: their mean (\bar{B}), their standard deviation (σ_B) and the difference between the highest and the lowest value of the samples (B_{Mm}).
- **The raw pulse amplitude** [A_{Mm} , A_{MC}]. The pulse amplitude is the most critical information that has to be extracted because it is strongly correlated with the energy of the event. There are others estimator of the deposited energy [76], but the amplitude is by far the most used one. As a first approximation, it can be evaluated in two ways: as the peak-to-peak amplitude (A_{Mm}) and as the difference between the pulse

¹A phase difference of 2π is equal to one readout unit, or Φ_0 , with our setup

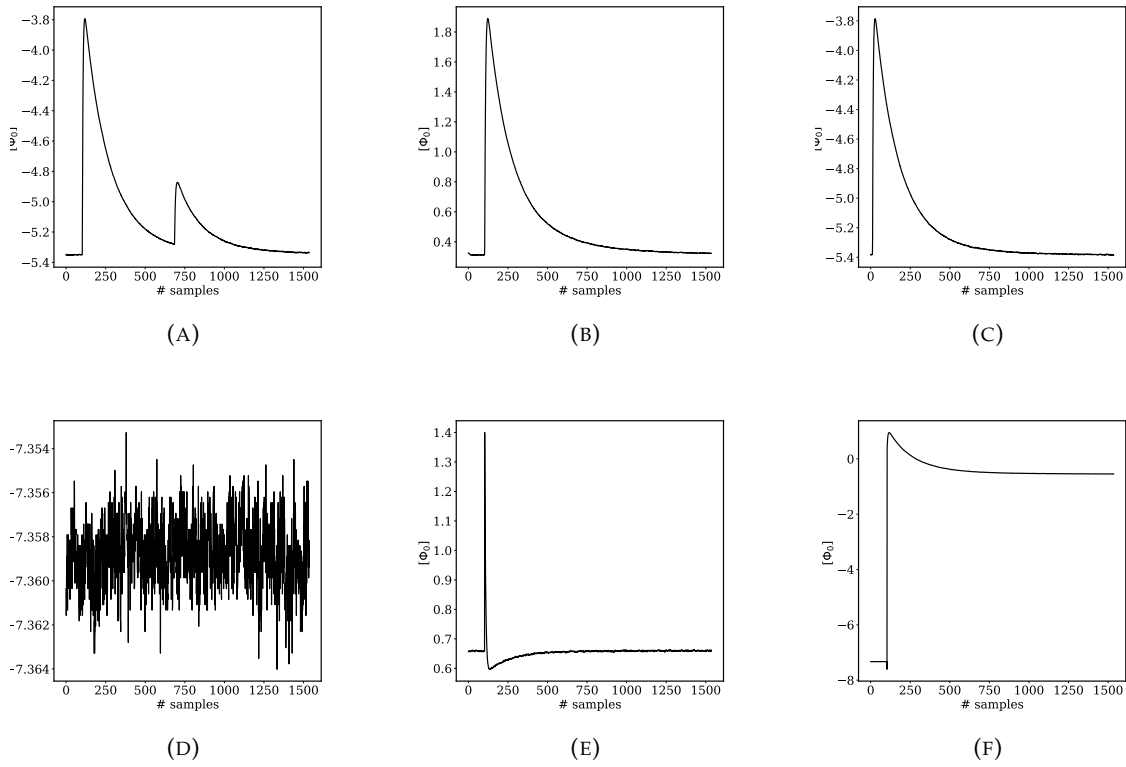


FIGURE 4.3: Examples of various type of spurious events: (A) *multiple event* (B, C) *dirt events*, (D) *empty event*, (E, F) *strange events*.

maximum and \bar{B} (A_{MC}). It is important to emphasise that these quantities are not the ones which are used for calibration; for that goal, a most precise estimation of the pulse amplitude has to be performed (see 4.3.1).

- **The pulse rise time and decay time [RT, DT].** The rise time (RT) of the pulse is defined as the time between the 10% and the 90% of the pulse height while the decay time (DT) is the time interval between the 90% and the 30% of the falling edge of the pulse. The exact positions of those points are obtained with a linear interpolation of the recorded samples. Although RT and DT are subjected to noise, they can still carry a lot of information about the nature of the energy deposition. Signals due to natural radioactivity or cosmic muons interacting with the detector's substrate (see section 6.1.5) as well as pile-up events shows a different detector's time response, thus their pulses exhibit a different shape compare to the single bulk interactions.

4.2.2 Filters for event tagging

The first level data reduction is made of 6 filters that assign a tag to each event of the dataset. Those tag filters only require few input parameters and a threshold value. As the thresholds depend on the detectors' characteristics and working conditions, in principle each detector should have its unique set of values. However, I have observed that even if the detectors behave quite differently, the threshold value for each filter is basically the same for all the detectors, which means that it is possible to tune the thresholds for one pixel and then apply the same values to the whole array.

Empty filter

The aim of the empty filter is to tag the recorded windows containing no events. The events tagged by this filter are used to evaluate the noise spectrum of the detector, which is needed both for the optimum filter and to evaluate the Noise Equivalent Power (NEP) and the expected detector energy resolution. It tags as empty events the ones that fulfill the following condition:

$$A_{Mm} < thr_{empty} \times \min\{\sigma_B\} \quad (4.1)$$

with $\min\{\sigma_B\}$ the minimum value of the σ_B in the dataset.

With the goal activity per pixel of Holmes of 300 Bq and the expected length of the recorded window, less than 50% of the random trigger events is expected to be without a signal. Keeping the fraction of false positive events as low as possible is crucial to achieve the best performance with the optimum filter.

Strange filter

The strange filter tags those events whose shape is substantially different from the one expected by a single energy deposition in the absorber. To be tagged by this filter the events have to satisfy:

$$|A_{Mm} - A_{MC}| \geq thr_{strange} \quad (4.2)$$

For a signal of interest this difference is expected to be close to zero, while for cross-talk, fast signals and events for which the trigger fails to recognize the pulse start it should be greater.

Baseline filter

The baseline filter tags mainly the *dirt events*, i.e. signals which are rising on the tail of a previous pulse. For these pulses it is difficult to link their amplitude to the deposited energy. Due to the detector non-linearity, the same energy deposition will produce different amplitudes depending on the time distance from the previous pulse. If not correctly identified, they will produce a distortion in the energy spectrum that will degrade the experimental sensitivity. The baseline filter requirement is:

$$\sigma_B \geq thr_{bsl} \times \min\{\sigma_B\} \quad (4.3)$$

Multiple event filter

With the adopted version of the optimum filter, it is not possible to estimate the amplitudes of two or more pulses in the same triggered window. The multiple event filter is a derivative filter that recognizes the pile-up events on the tail of the first triggered signal. Its implementation is done in three steps:

1. The data are smoothed with a moving average of order k . This means that the i -th sample of the signal $s[i]$ is re-defined as

$$s_{MA}[i] = \frac{s[i] + s[i-1] + \dots + s[i-(k-1)]}{k} = \frac{1}{k} \sum_{j=0}^{k-1} s[i-j] \quad (4.4)$$

This acts as a low pass filter, reducing the odds that noise peaks will be mistaken for a second pulse peak in step 3.

2. The derivative of the data is evaluated.

3. The events that present one or more samples above a certain threshold thr_{mult} are tagged as multiple events. The first samples after the pretrigger are not considered (the ones on the rise-edge of the pulse).

Note that the pile-up on the tail can also be identified by their larger value of DT and by the second level data reduction algorithms.

Coincidence filter

Cosmic muons or natural radioactivity interacting with the detector surrounding can heat multiple thermometers at the same time. This pulses can be identified by looking at the events timestamp t in all channels and removing the nearly coincidence ones.

$$\Delta t \leq thr_{coin} \quad (4.5)$$

Good filter

The events that are not identified by the previous filters are tagged as *good events*. Those are the ones which will be used in the next steps of the analysis routines.

4.3 Energy estimation

The energy associated with a pulse is the most important parameter to extract. Pulse-height estimation is initially devoided of information about the absolute energy and the complex physics of the TES prevents the computation of the absolute calibration of the detector based on fundamental device properties.

As a result, the most common procedure is firstly to measure the signal amplitude, then to correct this value, taking into account the fact that the detector's gain can change during the measurement. Finally, the amplitude is converted into energy with a calibration function extracted from known energy peaks in the measured spectrum.

This procedure may seem trivial at first glance, but several precautions must be taken to not spoil the result. For instance, the precise pulse height estimation is based on the assumption that the signals produced at different energies present a common shape at all energies.

The TES thermometer is a sensitive but non-linear device, and its nonlinearity results in a slightly different signal's shape for different energies, even far from detector saturation and this in turn worsens the effective energy resolution achieved with the optimum filter technique. To reduce this effect, usually the "common" signal shape is extracted from an energy interval as close as possible to the energy region of interest.

There are other methods used to extract the pulse's energy which can be less sensitive to the detector nonlinearity, such as [76].

4.3.1 Optimum filter

The optimum filter technique was first developed by Gatti and Manfredi [77] for solid-state detectors in 1985. It's a filter which guarantees the best signal to noise ratio under certain assumption, acting on the frequency components of the signal and suppressing those frequencies where the noise contribution is more significant.

Today, there are several different implementation of this filter, ranging from the use of the noise autocorrelation function to the use of the Discrete Fourier Transform (DFT). Holmes use the latter.

The filter assumptions are:

1. Each record s can be seen as $s[i] = K \times m[i] + n[i]$. K is a constant proportional to the energy of the event, m is called the average pulse and it represents the common shape of the pulses while n is the noise.
2. The noise n is ergodic with a power spectral density of \mathcal{N} .
3. s is long enough and is sampled at sufficient speed to contain all the relevant frequency components of m .

Let's assume that \mathcal{H} is the a priori unknown optimal filter of length N that lead to the best S/N ratio, with $\mathcal{H}[i] \in \mathbb{C}$. Calling \mathcal{S} and \mathcal{M} the DFT of s and m respectively, the output of the filter $s_{OF}[i]$ is

$$s_{OF}[i] = IDFT\left(\mathcal{H} \circ \mathcal{S}\right)[i] \quad (4.6)$$

where $IDTF$ is the inverse fourier transform and \circ denotes the element-wise product. The RMS noise at the output is

$$RMS = \sqrt{\sum_i^N (\mathcal{N} \circ |\mathcal{H}|^2)[i]} \quad (4.7)$$

Now, after defining Q^2 as the square of the signal to noise ratio (S/N) at i_{max} , which is position of the maximum in the vector s_{OF}

$$Q^2 \equiv \frac{\left(s_{OF}[i_{max}]\right)^2}{RMS^2} \quad (4.8)$$

we can define \mathcal{H} as the filter which maximize the Q^2 . Applying the Schwartz inequality to 4.8, the filter is equal to

$$\mathcal{H}[i] = C \times \frac{\mathcal{M}[i]^*}{\mathcal{N}[i]} \quad (4.9)$$

with C a normalization factor. We set C such that the amplitude² of $m_{OF}[i] = IDFT\left(\mathcal{H} \circ DFT(m)\right)[i]$ is the same of m .

The measure of \mathcal{N} is trivial: the noise power spectral density is evaluated as the average of the absolute value of the events' fourier transforms tagged by the *empty filter*.

The average pulse m is more complicate to evaluate. First of all, we select an ensemble of 'clean' single pulse records³ with similar value of RT , DT and A_{MC} . Each pulse starts at a slightly different time; therefore, before averaging the pulses sample by sample, each of them have to be shifted by a time Δt to correct this effect.

Taking the first pulse of the ensemble as an approximation of the average pulse m , a preliminary optimal filter will be applied just to evaluate the time when each pulse reaches its maximum. Once one of these times is taken as a reference, Δt will be calculated, each pulse will be corrected by a linear interpolation and finally the right average pulse can be evaluated.

With s_{OF} , the amplitude can be measured both in time domain and in frequency domain. I indicate those values as A_{OFT} and A_{OFF} respectively. A_{OFT} is evaluated considering the maximum point of the parabola that intersect $s_{OF}[i_{max}]$, $s_{OF}[i_{max} - 1]$ and $s_{OF}[i_{max} + 1]$. I

²Evaluated like A_{OFT} .

³The ones tagged with the *good filter*.

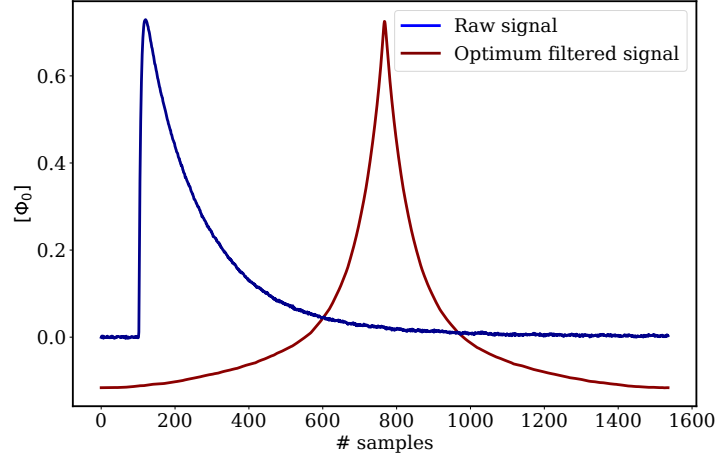


FIGURE 4.4: Example of a signal before (blue) and after (red) the optimum filter.

also extract the information on the position of the parabola maximum, because it is related to the true arrival time of the energy deposition. I call this value OF_{delay} . A_{OFF} is calculated as

$$A_{OFF} = \frac{1}{N} \sum_{i=1}^N |DFT(s_{OF})[i]| \quad (4.10)$$

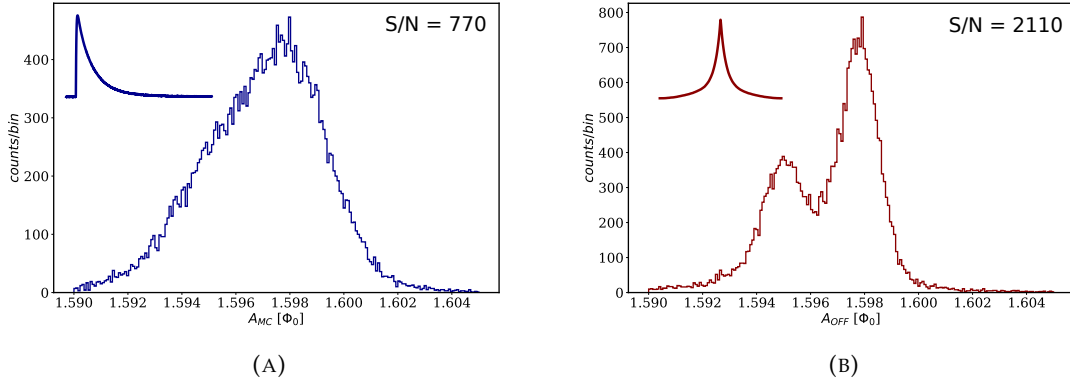


FIGURE 4.5: Comparison between the pulse height distribution for the Mn K_{α} line before (A) and after (B) the Optimum Filter.

4.3.2 Arrival time correction

The evaluation of the pulse amplitude carries a systematic and undersided dependence of the timing of the event t_{true} relative to the sampling time. The value of the first sample on the rising edge of the pulse depends on $\Delta t = t_{true} - t_0^{samp}$, with t_0^{samp} the time of the first recorded sample on the rising edge of the pulse.

The longer the Δt , the higher the sample will be. Hence, as shown in Figure 4.6, the frequency components of the signal will be modified and the optimum filter amplitude will depend on Δt . This unwanted correlation is related to the sample frequency, the higher the

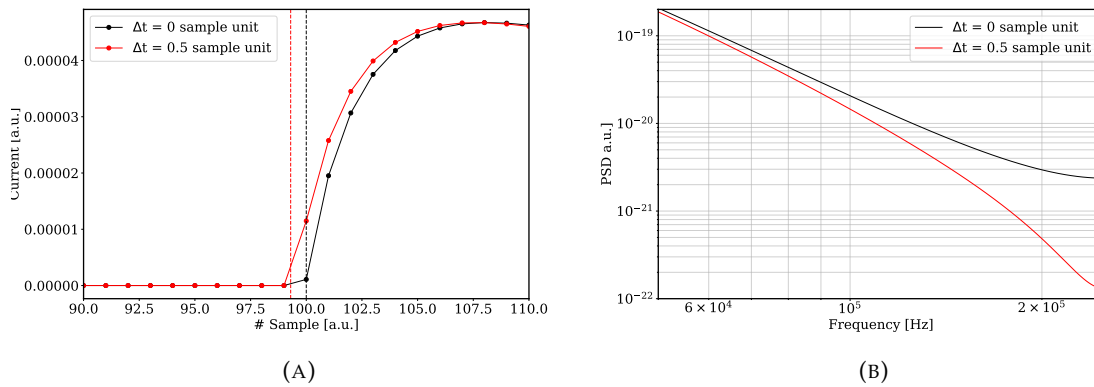


FIGURE 4.6: (A) The rising edge samples of two simulated pulses with the same parameters but with $\Delta t = 0$ and with $\Delta t = 0.5$ sample units. The dotted lines represent the exact arrival time of the events. (B) The Power spectral density of the two pulses of figure (A), with slightly different frequency components. The magnification was made in the higher frequency part of the spectrum to appreciate the effect.

frequency, the lower the effect, to the number of samples on the rising edge (the higher, the lower the effect) and to the signal height (the lower, the less severe this correlation will be).

One of the best way to reduce the bias is through a smoothing of the signals with a simple moving average, i.e. removing the highest frequencies components from the samples.

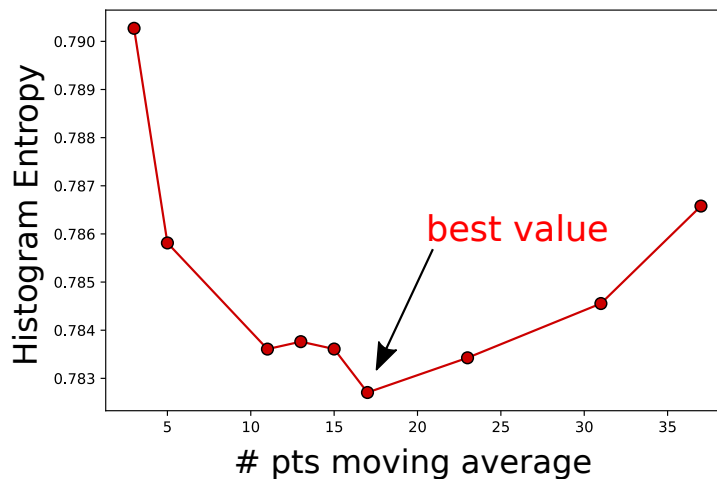


FIGURE 4.7: The spectrum entropy is evaluated on a sample containing events from the Mn K_{α} line, varying the size k of the moving average on the signals. At $k \sim 17$ the entropy reaches a minimum, i.e. the spectral features become sharper, resulting in a higher energy resolution.

First of all, I have to figure out if the bias is present at all and what is the size k of the points to average. Then, I select an ensemble of events in an energy region, preferably of high energy for which the effect is more severe, in which a peak is present. Then, those events are smoothed several times. At each iteration, the size k of the moving average is changed,

the average pulse and the optimum filter amplitudes are calculated on the ensemble and the entropy I of the amplitude spectrum is computed

$$I = - \sum_i^{nbin} c_i \times \log_2(c_i) \quad (4.11)$$

where $nbin$ is an arbitrary number of bins and c_i is the normalized bin entry. If the arrival time bias is present, the peak should become sharper with a particular value of k and then flatten out above this value. Thus, we will expect a minimum in the plot of the points (k, I) . If this is the case, than k is chosen as a value around those minimum and the moving average is apply to the all dataset. Otherwise, the bias is negligible and it is best not to apply any smoothing to the dataset.

If the detectors in the array behave in the same way, this procedure has to be tuned only for one detector, using the k value found on the whole array. Even if k is not the exact minimum for a particular pixel, I have found that it still allow to achieve an improvement in energy resolution for that detector.

The arrival time bias was strongly present with “old” drie-fabricated array setup (*holmes-DRIE*, see section 5.1), while the new chip setup has resulted in longer detectors’ RT with this bias negligible or not present at all.

4.3.3 Gain drift correction

Due to the oscillation of the bath temperature and/or the voltage bias, the detector gain is not stable during the measurement time. This results in signals, caused by the same energy deposition, displaying a time-varying amplitude that will introduce a distortion in the final energy spectrum.

This *amplitude drift* can be fixed by removing the dependence of the signal amplitude on the baseline \bar{B} . Usually, this is done by selecting an ensemble of events inside a monoenergetic peak, fitting the distribution of (\bar{B}, A_{OF}) with $f(\bar{B}) = a \times \bar{B} + b$ and defining a new pulse amplitude A'_{OF} as

$$A'_{OF} = A_{OF} - f(\bar{B}) \quad (4.12)$$

If the robust linear regression used to fit the data describes well their distribution, A'_{OF} should be stable over time.

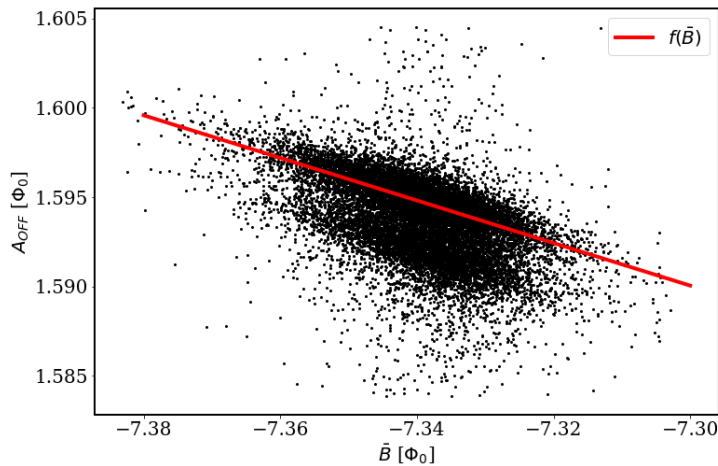


FIGURE 4.8: Example of the distribution of (\bar{B}, A_{OF}) for the Mn K_α line

However, this procedure is much more complicated in practice. First of all, not all the events in the selected ensemble will be distributed with the same slope. Different slopes correspond to different time intervals, as shown in figure 4.9. The origin of this phenomenon is still under investigation. It was possible to observe that these time intervals are not synchronized for each detector of the array, and their appearance seems to depend on the detector features such as geometry, idle current, temperature etc.

Even if during this time intervals the baseline \bar{B} do not usually show any discrete jump over time, it is possible that the different slopes can be related in some way to the existence of phase slip lines (PSL) in the TES thermometer. As explained in chapter 3.1.2, the PSL makes the shape of $R_{TES}(I, T)$ nontrivial, maybe changing its monotonic behavior depending on the idle TES resistance, current and temperature.

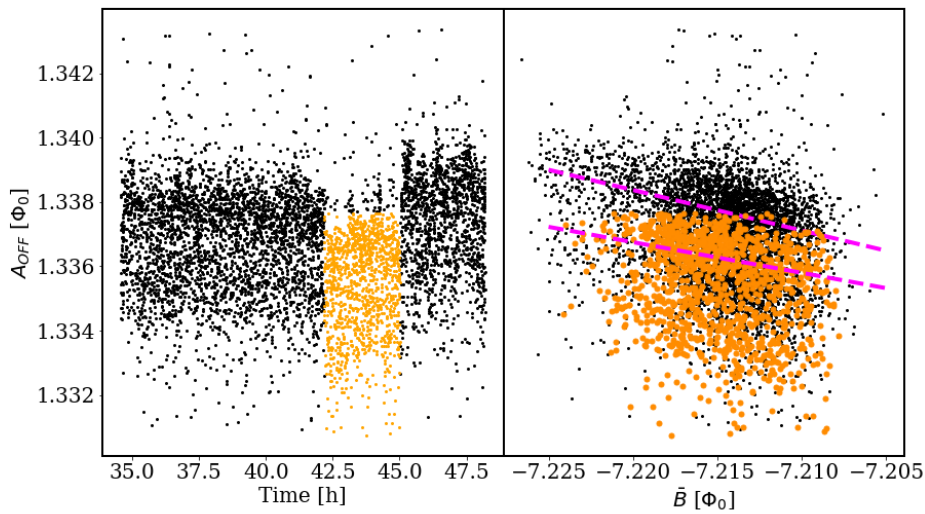


FIGURE 4.9: *Left:* The amplitude drift is shown. *Right:* the distribution of (\bar{B}, A_{OF}) on the same dataset is shown. The point in orange have a different slope (dotted pink line) respect to the baseline, and they have to be removed in order to correct the amplitude drift on the dataset.

Putting aside their nature, remove the events from these time intervals from the dataset before selecting the ensemble and evaluating $f(\bar{B})$ seems to be the best solution.

A further complication is that the slope of the function depends also on the signal energy

$$f(\bar{B}) \rightarrow f(\bar{B}, E) = a(E) \times \bar{B} + b(E) \quad (4.13)$$

This is not an issue when the TESs are used as X-ray microcalorimeters, because in those cases one is usually interested in measuring different energy peaks, thus the amplitude of the events in each peak can be corrected separately. Instead, the Holmes region of interest is a continuous, and using $f(\bar{B})$ evaluated at the nearest energy peak (the M1 peak) could not fix completely the gain drift, leaving unwanted spectrum distortion in the ROI.

For this reason, I developed a technique to correct the gain drift in the whole energy spectrum at once. The idea is to divide the energy spectrum into different small regions for which $a(E)$ and $b(E)$ can be considered almost constants. Then to correct the amplitude of the events in each region with the corresponding value of $f(\bar{B}, E)$. I will assume that $a(E)$ (and $b(E)$) in each energy region can be approximated with

$$a(E) \simeq a(\langle A_{OF}(t_0) \rangle) \quad (4.14)$$

where $\langle A_{OF}(t_0) \rangle$ is the mean of the first amplitudes in that energy interval. The problem thus becomes to find the function which approximate best $a(\langle A_{OF}(t_0) \rangle)$ and $b(\langle A_{OF}(t_0) \rangle)$, using the peaks present in the spectrum as a reference. If the peaks are spread over the spectrum, a spline of degree one should be the most suitable function.

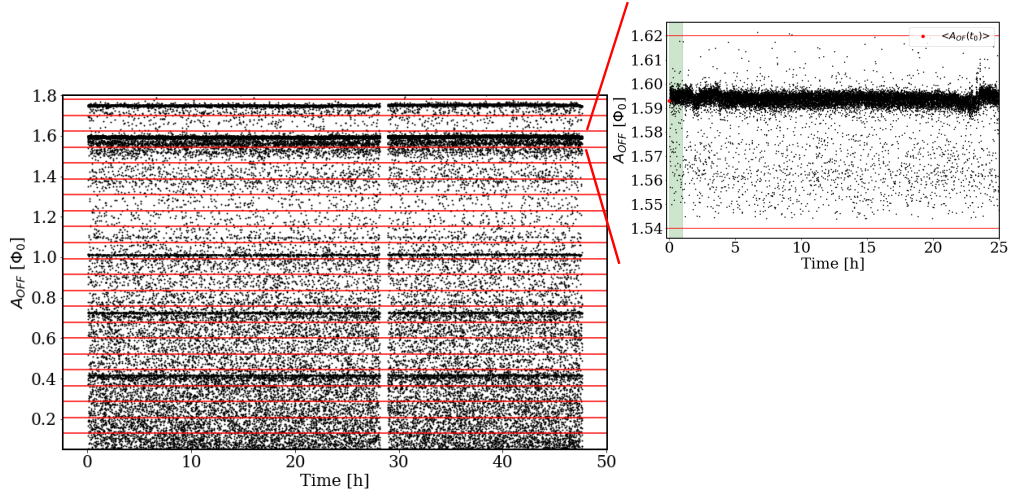


FIGURE 4.10: Example of the gain drift correction procedure. The black points are the amplitude of the measured signals. The red line mark the energy intervals the dataset has been divided, while the green area (top right plot) indicate the region in which $\langle A_{OF}(t_0) \rangle$ (the red dot) is evaluated in that energy interval. Some of the signals (around $\sim 28h$) are missing because they present a different slope in the (\bar{B}, A_{OF})

In summary, the steps for the gain drift correction are the following:

1. Remove the time intervals which present a different slope from the dataset.
2. For each peak, evaluate $\langle A_{OF}(t_0) \rangle$, $a(\langle A_{OF}(t_0) \rangle)$ and $b(\langle A_{OF}(t_0) \rangle)$.
3. Estimate $a(E)$ ($b(E)$) in every other energy interval using a spline of order I and the points from the previous step.
4. Divide the events in the dataset in small amplitude intervals.
5. For each interval, evaluate $\langle A_{OF}(t_0) \rangle$ and correct the amplitude of those events with the expected a and b coefficients.

For Holmes, the idea is to estimate $f(\bar{B}, E)$ during the calibration periods (in which a switchable calibration source will be used, with energy peaks above and below the ROI) and use it to correct the gain drift of the previous “physical” data-taking.

This is for now a manual procedure that has to be done pixel by pixel, with the step 1 taking most time to complete, but it will be made automatic for the multi-array phase of Holmes.

4.3.4 Energy calibration

After that the pulse amplitudes has been precisely evaluated and corrected, it is time to obtain an energy-calibrated spectrum. The goal is to determine one function f_i for each detector such that $E = f_i(A_{OF})$ is the best possible estimate of the energy deposition associated with the signals. The generation of the calibration curve is done in an automatic way.

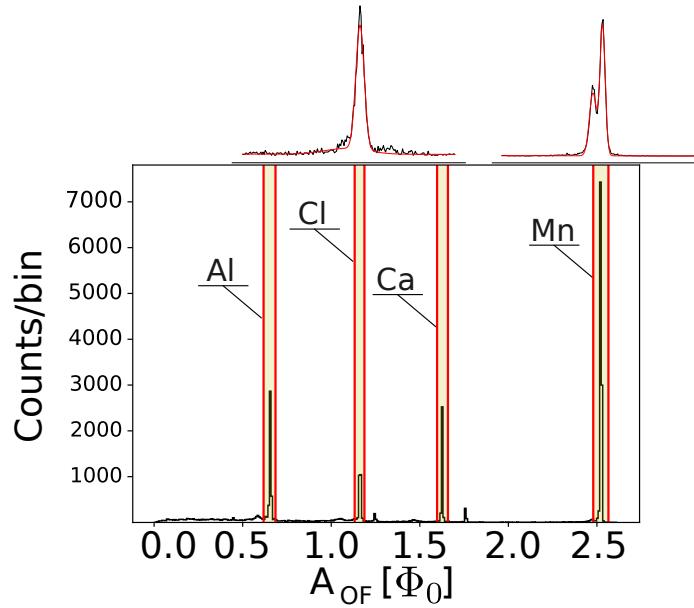


FIGURE 4.11: Example of the calibration procedure with the Holmes X-ray fluorescence sources. The yellow area are the regions in which the peak position is evaluated.

First, the position of each peak in the spectrum is roughly evaluated. If the distance between two peaks is less than a certain value, the higher energy peak is not considered in the following steps. This is done in our current setup to exclude the K_β peaks, for which the position of the maximum is difficult to evaluate. Then a small interval around the peak is selected and a multi-gaussian fit with non-uniform background is performed on the resulting histogram, from which the position of the highest peak is calculated. Assuming to know the energy of the peaks, the calibration points are placed in the $A_{OF} - E$ space, and a fit with a first or second order polynomial curve is performed.

It is important to point out that in the interest of a neutrino mass measurement an extremely precise calibration curve is not necessary because the only strongly calibration-dependent quantity is the Q -value of the decay, but it will be a free parameter of the fit. In addition, the spectrum for each detector will be treated separately in the analysis.

Expected energy resolution

To check if the previous procedures have been correctly carried out, it is possible to compare the energy resolution measured at a known energy peak with the expected one from the noise equivalent power NEP

$$\Delta E_{FWHM} = 2\sqrt{2\ln 2} \left(\int_0^\infty \frac{4}{NEP(f)} df \right)^{-1/2} \quad (4.15)$$

The NEP can be calculated from the detector responsivity $\mathcal{R}(f)$ (or $r(t)$ in time domain) and the noise power spectrum $\mathcal{N}(f)$

$$NEP(f) = \frac{\mathcal{N}(f)}{|\mathcal{R}(f)|^2} \quad (4.16)$$

while the responsivity can be estimated knowing the average signal $m(t)$ and the energy associated with it.

$$m(t) = E \times (\delta(t - t_{start}) * r)(t) \quad (4.17)$$

where $*$ denotes the convolution operation and assuming that the energy deposition time profile can be modeled as a delta function.

Putting all together and taking into the normalization due to the discretization

$$NEP[i] = \mathcal{N}[i] \circ \mathcal{R}[i] = \mathcal{N}[i] \circ \left(\left| \frac{DFT(m[i]) \times t_{sample}}{E} \right|^2 \right)^{-1} \quad (4.18)$$

4.4 Second level data reduction

At this point there are still numerous spurious events which are not recognized by the first level data reduction.

Background events interacting with the detector's surroundings and pile-up events on the rise edge of the pulse are among these. The latter consists of two events of energies E_1 and E_2 which occur within a time interval shorter than the time resolution of the detector, so they are mistaken for a single event with energy $E \simeq E_1 + E_2$. If not correctly identified, pile-up events on the rise time⁴ will distort the decay spectrum of ^{163}Ho , lowering the neutrino mass sensitivity.

Simulations have shown that the Holmes experimental sensitivity strongly depends on the pile-up fraction f_{pp} , i.e. the ratio between the number of pile-up events to single events, thus its reduction is crucial for the success of the experiment (2.3).

These events are extremely difficult to identify, because there are only subtle differences between them and a true signal event. They require advanced discrimination techniques with energy independent efficiency in order to be suited for a neutrino mass measurement.

4.4.1 Optimum Filter shape parameters

Using the same terminology as in [78], from the optimum filter it is possible to compute three different parameters, called the Optimum Filter Test Value Left and Right (TVL and TVR) and the Optimum Filter Test (OFT).

The first two are the root mean square differences between the normalized average pulse $m_{OF}[i]$ and the normalized signal $s_{OF}[i]$ both after the optimum filtering.

$$TVL = \frac{1}{N} \sum_i^N (s_{OF}[i_{max} - i] / s_{OF}[i_{max}] - m_{OF}[i_{max} - i] / m_{OF}[i_{max}])^2 \quad (4.19)$$

$$TVR = \frac{1}{N} \sum_i^N (s_{OF}[i_{max} + i] / s_{OF}[i_{max}] - m_{OF}[i_{max} + i] / m_{OF}[i_{max}])^2 \quad (4.20)$$

where i_{max} is the position of the maximum sample in the vector, and N is an arbitrary number that I usually set as twice the number need to reach half of the signal maximum.

Before applying eq 4.19, 4.20, a synchronization between $m_{OF}[i]$ and $s_{OF}[i]$ is performed using OF_{delay} and a linear interpolation.

If in a dataset there are some spurious events, their shape is expected to be different from the average one, therefore their TVL and TVR are expected to be well above the mean value, as shown in Figure 4.12.

⁴from now on they will be indicated simply as pile-up events

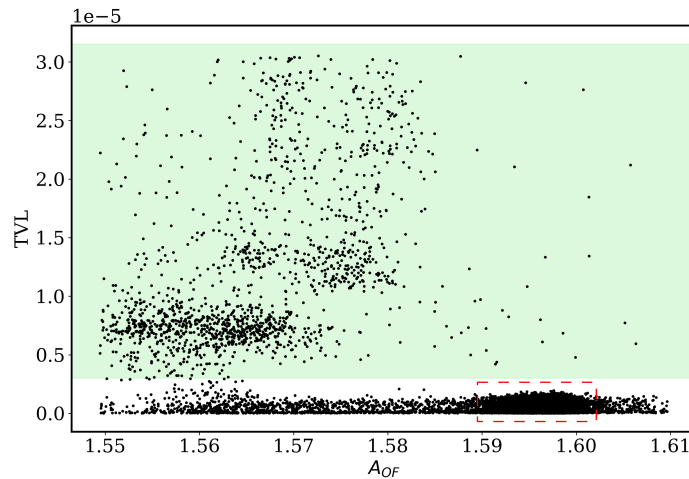


FIGURE 4.12: Example of the distribution of (A_{OF}, TVL) near the Mn K_α line (red dotted square). The signals with a TVL value inside the green area can be removed.

OFT is defined as

$$OFT = 1 - \frac{A_{OFT}}{A_{OFF}} \quad (4.21)$$

In the presence of two pulses in the acquired window, the OFT will be greater than zero roughly because the A_{OFF} performs an estimation on the pulse amplitude using the information from the whole window, while A_{OFT} only on the samples near the maximum.

4.4.2 Wiener Filter and Pile-up discrimination

As already mentioned, each signal s can be seen as the convolution of an input function $p(t)$, representing the time profile of the energy deposition inside the detector, and the detector response function $r(t)$

$$s(t) = r(t) * p(t) + n(t) \quad (4.22)$$

with $n(t)$ representing the noise.

I want to build a filter that recovers the original input function, deconvolving the signal from the response function of the detector and allowing us to recognize pile-up pulses more easily. Respect to the typical time scale of the signal, this input function can be seen as a delta function starting at the pulse time start t_{start} , $p(t) = E \times \delta(t - t_{start})$.

The idea is to find the coefficient $[a_0, \dots, a_N]_i$ of a causal finite impulse response (FIR) Wiener filter [79] of order N which minimize the difference between the filtered signal $s_{WF}[i]$ and the input power function $p[i]$.

Assuming that the discretized signal and the input power function can be seen as

$$s[i] = k \times m[i] + n[i] \quad (4.23)$$

$$p[i] = k' \times \delta_{ii_{start}}[i] \quad (4.24)$$

m is the average signal, $\delta_{ii_{start}}$ is the Kronecker delta and k, k' are constants.

The Wiener filtered signal is written as

$$s_{WF}[i] = \sum_{j=0}^N a_j s[i-j] \quad (4.25)$$

and it is designed as to minimize the mean square residual error $E[e^2[i]]$

$$a_i = \arg \min E[e^2[i]] \quad (4.26)$$

$$e[i] = s_{WF}[i] - p[i] \quad (4.27)$$

In the following I will report briefly some of the passages necessary to evaluate the $[a_0, \dots, a_N]$

$$E[e^2[i]] = E\left[\left(\sum_{j=0}^N a_j s[i-j]\right)^2\right] + E[p^2[i]] - 2E\left[\sum_{j=0}^N a_j s[i-j]p[i]\right] \quad (4.28)$$

To find the a_i which minimizes $E[e^2[i]]$, I calculate its derivative with respect to each a_i

$$\frac{\partial}{\partial a_i} E[e^2[i]] = 2E\left[\left(\sum_{j=0}^N a_j s[i-j]\right)s[i-j]\right] - 2E[s[i-j]p[i]] \quad (4.29)$$

$$= 2\left(\sum_{k=0}^N E[s[i-k]s[i-j]]a_j\right) - 2E[s[i-j]p[j]] \quad (4.30)$$

I assume that $s[i]$ and $p[i]$ are each stationary and jointly stationary and knowing that

$$R_s[j] \equiv E\{s[i]s[i+j]\} \quad (4.31)$$

$$R_{sp}[j] \equiv E\{s[i]p[i+j]\} \quad (4.32)$$

are respectively the autocorrelation of $s[i]$ and the cross-correlation between $s[i]$ and $p[i]$. In practice, to compute R_s and R_{sp} I just need the average signal m and the Kroneker delta

$$R_s[i] = k^2 \times R_m[l] + R_n[i] + k \times R_{mn}[i] \simeq k^2 \times R_m[i] \quad (4.33)$$

$$R_{sp}[i] = k \times R_{mp}[i] + R_{np}[i] \simeq k \times R_{mp}[i] \quad (4.34)$$

eq 4.30 can be rewritten as:

$$\frac{\partial}{\partial a_i} E[e^2[i]] = 2\left(\sum_{j=0}^N R_s[j-l]a_j\right) - 2R_{sp}[l] \rightarrow \sum_{j=0}^N R_s[j-l]a_j = R_{sp}[l] \quad l = 0, \dots, N \quad (4.35)$$

It's easy to solve the above equation in its matrix form

$$\begin{bmatrix} R_s[0] & R_s[1] & \dots & R_s[N] \\ R_s[1] & R_s[0] & \dots & R_s[N-1] \\ \dots & \dots & \dots & \dots \\ R_s[N] & R_s[N-1] & \dots & R_s[0] \end{bmatrix} \begin{bmatrix} a_0 \\ a_1 \\ \dots \\ a_N \end{bmatrix} = \begin{bmatrix} R_{sp}[0] \\ R_{sp}[1] \\ \dots \\ R_{sp}[N] \end{bmatrix} \quad (4.36)$$

Using eq 4.33 and 4.34, the equation becomes

$$k^2 \times \begin{bmatrix} R_m[0] & R_m[1] & \dots & R_m[N] \\ R_m[1] & R_m[0] & \dots & R_m[N-1] \\ \dots & \dots & \dots & \dots \\ R_m[N] & R_m[N-1] & \dots & R_m[0] \end{bmatrix} \begin{bmatrix} a_0 \\ a_1 \\ \dots \\ a_N \end{bmatrix} = kk' \times \begin{bmatrix} R_{s\delta}[0] \\ R_{s\delta}[1] \\ \dots \\ R_{s\delta}[N] \end{bmatrix} \quad (4.37)$$

or

$$\mathbf{T}\mathbf{a} = \frac{k'}{k}\mathbf{v} \quad (4.38)$$

k'/k can be seen as a normalization factor, it doesn't change the shape of the filtered pulse. Therefore, I will set it equal to 1, resulting in

$$\mathbf{a} = \mathbf{T}^{-1}\mathbf{v} \quad (4.39)$$

Thus, the a_i of the wiener filter are given by the product of the inverse of the Toeplitz matrix \mathbf{T} with the vector \mathbf{v} , which in turn are defined only by the average signal and the Kroneker delta.

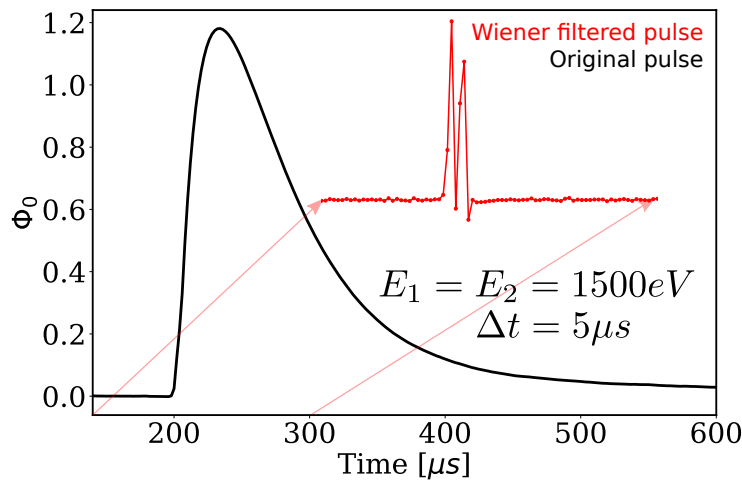


FIGURE 4.13: A simulated pile-up event (black) well identified by the Wiener (red) filter.

As you can see in figure 4.13, if a signal follow eq 4.24 its shape after the Wiener Filter will look like a delta function, while if it is made of two or more pulses, it will look like two or more delta or a single “drooled” delta if the time difference between the energy depositions is close to the signal sampling time.

Wiener filter shape parameters

Now, I need to find a set of suitable parameters which allow me to discriminate between a drooled delta and a proper one. The first parameter that can be defined is called Wiener filter width WF_w and it is defined as the distance between the first and the last point of the filtered signal above a certain threshold thr_{WF} . The exact points' positions x_f and x_l is evaluated by a linear interpolation between the first sampled point above threshold and the previous one. The second parameter is called WF_{pts} and is the integer number of sample of the filtered signal above the thr_{WF} . The last one is the position of the maximum filtered signal, WF_{delay} . Notice that WF_{pts} , WF_w and WF_{delay} do not depend on k'/k .

Due to the fact that the delta-function will be undersampled, WF_{delay} will be calculated using symmetry

$$WF_{delay} = x_f + \left(\frac{x_l - x_f}{2}\right) \quad (4.40)$$

All of these parameters depends on the value of thr_{WF} . I suggest to set thr_{WF} signal by signal

$$thr_{WF} = \lambda \times \sigma_B \quad (4.41)$$

where σ_B is the RMS value of the i -th signal calculated on the pretriggered filtered samples, while λ is a reasonable value which minimize the probability P that the filtered noise ends up above threshold. This is given by

$$P = n \times \left(1 - \frac{\int_{-\lambda\sigma}^{+\lambda\sigma} gaussian(x|0, \sigma) dx}{2}\right) \quad (4.42)$$

n is the length of the window in which the delta function is searched.

We expect that the pile-ups will be distributed outside a dense region made of single events in the WF_w-WF_{pts} and in WF_w-WF_{delay} spaces. A possible strategy to implement this filter in the Holmes experiment will be outlined in section 6.2.3.

4.4.3 DSVP for discrimination of spurious events

The DSVP (Discrimination through Singular Vectors Projections) [80] is a novel technique that I have developed based on a previous work [81] to discriminate spurious events within a dataset. In the following, I will lay down a general procedure which in principle can be tailored for a broad variety of applications, not only to microcalorimeters signals. In fact, one of the main advantage of this method is that it does not rely on any particular assumption about the structure of the recorded events. Therefore the syntax will be kept as vague and abstract as possible. The expected performance of this technique for the Holmes experiment will be shown in section 6.2.2.

The aim of the DSVP algorithm is to discriminate as many as possible undesirable events (i.e. spurious events which differ from a reference signal) present in a given dataset, using the information about the mean 'morphology' of the events present in the dataset. In order to apply the DSVP technique, the following elements are required:

- The measured dataset, \vec{M} . This $n \times d$ matrix consists of the dataset of interest, where each row is an event described by d variables. Namely, the events can be seen as points in the \mathbb{R}^d space. From now on, we call the *good* events in the dataset A events, while B events are the ones to be rejected. We assume that the A events are more numerous respect to the B ones ($N_A > N_B$)⁵.
- The expected number of B events N_B that the algorithm should discard at most.
- A training dataset, \vec{T} , such that $N_A \gg N_B$. The events of this $n' \times d$ matrix can be distributed in a different region of \mathbb{R}^d respect to the events in \vec{M} . For instance, in the case of microcalorimeter signals, the events in \vec{T} can lie in a different energy range respect to the events in \vec{M} .

We will use the training dataset \vec{T} to define a new vector space which will help us to highlight the features that distinguish an A event from a B one. This new vector space, called from now the projections space, has dimension k , with $k \ll d$. The events can

⁵See section 4.4.3

be represented as points in the \mathbb{R}^k projection space, so that the A events are distributed differently respect to the B ones.

The idea is to find a model (i.e. hypersurfaces) describing the distribution of the A points in \vec{M} in this new space, so that the B points can be identified as the ones with a larger distance from what predicted by the model. In order to find the model we need to 'clean' the dataset first, obtaining a subset of \vec{M} , $\vec{M}' \subset \vec{M}$, which contains mostly A events at the expense of deleting also some A events.

The next step is to represent the events in \vec{M}' in the projection space and to find the model parameters which describes the distribution of the \vec{M}' ($\sim A$) events.

We then define the discrimination parameter and its threshold to recognize an A event from a B one in \mathbb{R}^k .

Finally, we take the original dataset \vec{M} , represent the events in the projection space, find the discrimination parameter and discard all the events that have a value of the discrimination parameter above the threshold found.

The procedure (dataset 'cleaning', model and threshold definition and B discrimination) is then repeated with the survived events. At each iteration, the \vec{M} dataset will contain a smaller fraction of B events. In the following sections, each steps of the algorithm are described in detail.

Raw cleaning with PCA

In the first step, the aim is to create a suitable dataset for modeling the distribution of A events in the \vec{M} matrix, lowering the ratio N_B/N_A at the expense of deleting also A events. Knowing that $N_A > N_B$, the mean 'morphology' of the events is closer to the A ones. We can define a suitable parameter using the Principal Component Analysis (PCA) to discard mainly B events. The procedure used is equal to the one described in [81], which will be reported for completeness.

The singular value decomposition (SVD) [?] is computed for the $n \times d$ matrix \vec{M} , which is decomposed in a product of three matrices $\vec{M} = \vec{U}\vec{D}\vec{V}^T$. The columns of \vec{U} and \vec{V} are the left and right singular vectors respectively, while the entries of the diagonal matrix \vec{D} are the singular values. The singular values are ordered from 1 to d in order of importance. Only the first $j < d$ columns of \vec{D} are non-neglibile. It is convenient to define a new matrix $\hat{\vec{U}}$ which contains only the first j columns of \vec{U} subtracted by their means which is equivalent to centering the data matrix, as required by the PCA.

The columns of $\hat{\vec{U}}$ are vectors of length n . Basically, they represent the projections of the mean-centered events contained in \vec{M} on the right singular vectors (i.e. the columns of \vec{V} , which are called principal vectors in the PCA framework) with the first column of $\hat{\vec{U}}$ expressing the projections on the first right singular vector and so on. The columns of \vec{V} are vectors of dimension d which represent the direction of greatest variance of the data in \vec{M} .

Thanks to the properties of the PCA, an appropriate combination of the projections can be of use to define a parameter, called $norm^2$, which indicates how close an event is to the mean 'morphology' of the events in \vec{M} .

The precision matrix $(\sigma^2)^{-1}$ is computed from the $j \times j$ empirical covariance $\sigma^2 = \hat{\vec{U}}^T \hat{\vec{U}}$ and it is used to evaluate the parameter $norm^2$ for each event $i = 1, \dots, n$ in the matrix \vec{M}

$$norm_i^2 = \hat{\vec{U}}_{i,*} (\sigma^2)^{-1} \hat{\vec{U}}_{i,*}^T \quad (4.43)$$

Suppose that we have a guess of how many B events are expected in the dataset. We call this number N_B^{guess} . B events deviate disproportionately from the mean in this covariance-adjusted sense, so we discard those with largest $norm^2$ and repeat the procedure on the remaining data a total of l times, removing on the l -th iteration a number of events equal to $N_B^{guess}/2^l$ with the largest $norm^2$. In our tests, we use $l = 5$.

The iterations guarantee that the mean morphology of the events are closer and closer to the A events each cycle, as B events are increasingly eliminated.

After the PCA, we have eliminated

$$N_{del}^{PCA} = \sum_l \frac{N_B^{guess}}{2^l} \quad (4.44)$$

events, where the B events are the ones predominantly discarded. The remaining events after the PCA are $m = n - N_{del}^{PCA}$. We call \vec{M}' the $m \times d$ the matrix of the survived events, which is mostly composed of A events.

Define a model for the A-events

To discriminate the undesirable events, we now need to define a model which describes the distribution of the A points (the ones belonging to \vec{M}') in the projection space.

First, we need to define this space. We decompose the \vec{T} matrix using the SVD. Because the training matrix \vec{T} is mainly composed by A events, we assume that its first k significant right singular vectors $\{\vec{v}_1, \vec{v}_2, \dots, \vec{v}_k\}$ can constitute a base of the projection space. The events in \vec{M}' are projected onto these vectors.

From now on, each event in \vec{M}' will be described by $k < d$ variables, its projections onto the right singular vector of \vec{T} . We indicate all the coordinates of the \vec{M}' points along the i -th base vector of the projection space as $p_i = \vec{M}' \cdot \vec{v}_i$.

To describe the points distribution in the new vector space, the projections p are classified into two groups: the k' independent projections, indicated as \vec{p}_{ind} and the dependent ones, \vec{p}_{dep} .

$$\{p\}_k = \underbrace{p_1, \dots, p_{k'}}_{\vec{p}_{ind}}, \underbrace{p_{k'+1}, \dots, p_k}_{\vec{p}_{dep}} \quad (4.45)$$

The dependent projections can be expressed as a function of the independent ones. There is no general rule to identify which projection is "independent" and which one is not, since it is related to the specific problem. The training dataset can be used to identify the dependencies among the projections, as shown in Fig 4.14.

The distribution of the dependent projections can now be easily described in a $\mathbb{R}^{k'+1}$ subspace by a set of f curves

$$p_i = f_i(\vec{p}_{ind}) \quad ; \quad i = k' + 1, \dots, k \quad (4.46)$$

Knowing precisely the set of curves $\{f\}$, we will be able to differentiate between the two distribution of events, because the projection of the B events will not follow the same curves as the one of the A events.

Usually the functional form of the different f is unknown. However, we can approximate each f curve with a Taylor expansion and let a (weighted) linear regression find the best

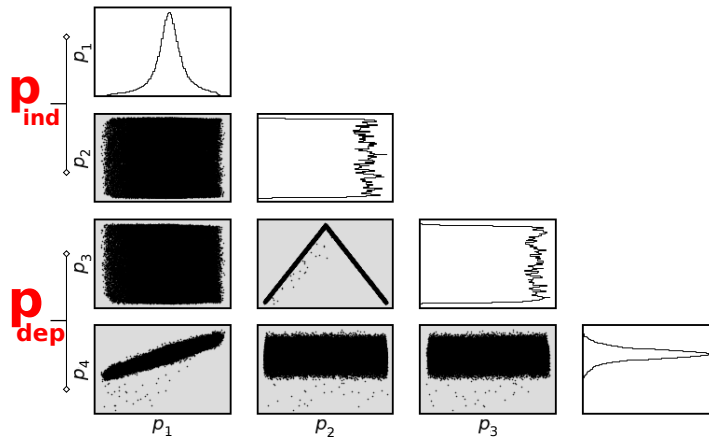


FIGURE 4.14: An example of distribution of the points in \vec{T} in the projection space from sec. 6.2.2. In this particular case, the projection space is in \mathbb{R}^4 . We decided to set $k' = 2$, thus describing the points distribution in \mathbb{R}^4 with two curves: $p_3 = f_3(p_1, p_2)$ and $p_4 = f_4(p_1, p_2)$

parameters of the expansion. In particular, we use a modified version of the random sample consensus (RANSAC) algorithm [?] ⁶. The set of curves $\{f\}$ which describes the \vec{M}' events in the projection space is what we called the model.

Find a discrimination threshold

The difference between the measured dependent projections and the ones expected from the model is evaluated for each event in the \vec{M}' matrix. A residual norm is defined as

$$d = \sqrt{\sum_{j=k'+1}^k (p_j - f_j(\vec{p}_{ind}))^2} \quad (4.47)$$

In order to discriminate between the A events, the one with the lowest residual norm, and the B , we need to define a threshold value, d_{thr} . Due to the fact that the \vec{M}' dataset is mainly made of A events the threshold is chosen as the highest value of d plus the standard deviation of the d distribution

$$d_{thr} = \max\{d\} + \text{std}\{d\} \quad (4.48)$$

This threshold definition should ensure to include not only the A events in \vec{M}' , but also the A events in the original dataset \vec{M} which were eliminated by the 'PCA cleaning' described in 4.4.3. Nevertheless, this definition of threshold might need to be redefined to account for the specific problem considered.

Apply the model

Now all the components to make the algorithm work are present: a base for the projection space, a set of curves to model the points distribution in that space and a discrimination

⁶Due to the fact that the number of outliers (B events) from step 4.4.3 is expected to be negligible, any type of weighted linear regression can in principle be used.

threshold.

We will now use these tools on the original dataset \vec{M} , namely:

1. Take the inner product of the events in \vec{M} with the base of the projection space, determining p_k .
2. Evaluate the residual norm d using the curves describing the A projections distributions.
3. The events with a residual norm above the threshold are discarded.

After the third step, we will have discarded N_{del} events. The events deleted by the third step will be almost, if not all, spurious B events. All the previous steps (PCA, model and threshold definition) are now repeated with a reduced number of expected B events, $N^{B'} = N^B - N_{del}$. The iterations successively improve the representation of A events, as B events are increasingly eliminated. The algorithm stops when $N_{del} = 0$ or when $N^{B'} = 0$.

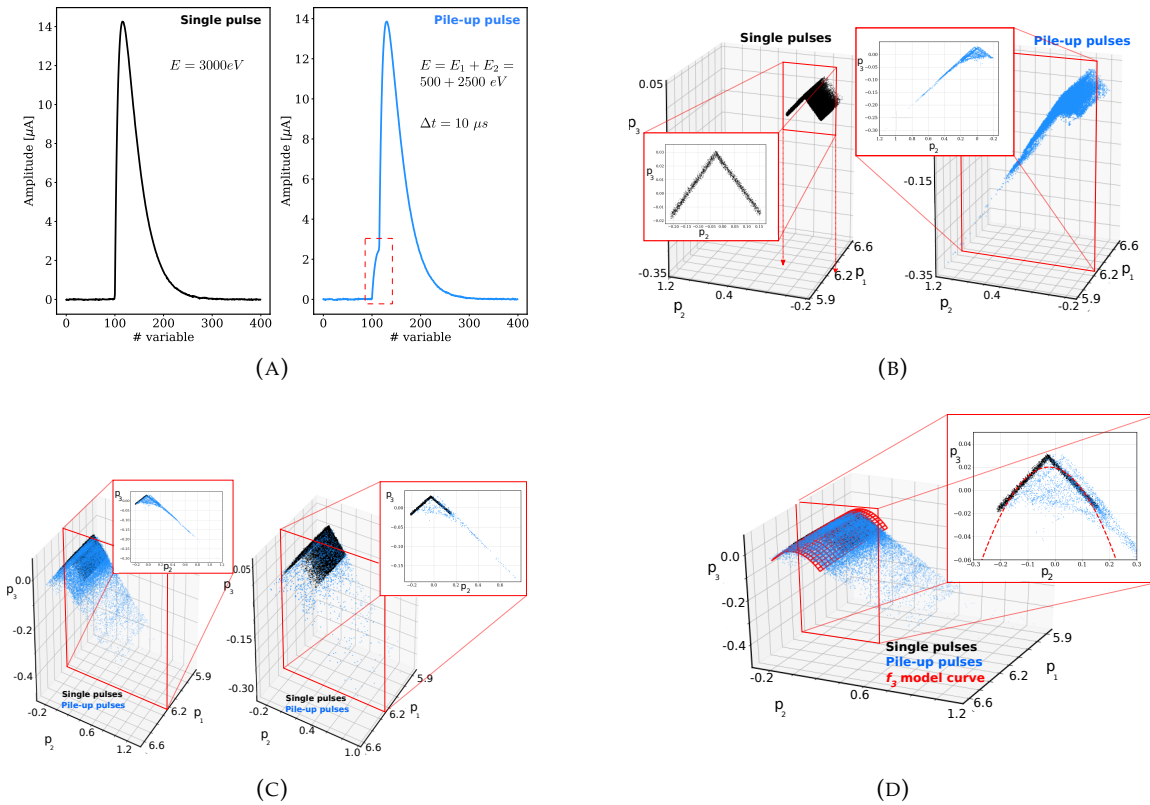


FIGURE 4.15: a) Each event (row) of the matrix \vec{M} is initially described by 400 variables i.e. samples; we can represent each event as shown in figure or as points in \mathbb{R}^{400} . \vec{M} contains two different types of events: single pulses (A) of energy E and pile-up pulses with different arrival time (B) with energies E_1 and E_2 such that $E_1 + E_2 = E$. (b) The events of \vec{M} are represented in the projections space. In this space, the two types of events follow two different distributions. (c) In the left (right) panel the matrix \vec{M} (\vec{M}') is represented in the projection space. It is possible to appreciate how the PCA has drastically reduced the fraction of pile-up. (d) The curve $f_3 = f_3(p_1, p_2)$, which describes the distribution of the events in \vec{M}' , is used to discriminate between the single pulse and pile-up pulses.

Fig 4.15 shows a visual representation of some of the steps of the DSVP technique. As an example the figure reports signals from a simulated TES microcalorimeter, as explained in 6.2.1. This particular case was chosen because there are just 3 non-negligible singular values, therefore the points in the projection space can be easily shown on a 3D plot.

Computational speed

The method was implemented in python, taking advantage of many of the fast modules of NumPy and SciPy. The majority of the computational time is taken by the *Raw cleaning with PCA* part, due to the fact that the SVD on the matrix \vec{M} is performed five times for each iteration. Nevertheless, the algorithm is quite fast, taking ~ 7 minutes to compute 9 iterations on a matrix \vec{M} composed of 120000 rows and 1024 columns of float32 numbers, using only one (six years old) CPU with a base clock of 2.6 GHz.

Chapter 5

Detectors performance

5.1 Experimental setup

As seen in chapter 2.3, a calorimetric experiment basically has two requirements for achieving a high sensitivity on the neutrino mass : a high energy resolution combined with a large number of recorded events. The activity of each detector must be chosen to fulfill this goal while keeping a feasible fraction of pile-up events.

Transition Edge Sensors are probably the most suitable detectors for a calorimetric neutrino mass experiment because their very high intrinsic energy resolution (the energy of single photons or electrons can be measured with resolving powers $E/\Delta E > 10^3$) can be maintained even with a multiplexed readout, allowing a relative fast detector time response at the same time.

The best detector design for the stringent Holmes requirements was previously identified with an intensive measurement campaign performed in Milano, while all the delicate steps for its fabrication were performed at NIST.

Holmes is now finally approaching the first stage of its measurement campaign: a low dose implantation detector array will be employed for a preliminary neutrino mass estimation and to assess the changes in the detectors' heat capacity. My PhD work consisted in laying the grounds for this crucial stage, from the final steps of the array fabrication to the data analysis routines and the microwave multiplexing readout of the whole array, without spoiling the detectors performance in the process.

I tested different array configurations in these years, for ease in this chapter I will refer to them as

1. *holmesDRIE*. It is the prototype array studied in [64], with the 2 μm thick gold absorber and silicon DRIE etching performed at NIST.
2. *holmesKOH* is the array with the gold already deposited and the membrane release with wet KOH silicon etching. The pixel position and the SiO_2 mask were modified respect to *holmesDRIE* to match the requirements for the KOH etching.
3. *holmesKOH Au_{a,b}* is the array configuration ready to be implanted with Holmium. All the final fabrication processes, gold sputter deposition, KOH silicon etching and photoresist removal, were performed in our laboratories as explained in 3.4. *holmesKOH Au_a* is made of 32 pixels with the target geometry for Holmes (see Figure 3.13) while *holmesKOH Au_b* is made of 32 different pixels in which the number of normal metal bars and the copper perimeter were changed.

In the following paragraphs I will outline the setup used for assessing the detector response.

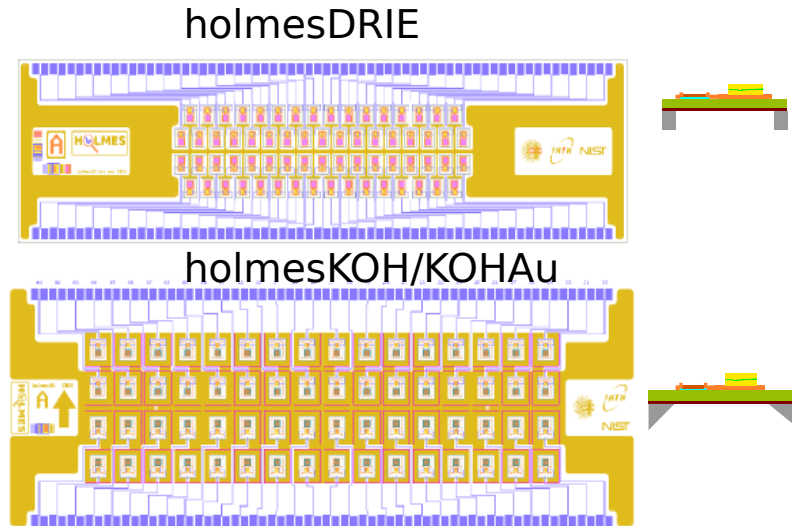


FIGURE 5.1: Holmes detector chip designs. *Top*: the chip configuration for the DRIE silicon etching, which guarantees a higher implant efficiency thanks to its close packing. *Bottom*: the chip configuration for the KOH silicon etching.

5.1.1 Cryogenic setup

In order to cool down the microcalorimeters at temperatures below the TES critical temperature ($\sim 100\text{mK}$), a $^3\text{He}/^4\text{He}$ dilution refrigerator (Triton by Oxford Instruments) is used, which provides $200\ \mu\text{W}$ of cooling power at $100\ \text{mK}$. The detector holder and the X-rays sources are thermally coupled to the coolest plate called the mixing chamber (MC). Although only one detectors holder was cooled in the runs I performed, the MC was designed to host all the 8 detector boxes in the final 1024 detectors configuration, alongside a switchable calibration source, which was not present at the time of the writing of this thesis.

The required vacuum of the order of 10^{-6}mbar is achieved using diaphragm pump ($P_{min} \sim 1\ \text{mbar}$) and a turbomolecular pump. When the cryostat is cold below 10K , the vacuum is kept thanks to the cryopump effect. A series of thermal aluminum and copper shields, firmly screwed at the different plates, prevents the thermal radiation to pass through the different temperature stages.

The rf-SQUIDs, being sensitive magnetometers, need to be isolated from external magnetic fields such as the earth's one. To this end, a large magnetic shield made of Cryoperm was mounted and coupled to the second stage pulse tube plate (2K stage). As a result, the cooling time extends from 24 hours to ~ 50 hours.

The signal from the rf-SQUIDs (TES) is readout through the microwave multiplexing technique, as explained in 3.2. The microwave probe tones must travel from the warm 300K electronics to the $20\ \text{mK}$ cold stage hosting the $\mu\text{-MUX}$ chip, limiting the heat load as much as possible. To do so, CuNi coaxial cables are used between 300K and $4\ \text{K}$.

After a $20\ \text{dB}$ attenuation at $2\ \text{K}$ in order to match the thermal noise, the signal is carried to the resonators (detectors) through stainless steel cables which have a reduced thermal load on the coldest stage, where the detectors are. Before actually entering the detector box, the probe signal is further attenuated by $20\ \text{dB}$ again, for adapting the thermal noise. When exiting the box, it passes through a circulator configured as an isolator to adapt the impedance and to isolate the resonators (detectors) from the thermal noise of the HEMT.

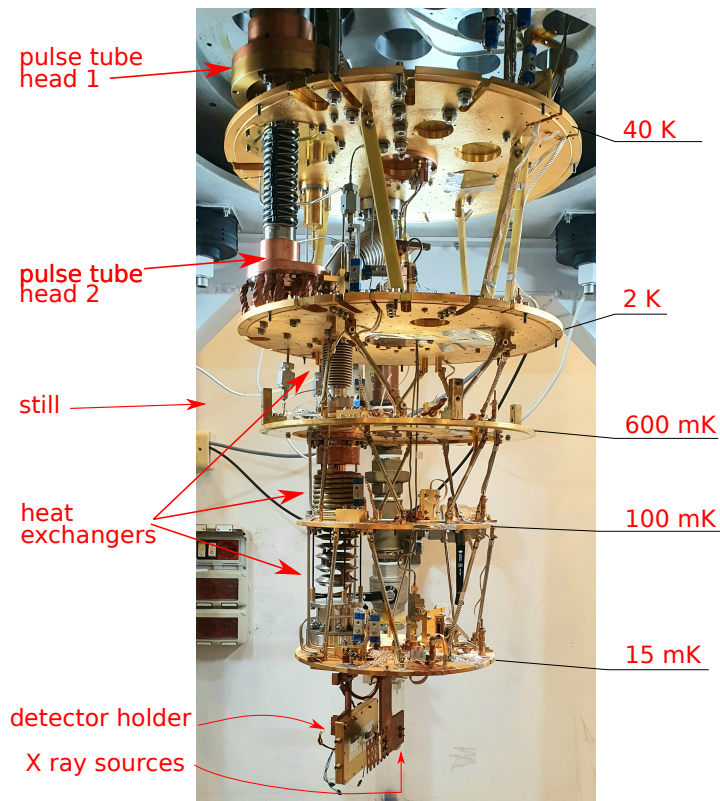


FIGURE 5.2: Picture of the Holmes dilution refrigerator

From the circulator, the signals are transmitted to a low-noise HEMT (High Electron Mobility Transistor), which is placed on the 2K plate. This connection is made with superconducting Nb coax cables to avoid dissipation of the signals, and ensuring a very low thermal conductance as well. The HEMT (*LNF – LNC48A*) has been chosen because it has a noise suited for high resolution spectroscopy with a constant gain in the bandwidth of the Holmes resonators (4-8 GHz).

All the cables mentioned before are thermalized by a simple contact between two opposite C-sections. In the future, it is planned to switch to a more robust thermalisation made with spark-plugs.

The voltage ramp signal necessary to the μ MUX multiplexing demodulation and the detectors voltage bias are carried with a Nb-Ti twisted pairs, which in turn is thermalised at each temperature stage by contact, forming a ribbon on a small copper rod screwed at each plate.

Different heaters and thermometers are spread out in the various plates, allowing us to extensively monitor and control the cryostat behavior during the measurements. Some of them are custom made, and they are monitored through other twisted pairs Cu, running along a similar path of the Nb-Ti.

With the current setup and with one holder box (128 detectors, two rf cables), the MC can reach the base temperature of 18 mK which is ideal at this phase because it allowed to study the detectors response in a wide range of initial condition. With the final configuration (1024 detectors, 4 HEMT and 8 rf cables and spark plug thermalisation) we do not expect this temperature to significantly vary, still allowing us to operate the detectors in their best conditions.

5.1.2 Warm Electronic setup

The HOLMES read out and multiplexing system is based on electronics developed for the readout of microwave kinetic inductance detectors (MKIDs) for the MUSIC and ARCONS experiments [62]. These readout systems are themselves based on the 2nd-generation Reconfigurable Open Architecture Computing Hardware (ROACH2) platform.

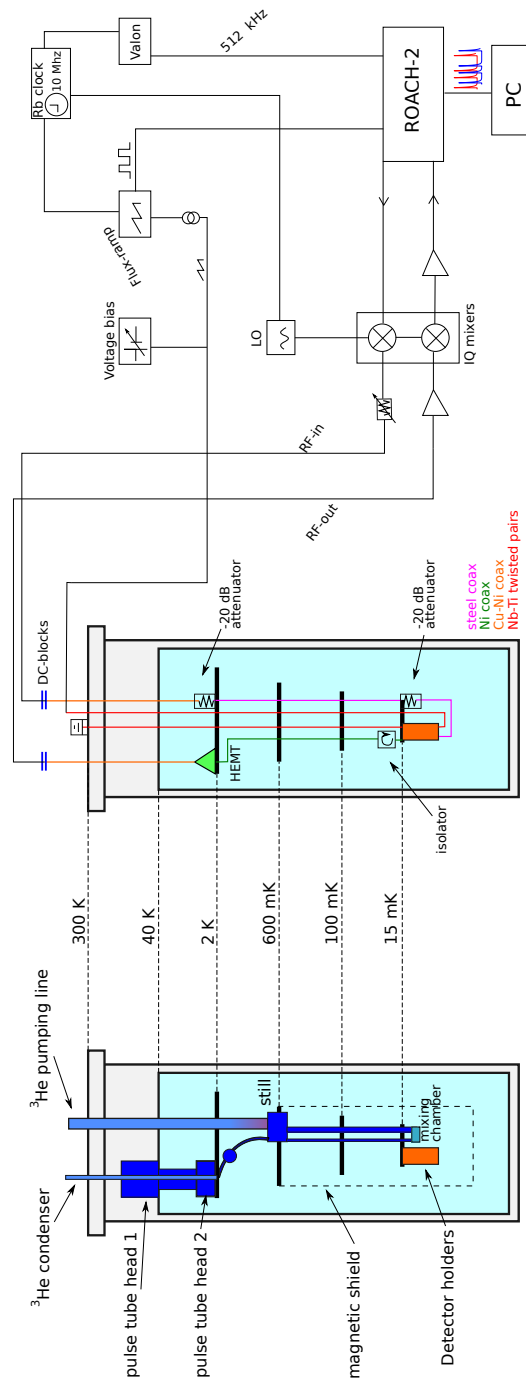


FIGURE 5.3: Scheme of the electronic setup inside and outside the cryostat.

The system is composed of a digital board (ROACH2), that accommodates a Xilinx Virtex

6 FPGA for the signal processing and a PowerPC 440EPx for the slow control, and of a peripheral DAC/ADC board that hosts two DACs (1000 MS/s, 16 bit, 75 dBc of NSD) and two ADCs (550 MS/s, 12 bits, 64 dB of SNR) to generate and acquire the in-phase and quadrature signals.

The multiplexing is based on a heterodyne mixing scheme. The sinusoidal probe tones, one for each microresonator to readout, are generated by a FPGA by implementing a Direct Digital Synthesizer (DDS) and using an external clock source. The resulting I and Q components are generated in a baseband frequency range (10-512 MHz) by two high speed digital-to-analog converter (DAC).

The up-conversion in the RF frequency range (4-8 GHz) suitable for the multiplexer chip is performed by mixing I and Q with a local oscillator (LO). Holmes uses a PXIe Hybrid with a commercial design from Polyphase Microwave but customized to match the Holmes requirements, i.e. to work in C-band (4 to 8 GHz) in order to be fully compatible with the HEMT bandwidth while having a total loss around 7 dBm, compatible with the power needed to excite 32 resonators. The RF-tones passes through an adjustable step-attenuator and then are sent into the cryostat. The modulated output tones are amplified with a gain of 26 dB and then down mixed from RF to baseband by exploiting the same IF board with the same LO signal. The output signals I and Q from the IF board are amplified again to exploit the full dynamic range of the two high speed analog to digital converters (ADCs). The FPGA firmware implements signal processing algorithms that separate the tone frequencies (channelization), reconstruct each sensor response from the modulated tones by extracting the amplitude and phase at each resonator frequency and finally deconvolving the flux ramp modulation.

In order to synchronize all the components of the system (ADCs, DACs and FPGA and LOs) a common external clock provided by a rubidium frequency standard is used. The acquired data are transmitted from the ROACH2 board to the data acquisition computer through a 10 Gb/s ethernet connection.

The flux-ramp and the voltage bias generators play a crucial role in the reconstruction of the signal and in the detectors stability respectively. For the former, any disturbance, such as ground-loop and electromagnetic interference, must be suppressed. As described in [82], we used a custom coupling transformer between the signal generator and the input to the cryostat to decouple it from the instrumentation rack. For the latter, the bias need to be as stable as possible, therefore a linear power supply designed to achieve a stability of \sim ppm/ $^{\circ}$ C stability, in combination with two large battery are used in each measurement.

5.1.3 Holder setup

The detector holder is a $10.5 \times 7.5 \times 0.85\text{cm}^3$ made of gold-plated copper to avoid oxidation and maintaining a high thermal conductivity. Its design was changed respect to the one reported in [64] to hold the final configuration of Holmes chips. Each holder is now hosting 2 detectors array (4×32 pixels) for a total of 128 detectors with their respective readout and bias chips. I tested various bonding process for each chip, resulting in the configuration summarized below and in Figure 5.4. Each electrical bonding was performed in Milano with 25 μm diameter Al bonding wires.

- **Readout chip** The readout chip is a $\mu\text{mux}17\text{a}$ multiplexer chip developed by NIST and optimized for Holmes. It consists of 33 quarter-wave resonators coupled to as many rf-squids, made from 200 nm thick Nb film deposited on high-resistivity silicon. One of the resonators, called the dark squid (DS), is not connected to a detector and can be used for testing. To avoid odd propagation mode in the feedline due to an electrical imbalance between the ground planes [83] which results in an overall

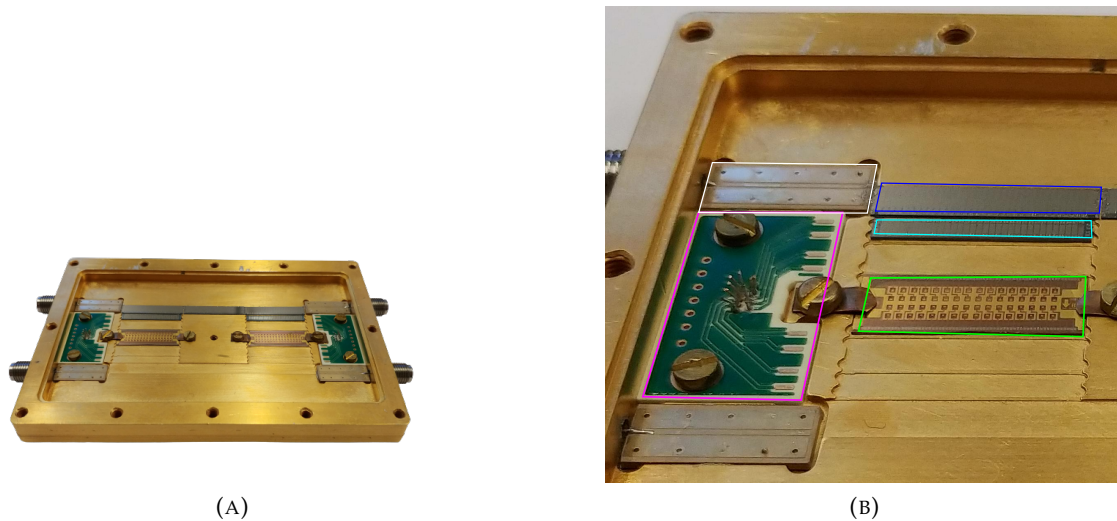


FIGURE 5.4: (A) Final design for the detector holder box. In this picture, only 64 of the 128 detectors are connected to the μ MUX chips. (B) Zoom of the previous picture, in which the main components are highlighted: the TES chip in green, the bias (resistance) chip in cyan, the PCB in magenta, the μ MUX in blue and the CPW in white. The inductance chip can be positioned between the bias chip and the TES chips.

distortion of the resonance profiles, we implemented airbridges across the feedline and from the chip to the box ground, both near north and south side of the chip. As shown in 5.5, this greatly improves the resonances profiles resulting in a lower readout noise and a more effective rf-tuning procedure.

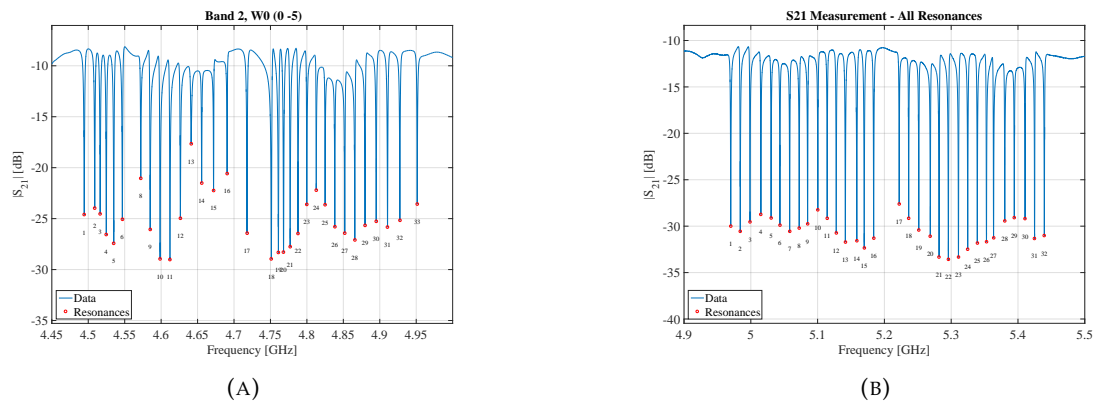


FIGURE 5.5: Example of the resonances profiles before (A) and after (B) airbridges bonding across the feedline. The resonances are deeper and more uniform across the bandwidth of the chip. In (B) one of the resonances is missing because it was damaged.

- **Bias chip** As explained in section 3.1, each TES need to be connected in parallel with a small resistance, indicated as R_L . These resistances have the value of 0.3 m Ω and are located below the readout chip.
- **Inductance chip** An important parameter is the inductance L that is added to the TES electrical circuit to slow the leading-edge of the pulses (from [?] $\tau_+ = \tau_R \propto L$).

In [64], an additional inductance of 50 nH was necessary to slow the detectors down. However, it was observed that in the current configuration the long bonding wires that connect the bias chip to the detectors provide a stray inductance comparable to the previous one, making the inductance chip no longer necessary.

- **TES array** The TES chip was designed by NIST to match the Holmes requirements. It consists of 2 modules of 32 detectors each, with bonding pads for the bias on both side of the chip. It is held in place by elastic Cu-Be clips, while the thermalization is done with various Au bonding of 25 or 50 μm diameter that connect the gold plates around the detectors to the holder.
- **PCB** The Printed Circuit Board has 8 available pins for the ramp and the TES bias.
- **CPW** The rf launchers are Coplanar waveguides, glued with silver epoxy for grounding the planes to the copper holder.

To avoid constraining the copper thermal contraction to the one of the silicon, the readout and the bias chip was glued with rubber cement coated on the east and west side of the chip.

The holder cover has two holes above the detectors chip covered with a 6 μm thin aluminum foil to block the external thermal radiation, allowing at the same time the X-rays from the external calibration sources to hit the detectors.

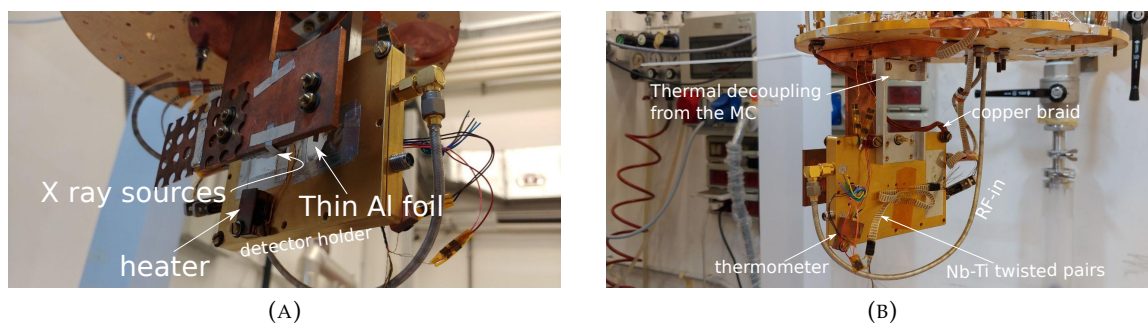


FIGURE 5.6: (A) Front view of the detector holder setup, facing the X-rays fluorescence sources. (B) Back view of the detector holder.

Two different configurations for the thermalization of the holder to the mixing chamber were tried: an aluminum support to thermally decouple it from the MC plate with two copper braids for the weak thermal connection and a copper support to strongly couple it with the MC. In the former case, the temperature stabilization was made with a heater and thermometer (controlled with a AVS-47 resistance bridge and TS-530A temperature controller by PICOWATT) screwed on the back of the holder, as shown in Figure 5.6, while for the latter it was accomplished by the default instrumentations on the MC (Lakeshore 370 AC). No substantial differences were noticed in the detectors thermal drift between the two configurations, therefore the latter configuration was primarily used.

5.1.4 Calibration sources

In the measurements performed in this chapter we used two ^{55}Fe sources pointing at a mixture of NaCl and CaCO_3 . These fluorescence targets were chosen because they provide X-rays in the energy range of interest for HOLMES, allowing to correctly calibrate and study the detectors response.

The $K_{\alpha 1}$ and $K_{\alpha 2}$ are asymmetric distributions, that were modeled as Cauchy with an asymmetry parameter δ , defined as the ratio between the half widths at half height on the low and high energy sides of the peak or, more accurately, as the weighted sum of n symmetric Cauchy distributions. The parameters used for the different peaks are reported in Table 5.1.

Element	line	I	γ	δ	E [eV]
Mn	$k_{\alpha 1}$	0.353	1.715	1	5898.853
		0.141	2.043	1	5897.867
		0.079	4.499	1	5894.829
		0.066	2.663	1	5896.532
		0.005	0.969	1	5899.417
	$k_{\alpha 2}$	0.229	2.361	1	5887.743
		0.110	4.216	1	5886.495
Ca	$k_{\alpha 1}$	1	0.98	1.15	3691.68
	$k_{\alpha 2}$	1	0.98	1.13	3688.12
Cl	$k_{\alpha 1}$	1	0.72	1	2622.39
	$k_{\alpha 2}$	1	0.72	1	2620.77
Al	$k_{\alpha 1}$	1	0.85	1	1486.88
	$k_{\alpha 1}$	1	0.85	1	1486.45

TABLE 5.1: Parameters used to model the X-ray calibration sources peaks.

In the future it is planned to setup a switchable calibration source similar to the one used in [33] with the same target as the one that was used in this thesis. The source will be crucial not only for the detectors calibration, but also for the correction of the detectors thermal drift in the ROI, as explained in 4.3.3.

5.2 TES time profile

The signal time profile plays a crucial role in the expected sensitivity of the Holmes experiment, because its rise (RT) and decay time (DT) must be tuned to be as short as possible to minimize the fraction of pile-up events and the dead time while keeping the single detector activity high. Adjusting the components of the electrical circuit of the TES bias and carefully designing the detectors geometry allow to tune their value to meet the experimental requirements.

It's worth noticing that due to the fact that the thermalization process occurs within a time scale of few hundred of picoseconds, the TES has an extremely fast intrinsic response. However, because the sampling time is fixed by the readout bandwidth, the detectors response must be slowed down to have a sufficient number of samples to precisely reconstruct the pulse profile. In addition, the pulse slew rate must be lower than the slew rate of the ramp to satisfy the requirements of the microwave multiplexing technique.

On the other hand, if the rise time is too slow the decay time has to be slowed down too, to preserve the high signal to noise ratio. With the selected detector design and with the current chip setup, the detectors show a rise times of 10 – 20 μ s, as pictured in Figure 5.8. With the current array (*holmesKOH Au*), it is difficult to represent a distribution of the RT that reflects the differences between the detectors because, as we shall shortly see, under

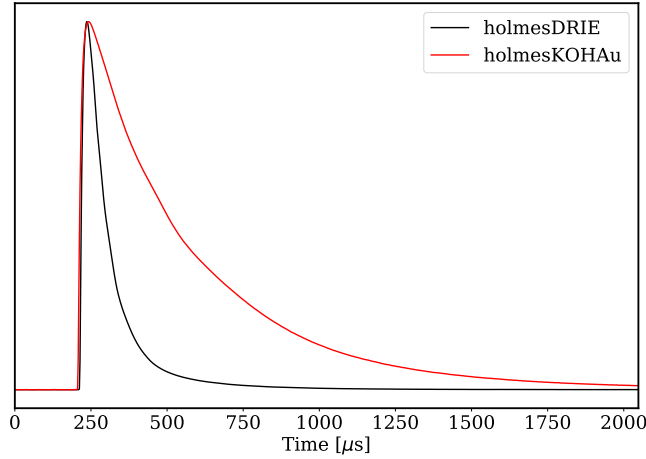


FIGURE 5.7: Examples of *holmesKOH Au* (run 55) and *holmesDRIE* (Run 37) TES responses to a Mn K_{α} photon normalized to their amplitudes. The pulse from Run 55 presents a longer recovery time. For these TESs the recovery process requires more time and hence the probability of having a pile-up event on their tail is higher.

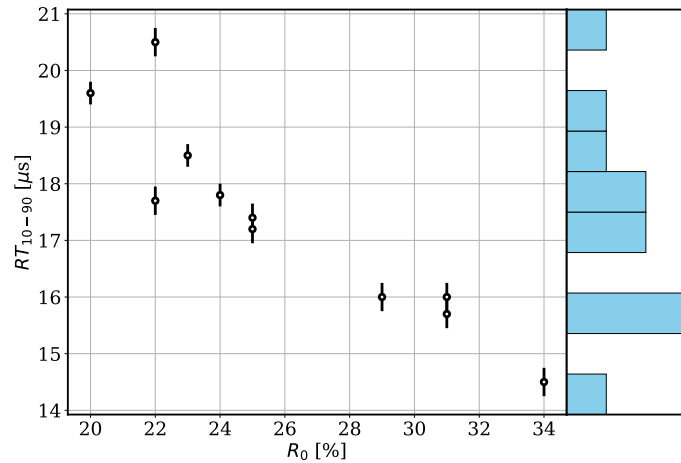


FIGURE 5.8: Example of the RT distribution in the *holmesKOH Au* chip (Run 57, measure 5)

the same conditions the TESs work at different temperatures, i.e. they have different values of $R_{TES}(I, T)$, and their rise time changes as expected from 3.14. Nevertheless, their RT is of the order of 20 μs which is well suited for the Holmes goals.

On the other hand, the detectors decay time in the chip processed with the KOH etching is not ideal. It went from $\simeq 70 \mu\text{s}$ of decay time of the *holmesDRIE* [64] to $\simeq 300 \mu\text{s}$ of the *holmesKOH(Au)*. As explained in 4.1.1, its important to have a fast decay time because it sets the length N of the recorded window so that the optimum filter can estimate precisely the amplitude (energy) of the pulse. N , in turn, defines the dead time of the measurement. The DT depends on the slope of the TES resistance and on the thermal conductance between the detector and the thermal bath G . While the former has been verified that has not changed between the two productions, G might have due to the different fabrication

processes used. The variation in DT can also be due to a variation in the heat capacity of the detectors but, the fact that the reduction in DT was observed both in *holmesKOH* and in *holmesKOH*Au seems to exclude a problem related to the Au deposition.

By acquiring characteristic IV curves at different bath temperatures, it was possible to measure the thermal conductance toward the bath of our devices.

In fact, from the IV curves we can extract the TES resistance R_{TES} and current I_{TES} by varying the applied voltage bias V_{bias} at a fixed MC temperature T_{bath} , which is kept below the device critical temperature. From them, P_{bath} can be evaluated as

$$P_{bath} \text{ at equilibrium} = P_J = I_{tes}^2 R_{tes} \quad (5.1)$$

$$\begin{aligned} P_{bath} &= k(T_{tes}^n - T_{bath}^n) \underset{G \equiv dP_{bath}/dT_{tes}}{=} \frac{G}{nT_{tes}^{n-1}} (T_{tes}^n - T_{bath}^n) = \\ &= \frac{GT_{tes}}{n} - \frac{G}{n} \left(\frac{T_{bath}}{T_{tes}} \right)^n T_{tes} \end{aligned} \quad (5.2)$$

I chose a TES resistance at 70% of its normal resistance in the transition range for computing the Joule heating power. In this 'high resistance' state I will assume that also T_{tes} is nearly constant and from now on I will simply call it T_c .

By studying the behavior of the TES at different bath temperatures it is possible to evaluate the thermal conductance towards the heat bath, as shown in Figure 5.9.

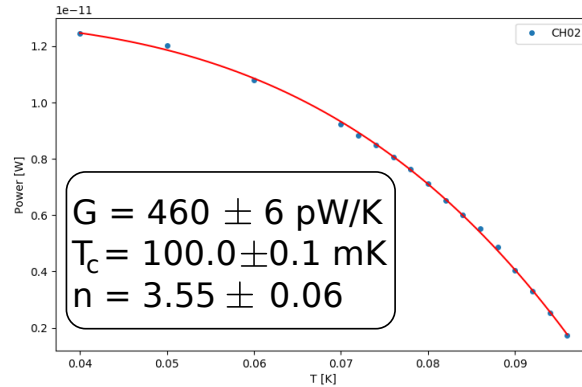


FIGURE 5.9: Example of a measurement of the thermal conductance of a *holmesKOH*Au detector.

The small variation in the TES critical temperature T_c , of the order of 2 % for *holmesKOH*Au (Figure 5.11), represents a first good indication that the thermometers produced in these two batches are virtually identical.

While the measured value of n seems to confirm the fact the 0.5 μm thickness of our SiN membrane allows the phonon propagation to pass from the 3D regime ($P \propto T^4$) to the 2D ($P \propto C_1 \times T^3 + C_2 \times T^{5/2}$ for a pure ballistic transport [66]), the G have been reduced by a factor of 0.25-0.5 compared to the expected value of $\simeq 600\text{pW/K}$ from the *holmesDRIE* to the *holmesKOH*(Au).

The thermal conductance G of SiN membranes at low temperatures is often dominated by surface scattering effects, resulting in a photon transport near the Casimir limit rather than the ballistic one. It is possible that this diffusion phonon transport is the main cause of the increase of the detectors decay time. However, the large variation of G and its apparently

random spatial distribution along the pixels (Figure 5.10) in combination with the fact that the measured etched area was the correct one, is also an indication that there could have been some issues with silicon wafer production rather than an un-uniform silicon etching.

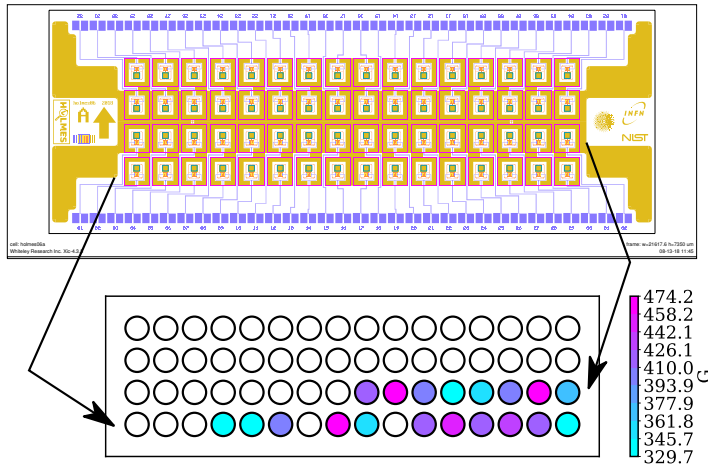


FIGURE 5.10: *holmesKOH Au* chip: the colors indicate the measured thermal conductance G in Run 56. No geometrical pattern can be identified for the G values

In fact, if the silicon surface was not perfectly flat and smooth the membrane, which is deposited above it, would also present a rough surface that, once the silicon underneath is removed, would lead to a diffusive propagation of phonons with an overall effect of reducing G .

To test this hypothesis, G will be measured on a different chip that was fabricated with the same procedure as the *holmesKOH(Au)* but with a DRIE silicon etching.

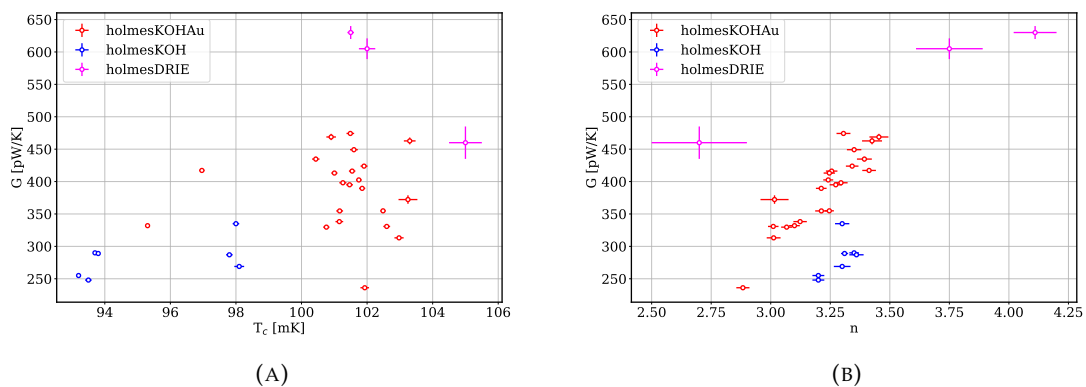


FIGURE 5.11: Distribution of the thermal conductance G , the critical temperature T_C and n for the three different detector chip studied.

5.3 Noise spectrum with a 32 channels array

The noise power spectrum of a single detector is the sum of the noise of the SQUID, of the Johnson noise due to load resistor and due to the TES, and the noise of the thermal fluctuation through the thermal conductance G . I indicate with SQUID noise the total readout noise associated with the SQUID, which includes the rf-SQUID noise, the Two Level System noise and the HEMT noise, where the latter is by far the most significant component of the readout chain.

In reality, the noise power spectrum is also affected by other contributions related to the microwave multiplexing technique. Some of which are inherently related to the flux ramp modulation, which impose a noise penalty of the order of $\sqrt{2}$ [62] compared to other readout technique such as the flux-locked loop readout, while others are common among the radio frequency systems. Among these, intermodulation distortions (IMD) due to the presence of non-linear elements anywhere in the readout (DACs, μ MUX, HEMT, etc.) will introduce unwanted frequencies that can fall in the bandwidth of the signal.

The main consequence is that achieving a noise spectrum which do not spoil the excellent intrinsic detectors energy resolution requires meticulous attention during the probe tones setup, carefully tuning the amplitude and the relative phases of each tones generated by the DACs. Its worth noticing that increasing the number of detectors (tones) will also inevitably increase the strength of these effects.

With our setup, the main obstacle is related to the lowest frequency that the ROACH2 DDS can generate. The fact that the DDS can produce only frequencies that are in units of 15.26 Hz will introduce a “fence” of equally spaced frequencies peaks in the frequency domain, as shown in Figure 5.12. The causes of this effect are not trivial and not yet fully understood.

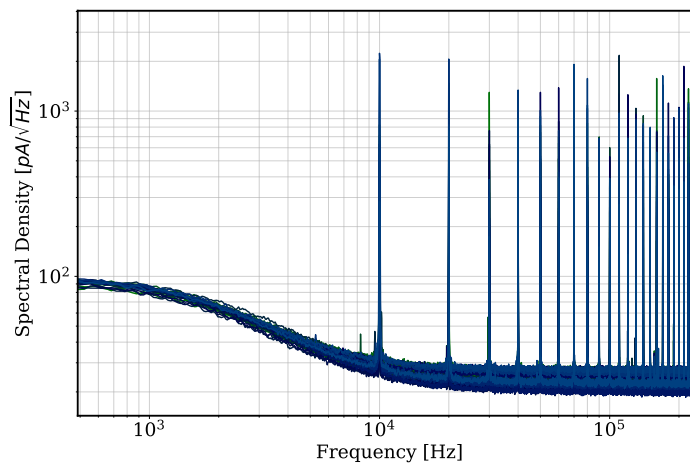


FIGURE 5.12: Noise Power Spectral Density (PSD) of 32 unbiased TESs (Run 60, measurement 13), only the R_L noise and the SQUID readout noise are present. IMD due to the DDS common frequency is also evident.

We saw that increasing the minimum frequency of the DDS by a power of 2^n will shift to higher frequency the “fence” by an equal factor, thus to solve this the precision in the probe tones generation must be decreased to shift the noise peaks out of the detector bandwidth. This in turn requires high quality resonances in order to not distort the TES signals during the demodulation. As explained in 5.1.3, this was achieved by increasing the number of ground bonding in the μ MUX chip.

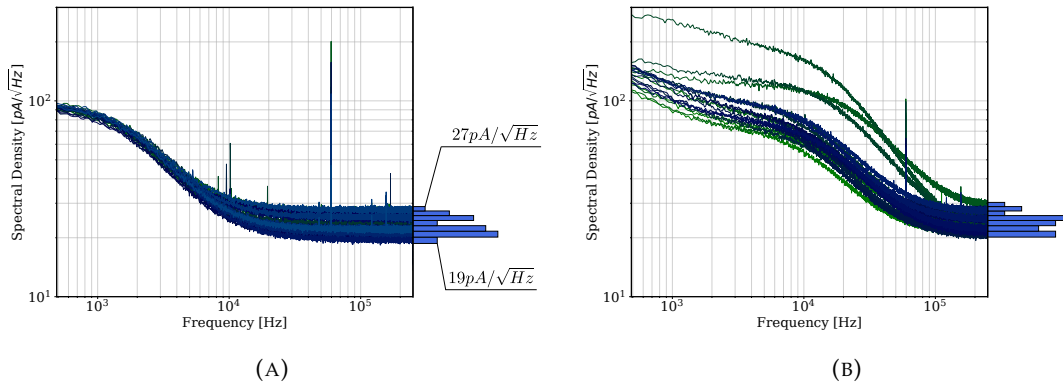


FIGURE 5.13: (A) Same as Figure 5.12, but the IMD was moved out of the TESs bandwidth by changing the the minimum frequency that the DDS can generate from 15.26 Hz to $\sim 250 \times 10^3$ Hz. The minimum and the maximum readout noise achieved are highlighted. (B) Same as Figure (A), but with the TES bias on. The different PSDs is due to the different geometries that were present on the chip.

Figure 5.13 shows the final noise spectrum of our 32 μ MUX chip connected to the resistance chip and to the detectors array. We can see that the readout SQUID noise, including IMD, produce an optimal flat noise spectrum between 19 and 27 pA/\sqrt{Hz} , which is low enough to have negligible impact on the resolution of the microcalorimeters. From the *holmesKOH*_{Au_b chip, I focused on the baseline detector of Holmes and fitted its noise power spectrum using the equation (3.19). The parameters estimated are reported in Table 5.2 and are comparable with the ones expected from previous measurements [64] and with the new thermal conductance's.}

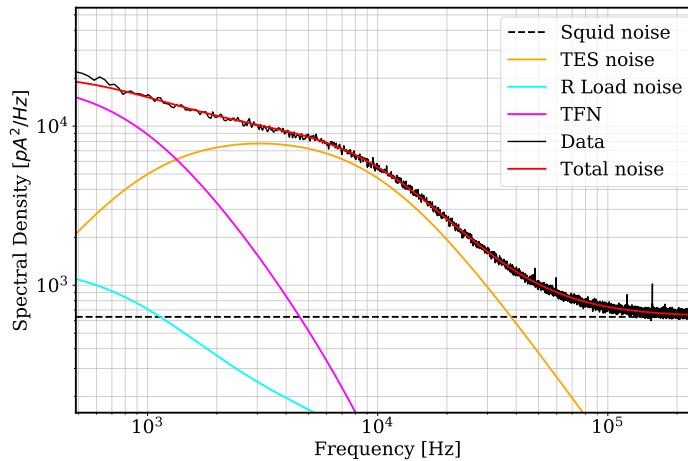


FIGURE 5.14: Simulated noise power spectrum compared to the one acquired during Run 55 for the baseline Holmes detector.

$G = 450 \text{ pW/K}$	$R_0 = 1 \text{ m}\Omega$	$C = 0.8 \text{ pJ/K}$
$T_{bath} = 0.03 \text{ K}$	$\alpha = 120$	$\beta = 2$
$L = 38 \text{ nH}$	$R_N = 6 \text{ m}\Omega$	$n = 3.7$
$T_c = 0.1 \text{ K}$	$M = 1$	$R_L = 0.3 \text{ m}\Omega$

TABLE 5.2: TES parameters used to emulate the noise PSD of a *holmesKO-HAu* TES in Run 55 (Figure 5.14).

5.4 Energy resolution

As explained in section 2.3, to achieve the target neutrino mass sensitivity Holmes must fulfill stringent requirements in terms of pile-up rejection and energy resolution. However, simulations have shown that with the target activity of 300 Bq, the correlation between neutrino mass sensitivity and energy resolution diminishes as long as the latter remains below 10 eV. A more stringent energy resolution may be required in the first phase of Holmes, where an activity of a few Bq will be achieved, to obtain a meaningful result. To estimate the energy resolution, the detectors have been illuminated with fluorescence X ray sources (sec 5.1.4). The goal of these measurements was to check if the energy resolution of the baseline detector of Holmes remains unchanged despite the different fabrication process of the array.

Before discussing the results, it is worth stressing that the comparison has been made by fitting the calibrated amplitude at the Mn peaks because their complex intrinsic structure is well known compared to the other peaks. Also, in spite of the fact that all the detector of the arrays were measured at the same time, the spread of the thermal conductances G prevents us to make a fair comparison between the various pixels of the array. In fact, the detectors response, as well as the energy resolution, strongly depends on the initial condition of the TES, resulting in TES with the same geometry but different working points showing different energy resolutions.

The procedures to produce a calibrated spectrum (data reduction, optimal filtering and drift corrections), are explained in 4. The resulting spectra are fitted with the characteristic line profile (Table 5.1) convoluted with the gaussian response function of the detector. Hence, the energy resolution ΔE is defined as the FWHM of the gaussian response. The results are shown in Figure 5.15, 5.16, 5.17 for the three different chip studied.

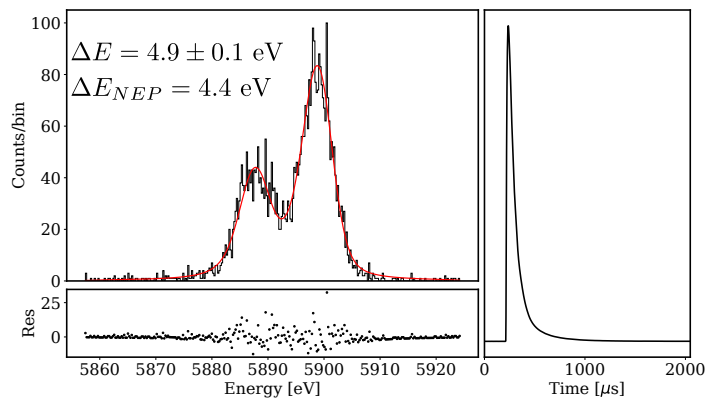


FIGURE 5.15: TES resolution on the 5.9 keV Mn K_{α} peak for a *holmesDRIE* TES (Run 37, measurement 14). On the side, the TES time profile is shown.

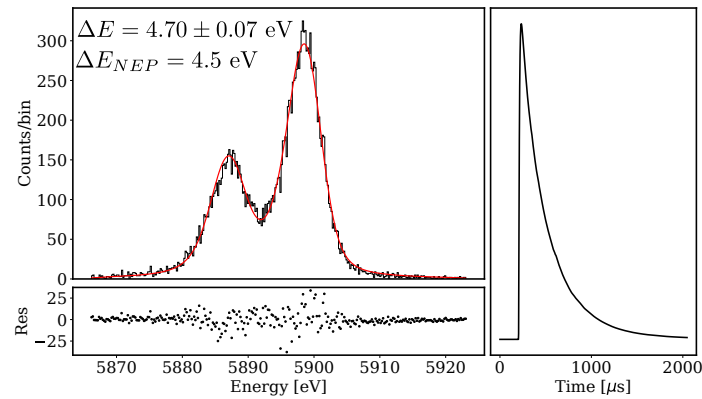


FIGURE 5.16: TES resolution on the 5.9 keV Mn K_{α} peak for a *holmesDRIE* TES (Run 54, measurement 1). On the side, the TES time profile is shown.

I would like to emphasize that the energy resolutions achieved are very close to the one predicted by the noise spectrum, called ΔE_{NEP} , indicating that the analysis procedures have preserved the energy resolution of the detector.

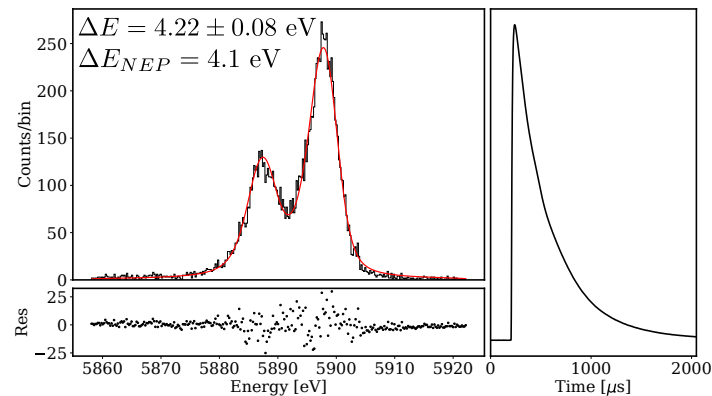


FIGURE 5.17: TES resolution on the 5.9 keV Mn K_{α} peak for a *holmesKOH Au* TES (run 55, measurement 2). On the side, the TES time profile is shown.

In conclusion, the fabrication process did not spoil the TES performance in terms of energy resolution. This, in combination with the successful multiplexing readout of a full 32 pixels array, represent an important achievement and significant step toward the first neutrino mass measurement of Holmes.

Chapter 6

Background studies

Considering that the count rate is particularly low in the region of the holmium spectrum near the end-point, ~ 0.26 counts $\text{eV}^{-1} \text{ day}^{-1} \text{ det}^{-1}$ for the energy region [2650, 2833] eV, the fraction of background signals must be kept as low as possible to avoid artifacts that would inevitably impair the the determination of the neutrino mass.

The background sources can be roughly divided into the following components:

1. **Pile-up.** We define a pile-up event a signal composed of two events of energies E_1 and E_2 which occur within a time interval shorter than the time resolution of the detector, producing a signal which is misinterpreted as a single signal with energy $E \simeq E_1 + E_2$. Thus, if not correctly identified, pile-up events will distort the decay spectrum of ^{163}Ho , lowering the sensitivity to m_ν .
2. **Radionuclides in the detectors' absorbers.** The custom ion implanter is designed in such a way to optimize the ^{163}Ho implantation efficiency. Nevertheless, radioactive contaminants from the embedding process are expected inside the gold absorbers. Among these, the ^{166m}Ho (β decay, $Q_\beta = 1854$ keV) represents the most dangerous one because it presents a 'fast' decay time of $\tau_{1/2} \sim 1200$ years, so even a small quantity can produce a flat but non negligible background spectrum in the ROI.
3. **Natural radioactivity.** Radioactive contaminants which are present in all the parts of the experimental setup, from the laboratory to the cryostat and the detector's holder.
4. **Cosmic rays.** Muons from cosmic rays interacting directly with the detector will produce a signal which is theoretically indistinguishable from the ^{163}Ho ones. Additionally, muons interacting with the experimental apparatus could create secondary products, increasing the total background rate.

With the goal activity per pixel of 300 Bq of Holmes, the pile-up will be the main background source, with a count rate of ~ 0.8 counts $\text{eV}^{-1} \text{ day}^{-1} \text{ det}^{-1}$ in the energy region [2650, 2900] eV, given a time resolution of $1.5 \mu\text{s}$. Therefore, its reduction is crucial for the success of the experiment. As it will be explained in section 6.2, two different algorithms were successfully studied for this goal, allowing to reach an expected time resolution of $1.5 \mu\text{s}$, a factor of two lower than previously studied technique [84].

As regards the ^{166m}Ho , Monte Carlo simulations show that with the ion implanter in the current configuration the $^{163}\text{Ho}/^{166m}\text{Ho}$ separation is expected to be better than 10^6 , which results in a count rate contribution in the ROI of < 0.01 counts $\text{eV}^{-1} \text{ day}^{-1} \text{ det}^{-1}$ with 300 Bq of ^{163}Ho . In addition, considering that the Holmes experiment is located at the cryogenic laboratory of the University of Milano-Bicocca at a depth of roughly 20 meters below ground, and that the Transition Edge Sensors have a sensitive area of the order of $5 \times 10^{-8} \text{ m}^2$ and a thickness of a few micrometers, the background contributions due to both cosmic rays and natural radioactivity are expected to be negligible compared to pile-ups.

However, natural radioactivity and cosmic ray induced events may become comparable or even overcome the pile-up rate if the ^{163}Ho activity per pixel is too low. This will be the case during the first Ho implantation campaign, where the activity per pixel will be kept low to evaluate how the detectors performances are affected by the presence of the Ho inside the absorbers. Therefore, assessing the expected background rate and keeping it as low as possible is mandatory for the success of the first stages of Holmes. The measurements done toward this goal are presented in the next section.

6.1 Natural radioactivity and cosmic rays

In general, radionuclides present in our environment can be grouped in three categories: primordial, cosmogenic, and anthropogenic (man-made). They are present in the air and laboratory building materials as well as in the cryostat components and in the detectors' holder. Radionuclides which are naturally present on the surface of the detectors could be enclosed in the bulk of the absorbers by the Au co-deposition process. To quantify the concentration of radionuclides and the cosmic rays flux in the laboratory, a six days measurement was performed with a HPGe close to the cryostat without the detectors holders, resulting in the energy spectrum shown in Figure 6.1.

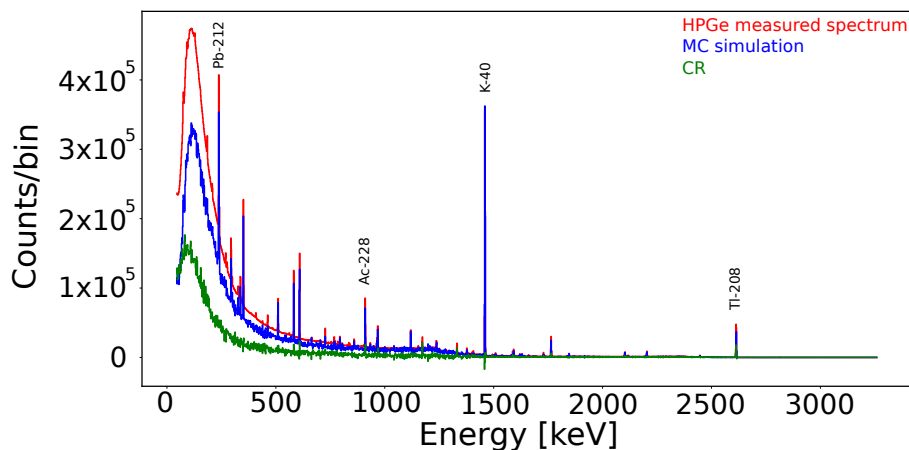


FIGURE 6.1: HPGe gamma ray spectrum measured in Milano-Bicocca cryogenic laboratory. The CR spectrum is the difference between the measured and the simulated one.

Through this measurement we identified 84 peaks and, as expected due to the experiment location, the main radionuclides were primordial radionuclides, i.e. those from the radioactive decay chains of the ^{232}Th and ^{238}U , and ^{40}K . Even if potassium has a ^{40}K natural abundance of 0.01%, its contribution is comparable to the ones from Th and U because of its greater abundance in the soil.

By removing from the measured spectrum the expected contribution of the radionuclides evaluated with a MonteCarlo, it was possible to achieve a preliminary estimation of the cosmic rays contribution to the total HPGe activity to 29%.

Each contribution of these radioactive sources to the actual background spectrum of our microcalorimeters is complex to quantify because as thermal detectors they are sensitive to all type of radiations but, due to their small volumes ($200 \times 200 \times 2 \mu\text{m}$ for the gold absorber), they are almost transparent to gamma rays. In addition, the detectors are located in a gold

plated copper holder at the bottom of the cryostat, in vacuum and surrounded by copper and aluminum shields at cryogenic temperature.

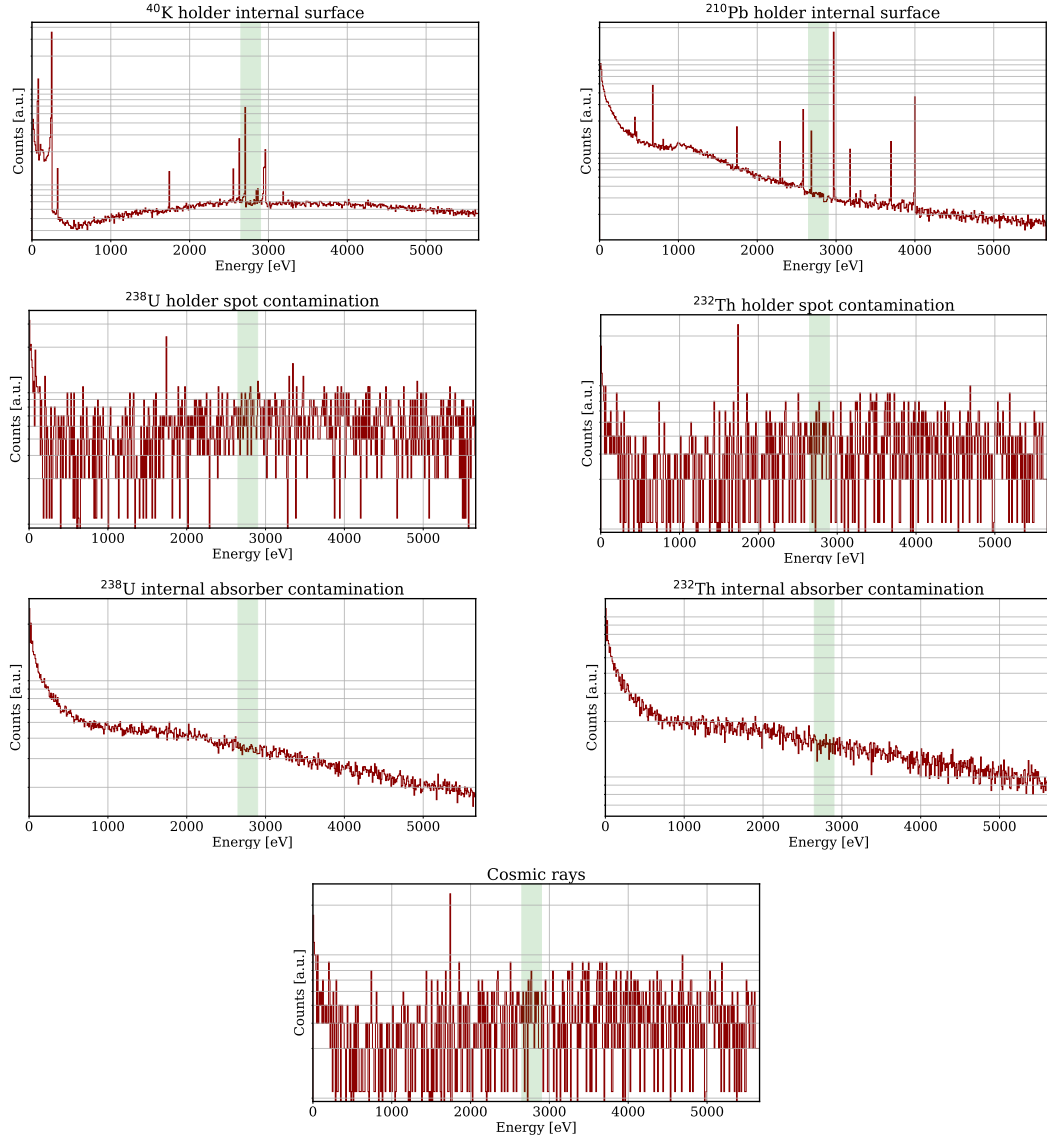


FIGURE 6.2: The resulting spectra of Geant4 Monte Carlo simulations. The green region highlights the Holmes region of interest.

A Monte Carlo simulation was performed, using Geant4 10.3, with *G4EmLivermorePhysics*, *Fluo*, *Auger*, *Pixe* and *Atomic Deexcitation*. The detectors were approximated as cylinders of 0.226 mm diameter and 2 μm thickness above a holey Si substrate and inside a cylindrical copper holder (Fig 6.3). Different energy spectra were generated by placing the radionuclides ^{238}U , ^{232}Th , ^{40}K and ^{210}Pb inside and on the surface of both the gold absorbers and the copper holder. Also a spectrum produced by a “cosmic ray source” above the detector was produced. Some of the resulting energy spectra are shown in Figure 6.2.

All the simulated background sources but the ^{40}K produce a smooth and almost flat background in the ROI. The ^{210}Pb present a peak near the low energy (high statistic) edge of the ROI, and therefore its contribution is expected to be negligible.

Due to the ^{40}K peaks position in the region of interest, the impact of the contamination of ^{40}K on the neutrino mass determination deserves to be further investigated, and this is done in section 6.1.7.

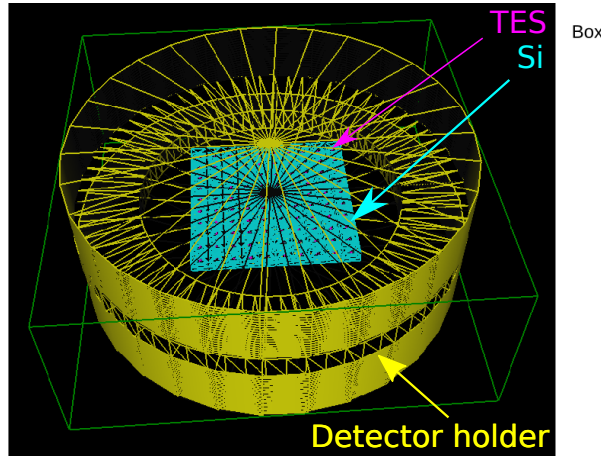


FIGURE 6.3: The detectors holder and chip configuration used for the MC simulations. Each simulated detector, depicted in pink, has an equivalent total area of the real TES ($200 \times 200 \mu\text{m}^2$).

A background measurement was performed without the external calibration source and with an array of 32 detectors. Three scintillators were placed under the cryostat to recognize the contribution of muons and muon-induced events. The measurement was done during the month of August and lasted about 500 hours. The purposes were to estimate the rate of background events and to determine the fraction of cosmic rays interactions.

6.1.1 Experimental setup

Three organic plastic scintillators were installed under the cryostat as shown in figure 6.4.

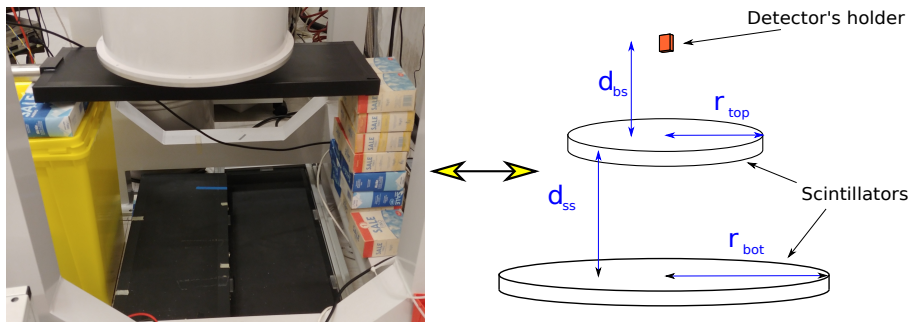


FIGURE 6.4: *Left*: A side view of the experimental setup, in which the position of the three organic plastic scintillators below the cryostat is shown. *Right*: The schematic of the scintillator and detector holder positions. For ease, the scintillators slabs have been approximated as circle of equivalent area.

Their relative distance and the distance from the detectors was chosen to cover a solid angle of 0.55 steradians from the vertical. The cosmic rays flux angular distribution goes as $I \sim \cos(\theta)^2$, where theta is the zenith angle, thus the scintillators setup should measure the muons hitting the detectors array with a geometric efficiency of roughly 50%.

The logic chain is shown in Figure 6.5. The bias voltage of each scintillator was set to match the characteristics of the discriminators, while the discriminator threshold was set to remove the signals due to low energy natural radioactivity. The coincidence further reduce its contribution. The final measured rate of coincidence signals was approximately 7 Hz, corresponding to a cosmic ray vertical flux of approximately $I \simeq 0.2 \text{ cm}^{-2} \text{ min}^{-1}$. This value is in agreement with the one expected with an overburden mass m_{ob} of 18 mwe, measured in previous studies [85]. Indeed, considering that the integral intensity of muons above 1 GeV/c at sea level is $I_{sea} \simeq 1 \text{ cm}^{-2} \text{ min}^{-1}$ [86], the attenuation A_μ due to the location of the cryogenic laboratory is, following the empirical relation [87]

$$\begin{aligned} A_\mu(m_{ob}) &= I/I_{sea} = 10^{-1.32 \log_{10} d - 0.26(\log_{10} d)^2} \simeq 0.23 \\ d &= 1 + m_{ob}/10 \end{aligned} \quad (6.1)$$

which is comparable to the one we have measured. m_{ob} is the overburden mass in mwe and d can be interpreted as the total overburden (atmosphere included) measured in number of atmospheres.

Because of the microwave multiplexing readout technique, syncing an external signal with the output signals from the detectors array is not trivial.

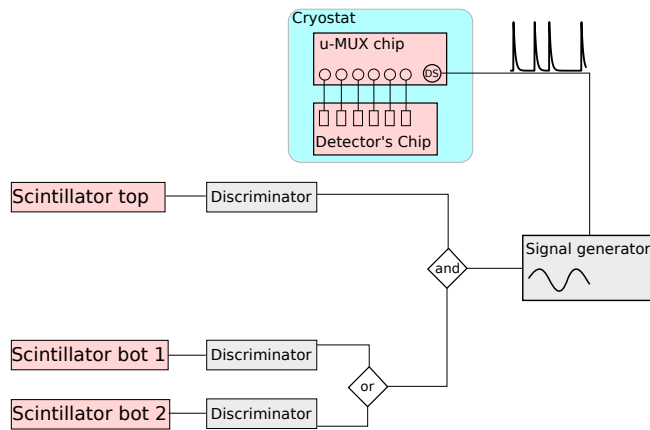


FIGURE 6.5: Scheme of the logic setup.

To solve this, we exploited the presence on the multiplexing chip of a squid which is not coupled to a detector, called the *dark squid* (DS). Its input was wire-bonded to one of the unused pad of the PCB on the detectors' holder, in order to send a custom input signal from room temperature to the multiplexing chip. The logic signal from the scintillators' coincidence module was sent to a signal generator, which in turn produce an ad-hoc signal to the DS that can be triggered by our readout alongside the signals from the calorimeters. The coincidence between the dark squid and the microcalorimeters were performed offline, tagging each event that has a timestamp t satisfying

$$t - t_{DS} \leq t_{thr} \quad (6.2)$$

as a muon or muon-induced event. Given a microcalorimeter signal with a timestamp t , t_{DS} is the timestamp of the closest event in the scintillators (DS) while t_{thr} is the threshold value, which must be tuned to include the various delays in the electronic chain.

Regarding the detectors, the array chip *HolmesKOH Au* (section 5.1) was used, made of 32 TESs with different geometries. We couldn't use its twin chip, the one with the identical detectors, because the molybdenum tracks transporting the bias were damaged.

The detectors and the read-out chips were enclosed in a gold-plated copper holder that we adopted in previous measurements with X-ray fluorescence sources, thus it features an entrance closed by an aluminum film 6 μm thick.

The μ -mux readout chip was an old one, used in many different measurements, and as a result of bad bonding and damaged resonances of the 32 detectors only 16 were measurable.

6.1.2 Detectors calibration

There were multiple factors that have led to a challenging calibration procedure for the whole array. First of all, these detectors were not previously characterized, secondly they had different geometries alongside unwanted variations in the thermal conductance to the bath, resulting in different energy response. Moreover, the switchable calibration source was not ready at that time and no statistically significant peaks are expected in the energy interval that our detectors can cover with their dynamic range, from 0 to 10 keV.

To solve this daunting problem, it was necessary to make several approximations. I assumed that the microcalorimeter can be modelled as a single body connected to the thermal bath by one thermal conductance. Therefore, its thermal response to an energy deposition $E = \int P(t)dt$ is described by

$$C \frac{dT}{dt} = P_J - P_{bath} + P \quad (6.3)$$

as explained in section 3.1.1. Integrating the previous equation, I obtained the energy deposited in the absorber E as a function of the joule power P_J and the power flowing from the TES to the thermal bath P_{bath} .

$$E = \int P_{bath}(t)dt + \int P_J(t)dt \quad (6.4)$$

P_J can be obtained by integration of the differential equation describing the electrical circuit

$$P_J(t) = I(t)^2 R_{TES} \simeq (R_0 + R_L)I(t)^2 - R_L I(t)^2 \quad (6.5)$$

The signal $I(t)$ can be obtained from the measured signal $s(t)$

$$I(t) = -1 \times k_{\phi_0/A} \times s(t) + I_0 \quad (6.6)$$

where $k_{\phi_0/A}$ is the known conversion factor from Φ_0 to Ampere, while I_0 and R_0 are the idle values of current and the resistance, which can be measured for each detector from their characteristic I-V curves, R_L is the known value of the load resistances common for all the detectors.

On the other hand, $P_{bath}(t)$ can't be measured because it requires the knowledge of the temperature variation of the detectors. I approximate its value by assuming that it doesn't vary significantly during the energy deposition.

$$P_{bath}(t) \simeq P_{bath,0} = R_0 I_0^2 = \text{const} \quad (6.7)$$

In summary, with just the I-V curves from the measured signals $s(t)$ it's possible to evaluate a parameter E^* which is a good estimate of the true energy E released. The approximation holds for the low energy events, while for the higher energy events E^* is an underestimation of E , as shown in Figure 6.6

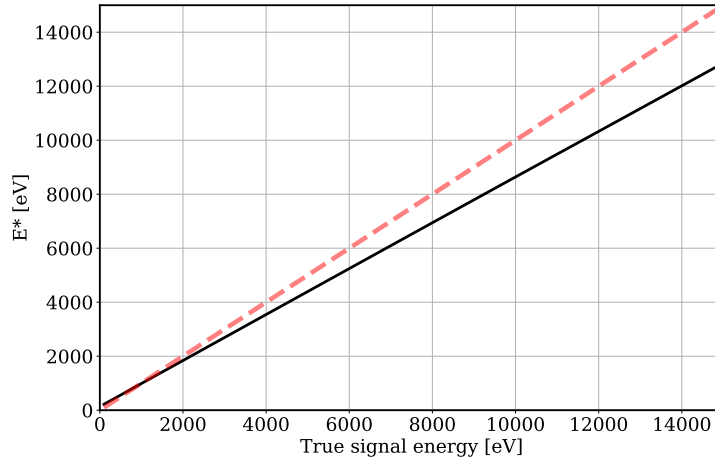


FIGURE 6.6: Trend of the E^* parameter (black line) compared to the true simulated energy E . E^* was evaluated using simulated pulses given an energy E . The red dotted line represents the case in which $E^* = E$. The higher the energy the larger the error.

$$\begin{aligned}
 E \simeq E^* &= \int_{t_0}^{t_f} R_0 I_0^2 dt - \int_{t_0}^{t_f} R_0 I(t)^2 dt \\
 &= R_0 I_0^2 \times (t_f - t_0) - \int_{t_0}^{t_f} R_0 I(t)^2 dt
 \end{aligned} \tag{6.8}$$

To partially fix the under evaluation of E due to eq 6.8, I defined a new parameter E_{cor}^* as

$$E_{cor}^* = p_1 + p_2 E^* + p_3 (E^*)^2 \tag{6.9}$$

where p_i are coefficients evaluated from a linear regression using the simulated signals of one of the detectors in the array.

To test the goodness of this rough calibration procedure, I compared E^* and E_{cor}^* to E^{cal} of an old 'true' calibrated measurement, where E^{cal} was the energy obtained after the calibration procedure described in section 4.3.4 using X-ray fluorescence sources. The errors

E^{cal} [eV]	E^* [eV]	E_{cor}^*
1455	1300 ± 260	1369 ± 273
3653	2930 ± 586	3278 ± 655
5898	4635 ± 927	5278 ± 1055

TABLE 6.1: Comparison between the 'true' measured signal energy (E_{cal}) and the energy estimated using this calibration procedure. The signals have been randomly taken from a measured dataset (run 60, measurement 3, detector channel 7)

are an estimation that take into account an uncertainty on the value of R_0 and I_0 of 10 % due to the temperature drift of the bath.

We can conclude that the calibration procedure described in this section can not be used to a precise energy determination of the signals, but it can be used for an estimation of the number of events inside a sufficiently wide energy interval, fitting perfectly the first goal of this measurement: the evaluation of the background rate.

6.1.3 The coincidences problem

During the offline analysis I noticed that with a t_{thr} value for the coincidence below the length of the recorded window (3 ms), the scintillators' channel had coincidence events with itself. In principle, this should not be possible, because with our read-out system the shortest time interval between two recorded events is the length of the window. Unfortunately, a problem with the timestamp allocation was later confirmed by a dedicated measurement, in which 1000 signals with a fixed time delay of 10 ms were sent by the external signal generator to the DS in the μ -MUX chip. The difference δt between the recorded time intervals and the expected one is shown in Figure 6.7.

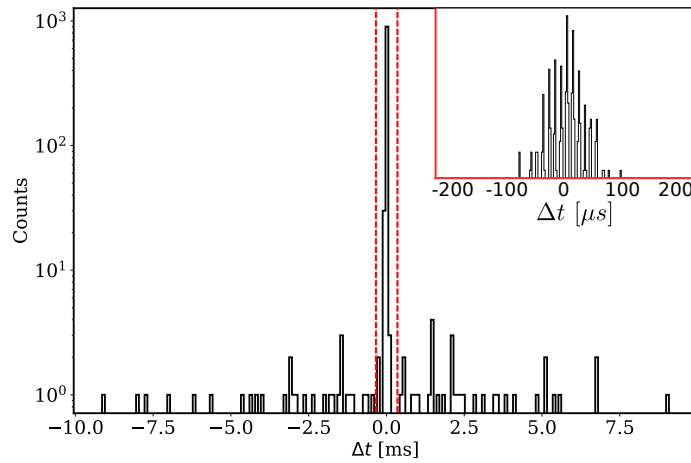


FIGURE 6.7: Distribution of the measured signals delays. The zero indicates the expected delay of 10 ms.

The most probable hypothesis is that our current acquisition system affixes a wrong timestamp with a probability of at least 10%. The wrong timestamp can differ from the true one up to tens of thousand of microseconds.

We are currently working to fix this problem, which is probably related to the default priority that the server gives to each process. Meanwhile, two threshold values were used to acquire the TES-TES and TES-scintillators coincidences.

For the former, a value of $t_{thr} = 65$ ms was selected as the value in which the measured coincidence rate reached a plateau. The expected rate for fake-coincidence was evaluated as the ratio between the mean value of a binomial distribution and the total number of events

$$r_{fake} = \frac{n_{tot} \times P_{fake}}{n_{tot}} = P_{fake} = 16 \times [1 - P_{poisson}(0|A_{bkg}t_{thr})] \quad (6.10)$$

and, as shown in Figure 6.8, this value is negligible even with such a large t_{thr} because of the low background activity.

On the other hand, the TES-scintillators coincidences rate is soon dominated by the fake-coincidence due to the scintillators activity of 7 Hz. Thus, we are forced to sacrifice efficiency for reliability and setting the $t_{thr} = 2$ ms.

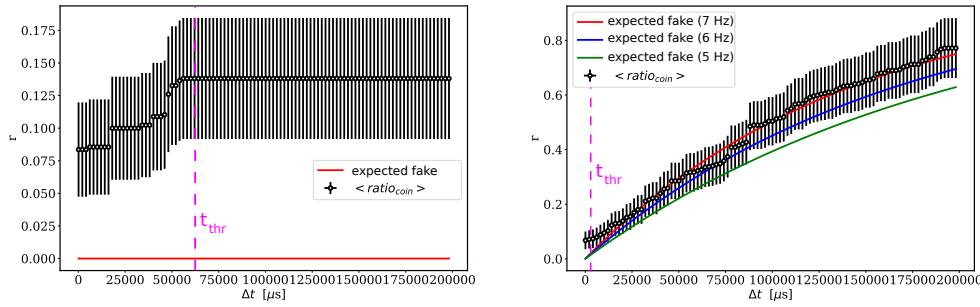


FIGURE 6.8: *Left*: The ratio between the number of TES-TES coincidences and the total number of events r_{coin} vs t_{thr} (indicated as Δt). The red line represents the expected number of fake coincidences, which is negligible. The value of t_{thr} for which r_{coin} reaches a plateau is the correct value. *Right*: Same plot, but for the TES-scintillator coincidences. In this case r_{coin} never reaches a plateau, instead for longer t_{thr} the fake coincidence dominates, as expected for an activity of 7 Hz.

6.1.4 About the data analysis

The data analysis described in this section was performed within a Bayesian framework. Because I think that for many of the readers, myself included, the Bayes theorem was just mentioned during their studies, it is worth dwelling on the subject to avoid confusion later on.

The so-called Bayesian methods are being employed in the most disparate fields of research and application, and I have the feeling that it is gaining ground also in physics. Some people are calling it a 'paradigm shift', although, as D'Agostini pointed out [88], it is a strange revolution indeed which has its roots in the centuries-old ideas of the founding fathers of probability, the likes of Bernoulli, Bayes, Laplace and Gauss.

Usually, to facilitate the understanding of the topic, it is introduced by pointing out the main difference between the bayesian method and the frequentist one, that is the definition of probability like a 'degree of believe' rather than a relative frequency of events. What seems like an abstract and philosophical matter has a profound impact on the respective theories and on the interpretation of their results.

I will focus mainly on the parameter estimation, because as physicist this is the main application. For a bayesian, a parameter is an unknown value, and the best way to represent our knowledge on the parameter after a measurement has been performed is to give the probability that the parameter lies inside a limited range of value, i.e. to give the probability distribution of the parameter. This process is called evaluating the posterior $P(\theta|\vec{x})$ and relies on the fundamental Bayes theorem

$$P(\theta|\vec{x}) \propto \mathcal{L}(\vec{x}|\theta)P(\theta) \quad (6.11)$$

where $\mathcal{L}(\vec{x}|\theta)$ is the probability that given the parameter θ the data \vec{x} were observed, called the likelihood, while $P(\theta)$ is called the prior distribution and it summarize our previous knowledge on the parameter θ .

A number is more human-readable than a plot. With this approach, one can arbitrarily choose how to summarize the posterior distribution (mean, confidence intervals, standard deviation...) as long as the choice is made explicit to the reader. The advantages of the bayesian approach are numerous, from the clean and easier interpretation of the results to a more natural analysis of what is called the systematic uncertainties. It has many

times pointed out that dependence of the posterior on the prior is the disadvantage of this method. An exhaustive answer on the matter can be found in [88], I just wanted to pointed out that there is no shame in admitting that a scientific result is always subjective at some degree. What matters most is that the prior choice is made explicit and not hidden inside a principle, so that it can be critically analyzed. Also, as more data are collected, the likelihood shrinks more and more and the dependence on the prior gets weaker.

The true disadvantage lies on the computational complexity of eq (6.11). Nowadays, many method based on different versions of the Marckov Chain Monte Carlo (MCMC) algorithm allow us to compute the posterior ¹ in a robust way. For the Holmes application, I decided to use STAN [89] which uses a modified version of the Hamiltonian MCMC to coherently explore the parameters space of the posterior, which should be more efficient in high dimensional problems such as the neutrino mass estimation respect to other methods.

6.1.5 Expected bagkround rate

To evaluate the expected background rate nine separate measurements were performed, lasting for a total of 20 days. The signals were tagged as singles interactions, TES-TES or TES-scintillator coincidences, following a similar procedure to the one explained in section 6.1.3. Then a calibration was performed using the detectors' characteristic I-V curves, merging the data from each detectors to produce three different spectrum for each tag.

To estimate the expected background rate in each energy interval, the posterior probability for the rate parameter was evaluated iteratively, using a Poisson distribution as likelihood given x_j counts in the j -detector and a flat distribution as prior. Then, the probability for the background rate was updated using the resulting posterior as prior for the probability distribution of the rate for the $(j + 1)$ -th detector.

The resulting distribution for the rate r in the i -th bin is a gamma distribution

$$P(r|N, c) \propto r^c e^{-cN}$$

$$c = \sum_{j=1}^N x_j \quad (6.12)$$

with N the number of detectors and x_j the counts of the j -th detector for that bin.

The data points in the rate plots represent the expected background rate in each bin expressed as the mean value of the gamma distribution while the error bars are the 95% credibility interval evaluated symmetrically from the median. If a bin has zero counts, the error represents the 95% upper limit.

The TES-TES background spectrum is composed of radiation that directly hits multiple absorbers or that interacts with the materials between the pixels. The latter case is the most probable and the resulting signal is expected to have significant different shape compared to the direct interaction due to the different thermalization process of the TES thermometer, as shown in Figure 6.9. Thus, they do not contribute to the final background rate, their energy spectrum is shown in Figure 6.9.

Singles interactions produce a background spectrum as shown in Figure 6.12. Between 0 and 10 keV it seems to be monotonically decreasing² although the calibration procedure does not allow us to exclude the presence of low energy peaks. The background rate near the end-point of the spectrum is measured to be of the order of 0.5×10^{-3} counts $\text{eV}^{-1} \text{day}^{-1} \text{det}^{-1}$.

¹Strictly speaking, to sample from the typical set of the parameter

²the low energy peak is due to the trigger that fails to distinguish between low energy signals and noise

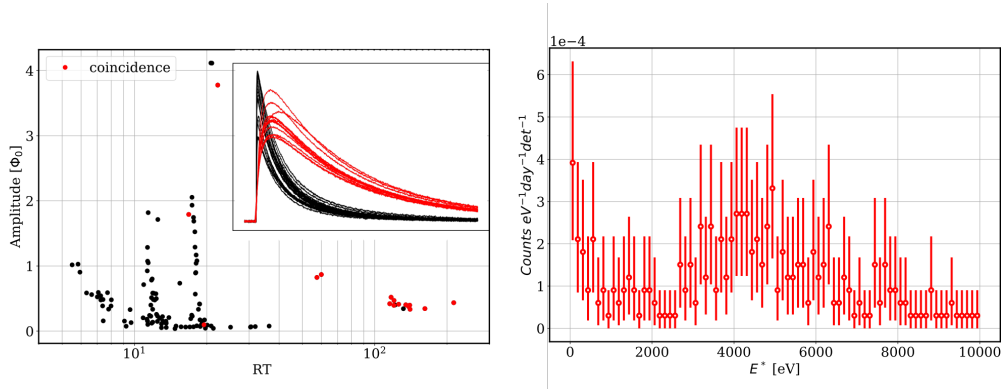


FIGURE 6.9: *Left*: example of the distribution of the signals amplitude respect to their rise time (RT). The signals tagged as TES-TES coincidences are shown in red. *Right*: The TES-TES coincidence energy spectrum.

However, it is reasonable to believe that a great fraction of the events in the single interactions dataset are radiations which does not interact directly with the absorber but with the detector surroundings, the copper perimeter or the thermometer itself. As in the TES-TES case, these interactions should produce signals with different shape that can be easily recognized with the first and the second data reduction procedures.

The expected efficiency of these techniques can be seen in Figure 6.11, where the distribution of the rise time (RT) in one of the measured detectors is shown while the pink bands represents RT spread for detectors measured previously with an external calibration source. It can be clearly seen that it does not matter where pink band should actually be for the considered detector, as most of the events will be outside this narrow band and it will be discarded by the first level data reduction.

To quantify the efficiency of these techniques the exact location of this band should be known, but without an external calibration source this seems impossible at first glance.

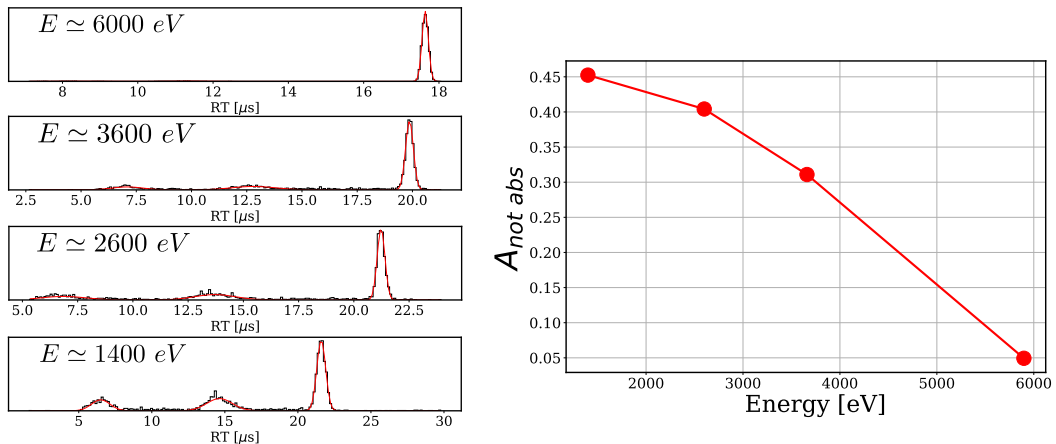


FIGURE 6.10: *Left*: example of the RT distribution at different energies intervals with an external calibration sources (Run 60). *Right*: the normalized area of the low RT peaks $A_{not\ abs}$ at different energies. As you can see, above 6 keV only the 5% of the signals presents a lower value of RT.

However, in previous measurements with the same array it was observed that signals from external X-ray sources show a RT distribution that can be modeled as a sum of gaussians with different means and intensities, as shown in Figure 6.10. The difference in the relative intensity of the gaussians seems to decrease as the energy decrease and for energy above 6

keV just one peak is present. I believe that the signals in the low intensity peaks (smaller values of RT) are radiations which interact directly with the thermometer, resulting in faster RT, and the trend of the peaks' intensity is motivated by the different attenuation lengths and dimensions in the absorber and in the thermometers.

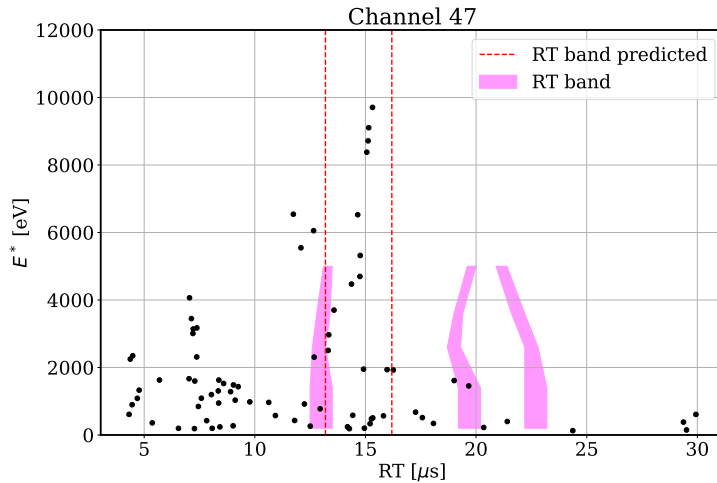


FIGURE 6.11: Distribution of the signals energy respect to their rise time for the TES pixel 47. The pink bands are an example of the RT distribution from three different detectors for radiations that interact directly with the absorber (bulk interactions). The red dotted lines represent the region in which the bulk interaction are expected.

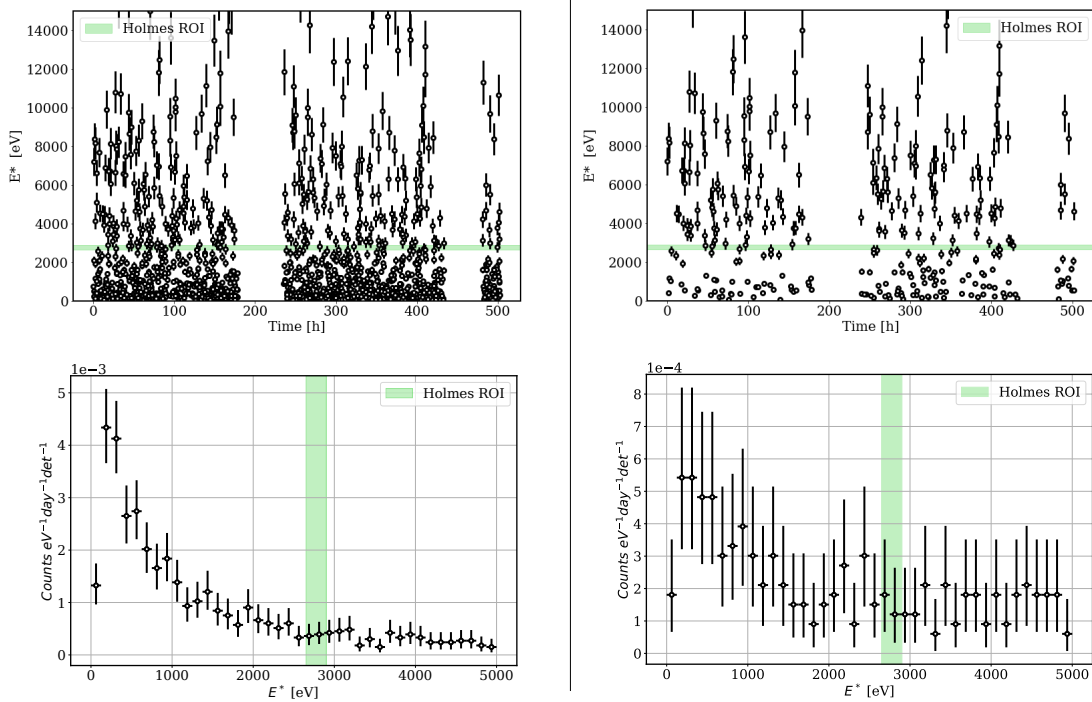


FIGURE 6.12: *Left:* (top) distribution of the signals energies in time for the singles interactions for all the detectors. (bot) the resulting background energy spectrum. *Right:* the same plots, but with only the bulk interactions.

Thus, the location of the RT band for the interactions in the absorber, i.e. for true Ho decays, can be found by looking at the RT of the high energy events ($E > 6$ keV) while the width of the band was conservatively defined as $3 \mu\text{s}$, three times the expected one.

Thus, a similar cut as the one shown in Figure 6.11 was applied to each detector, which results in the expected background spectrum presented in Figure 6.12, presenting a background rate in the ROI 1×10^{-4} counts $\text{eV}^{-1} \text{day}^{-1} \text{det}^{-1}$, five times lower than the one without data reduction.

6.1.6 Muon induced background

The TES-scintillator coincidences spectrum would have been a useful tool to study the muon induced background rate. However, because of the timestamp problem the efficiency of the tag was too low and only 11 events out of a total of ~ 1500 were recognized as muon-induced. To estimate the fraction of the background rate that is muon induced f_μ , I had to follow a different procedure based on MonteCarlo simulations, that just allow me to have an idea of its order of magnitude.

I divided the data in equal time intervals lasting 5 hours. In each interval, the total counts recorded by the detector array c_i follow a Poisson distribution

$$c_i = \text{Poisson}(c_i | N_i^\mu + N^b) \quad (6.13)$$

where N_i^μ is the mean number of muon induced events and N^b is the mean number events due to the natural radioactivity. The latter is assumed to be constant while N_i^μ in principle can vary during the measurement due to changes in atmospheric temperature and pressure above the laboratory.

The number of muon induced events in the array can be evaluated from the scintillators counts N_i^s using MC simulations and some approximation to estimate the various geometrical efficiency. Calling $P(A)$ the probability that a muon induced events hits the array while $P(B)$ the probability that it hits the top and bottom plane of the scintillators

$$N_i^\mu = k \times N_i^s \quad (6.14)$$

$$\begin{aligned} k &= P(A|B) = P(B|A) \frac{P(A)}{P(B)} \\ &\simeq 0.5 \frac{2.97 \times 10^{-5}}{0.86} = 1.75 \times 10^{-5} \end{aligned} \quad (6.15)$$

$P(B|A)$ and $P(B)$ are evaluated measuring the distance between the detector box and the scintillators d_{bs} and between the two scintillators plane d_{ss} respectively and approximating the scintillators slabs as circle of radius $r_{top,bot}$ with equivalent area (see Figure 6.4)

$$P(B|A) = \frac{\int_0^\alpha \cos(\theta)^2 d\theta}{\int_0^{\pi/2} \cos(\theta)^2 d\theta} ; \alpha = \arctan r_{top}/d_{bs} \quad (6.16)$$

$$P(B) = \frac{\int_0^\beta \cos(\theta)^2 d\theta}{\int_0^{\pi/2} \cos(\theta)^2 d\theta} ; \beta = \arctan r_{bot}/d_{ss} \quad (6.17)$$

$P(A)$ was evaluated from MC simulations in which 100 millions muons were generated above the detector box from an area approximately infinite, but only $\sim 18 \times 10^3$ interactions were recorded in the array composed of a matrix of 10×10 detectors.

From N^b , the posterior for f_μ was extracted, using for the prior of k a gamma distribution centered in (6.15) limited in a plausible interval of values and defining f_μ as

$$f_\mu = \langle f_\mu \rangle = 1 - \frac{N \times N^b}{\sum_i i^N c_i} \quad (6.18)$$

The fraction of muon induced events was measured having a mean value of $E[f_\mu] = 0.460 \pm 0.002$, with a plausible interval of 90% between [0.28,0.59].

6.1.7 ^{40}K and neutrino mass sensitivity

^{40}K is the only natural occurring unstable potassium isotope, having a half-life of 1.3×10^9 years. It decays via beta decay (branching ratio $\sim 90\%$) to ^{40}Ca or via electron capture (BR $\sim 10\%$) to an atomic and nuclear excited state of ^{40}Ar , which in turn relaxes emitting X-rays, auger electron and the characteristic gamma of 1460 keV (Figure 6.13).

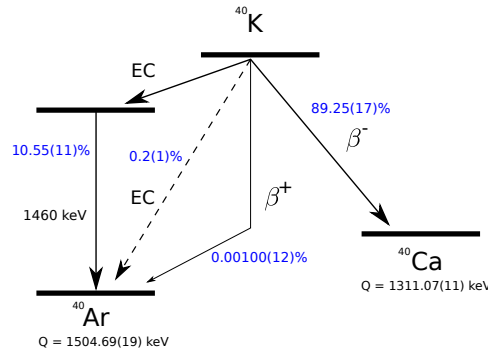


FIGURE 6.13: Scheme of the ^{40}K decay.

Both the gamma and the electron from beta decay produce a flat spectrum in the ROI region, while the EC produces de-excitation peaks with energy into and close to the ROI. If those peaks are present but not modeled in the final spectrum, they could potentially worsen the experimental sensitivity.

To have a preliminary idea of how severe this effect could be, I have studied qualitatively how the posterior of the neutrino mass changed if the likelihood did not include the ^{40}K peaks by varying the number of counts B under those peaks.

I fixed the number of detectors N_{det} to 32, the energy resolution to 5 eV, the time resolution τ_R to 1.5 μs , the measurement time T_{meas} to 3 years and I generated multiple toy ROI spectrum $S(E)$

$$\begin{aligned} S_{true}(E) &= S(E) + B \times m_{peaks}(E) \\ S(E) &= Ho(E) + f_{pp} \times (Ho * Ho)(E) + bkg(E) \\ Ho(E) &\propto \left(\sum_i I_i \times \text{cauchy}(E, x_{c,i}, \gamma_i) \right) \times \left((Q - E) \times \sqrt{(Q - E)^2 - m_\nu^2} \right) \end{aligned} \quad (6.19)$$

with $Ho(E)$ being the de-excitation ^{163}Ho spectrum³, f_{pp} is the ratio of pile-up pulses to single pulses, which can be approximated⁴ from the single detector activity A as $f_{pp} = A \times \tau_R$, $bkg(E)$ is the flat background and $m_{peaks}(E)$ are the de-excitations peaks due to the

³Second order effects like shake-up and shake-off 2.2 have not been considered

⁴For simplicity, I will also assume that in the dataset pulses having a second pulse on their tails are not present

EC of ^{40}K . The total number of generated events n_{ev} for $S(E)$ is given by the ^{163}Ho activity per pixel A , $n_{ev} = T_{meas}AN_{det}$, while the total number of single pulse n_s and pile-up pulses n_p are given by

$$n_s = \frac{n_{ev}}{1 + 2f_{pp}} \quad (6.20)$$

$$n_p = n_s f_{pp} \quad (6.21)$$

The ROI region was defined as $E \in [2650, 2900]$ eV and the background activity for the $bkg(E)$ spectrum was fixed at 1×10^{-5} counts $\text{eV}^{-1} \text{day}^{-1} \text{det}^{-1}$, five times lower than the one measured in the previous section. For each value of B , $\mathcal{O}(10)$ different spectra were generated, following 6.19. The parameter estimation on m_ν , Q , f_{pp} , n_{single} and bkg was performed with STAN, choosing as likelihood

$$\begin{aligned} \mathcal{L} &= \text{Poisson}(c_i | \lambda_i) \\ \lambda_i &= n_{single} \times \left(S * \text{normal}(0, 5/2.355) \right) (E_i) \end{aligned} \quad (6.22)$$

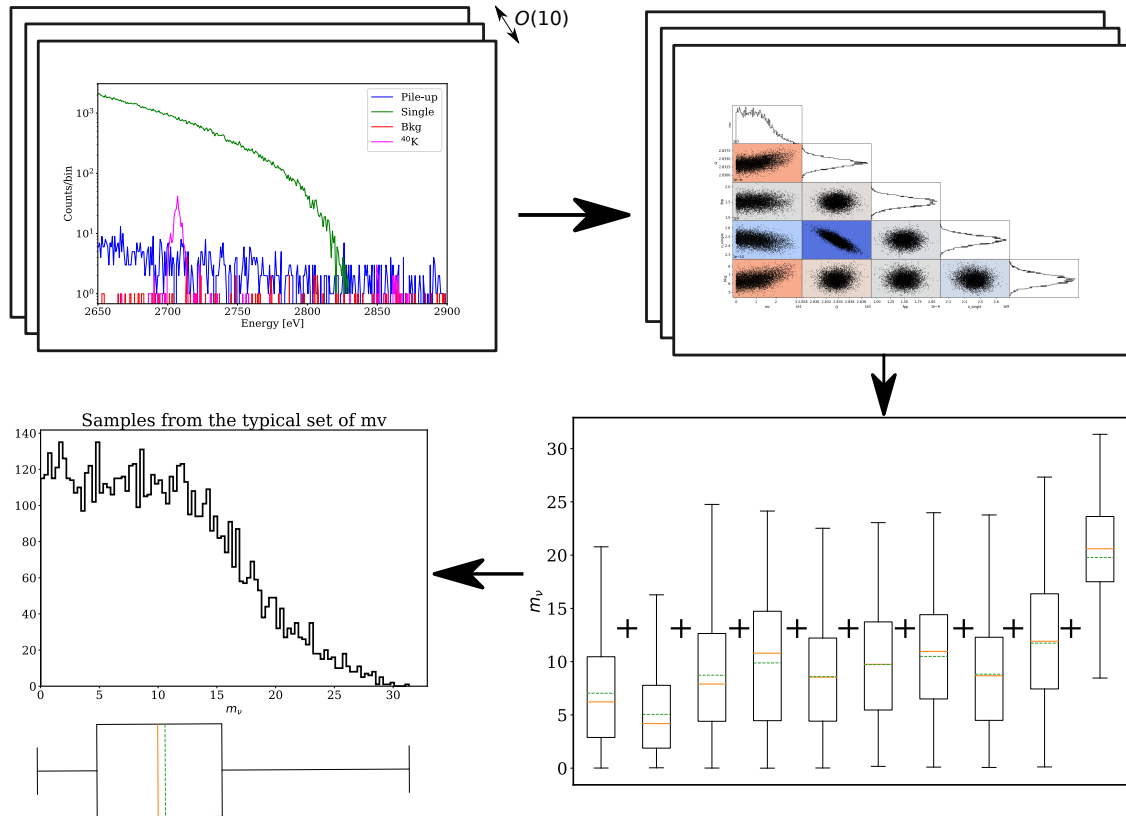


FIGURE 6.14: Scheme of the simulations: first for a fixed value of B different spectra are generated, then a parameters estimation is performed with STAN for each spectrum. The samples generated from the m_ν posteriors are merged to reduce the statistical fluctuations and the resulting distribution is shown as a boxplot.

and a normal priors for Q , f_{pp} , bkg and n_{single} , while for m_ν an exponential distribution with a slightly uninformative rate parameter of 0.01.

The samples generated from each Markov Chain Monte Carlo were merged to reduce the influence of the statistical fluctuation of each bin on the parameters posterior and the

resulting distribution of the “mean typical set” was summarized in a boxplot. The scheme for the followed procedure is depicted in Figure 6.14, while Figure 6.15 shows the final result for a single pixel activity of 1 Bq.

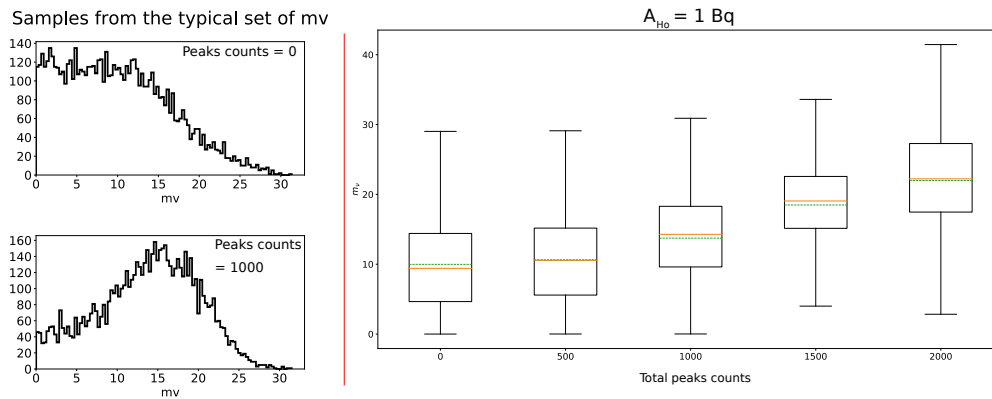


FIGURE 6.15: The distribution of the samples from the m_ν posteriors are shown with the variations the total number of ^{40}K decays (total peak counts), the B parameter. The boxplot lines approximately represents the 90% credible intervals, the orange (green) line the median (mean) of the distribution while inside the box there are 50% of the total entries.

It is reasonable to assume that the only place from which the de-excitations product of ^{40}K can reach the detectors are the internal cover of the detector’s holder and the surface of the gold absorbers, although the latter seems unlikely due to our fabrications procedures. Therefore, we used the MC simulations to convert B from total counts under the peaks to a surface density of K on the holder’s cover.

From that, we can conclude that with this configuration a surface contamination of 0.5 mg/cm^2 of K (corresponding to a number of counts under the ^{40}K peaks of ~ 1000) starts to affect the posterior distribution of m_ν and worsen the experimental sensitivity.

6.1.8 Conclusion

Studying the influence of ^{40}K on the neutrino mass I simulated the condition in which this effect should be more noticeable, i.e. with the lowest target pixel activity of Holmes. Even with this setup, the amount of potassium required to produce a measurable effect on the final spectrum is quite large, and we can preliminary conclude that the influence of ^{40}K on the experimental sensitivity will be negligible and that the shape of the expected background in the ROI will be smooth or approximately flat.

I measured a background rate in the ROI of $0.5 \text{ counts eV}^{-1} \text{ day}^{-1} \text{ det}^{-1}$, but I proved that with a rough first level data reduction this rate can be reduced by a factor of 5 to $1 \times 10^{-4} \text{ counts eV}^{-1} \text{ day}^{-1} \text{ det}^{-1}$. We believed that it can be further reduced by at least a factor two by using a more tight RT cuts in combination with second level data reduction techniques.

The comparison between the background rate due to natural radioactivity and cosmic rays to the pile-up rate allow us to establish that the former is dominant in the hypothesis of an ^{163}Ho activity of 1 Bq per detector (Figure 6.16 (A)), while it becomes negligible compared to the pile-up above an activity of 50 Bq. The two have nearly the same magnitude at 10 Bq.

Due to the fact that the muon contribution to the final background rate is about the same order of magnitude as the natural one it can not be neglected. A further reduction on the total background rate of a factor of roughly 25% can be achieved by realizing an active

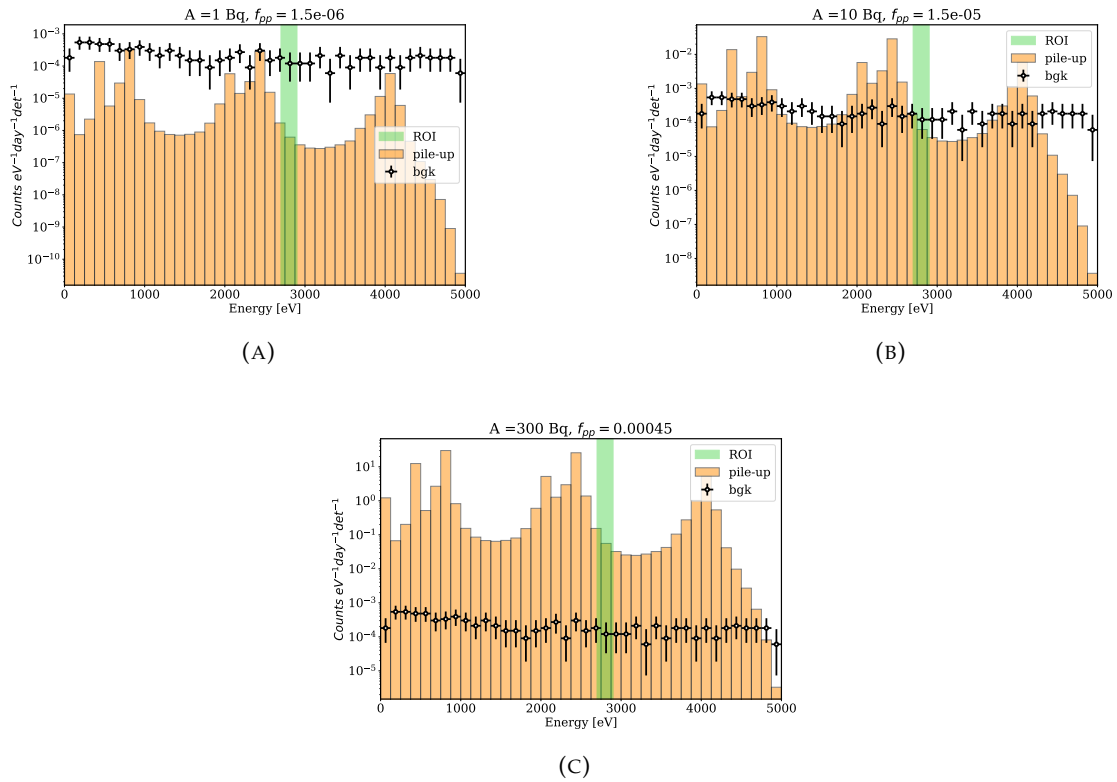


FIGURE 6.16: A comparison between the expected pile-up spectrum and the measured background for different single pixel activity A . The green region represent the Holmes region of interest.

muon veto similar to the one tested in this section, enhancing the experimental sensitivity in the first phase of the Holmes experiment.

6.2 Pile-up rejection

As already explained in section 2.3, the pile-up will be the main background source for Holmes. In fact, simulations have shown that the sensitivity on neutrino mass is not strongly dependent on the energy resolution of the detector (as long as $\Delta E < 10$ eV), but rather on the pile-up fraction f_{pp} which is defined as the ratio between the number of pile-up events to single events.

f_{pp} is proportional to the time resolution τ_R , as you can see from 6.24, i.e. the arrival time difference of two events below which they are misinterpreted as a single event with energy equal to the sum of the two. This in turn depends on the detectors and readout characteristics, such as the sampling time. Still, once fixed the detector response and the sampling frequency, τ_R depends on the algorithms used to discriminate the signals.

The latter must meet, other than a high efficiency, the very strict requirement of near zero energy dependence. This is imposed by simulations similar to the ones described in [50], which have shown that even a small fraction of false negative modifies the single events spectrum and leads to a systematic error on the neutrino mass evaluation.

With this goal in mind, I have studied an application of the Wiener Filter while developing a new discrimination technique called DSVP, as I described in 4.4. In this section these algorithms are applied in the framework of Holmes. The terminology that will be

used is the same as as the one of section 4.4.3 and in this context an A event is a signal caused by a single energy deposition in the microcalorimeter detector, while a B event is a signal caused by nearly coincident events. Each signal is a collection of records I_i of the current flowing through the detector sampled at an instant $t_i = i \times t_{samp}$, where t_{samp} is the sampling time of the readout system.

I tested their robustness and efficiency through many simulations which aim at emulating the results expected by the HOLMES experiment. The HOLMES TES microcalorimeters do not have the ^{163}Ho implanted yet, therefore a real data test will be done at later times.

6.2.1 Simulations

For this study I modeled three different TES microcalorimeters with the one-body model or with the two-body dangling model. In both cases the current pulse profile is obtained by solving the system of the electro-thermal differential equations (3.3), (3.40) applying the fourth-order Runge-Kutta method (RK4) and considering the transition resistance as proposed by [61] for taking into account the TES non-linear behavior

$$R_{TES}(T, I) = \frac{R_N}{2} \left[1 + \tanh \left(\frac{T - T_C + (I/A)^{2/3}}{2 \log(2) T_W} \right) \right] \quad (6.23)$$

with A and T_W given by the known α and β and the idle conditions.

To these pulses a noise waveform, generated as an autoregressive moving average ARMA (p,q) process with a power spectrum given by the Irwin-Hilton model, is added. To test

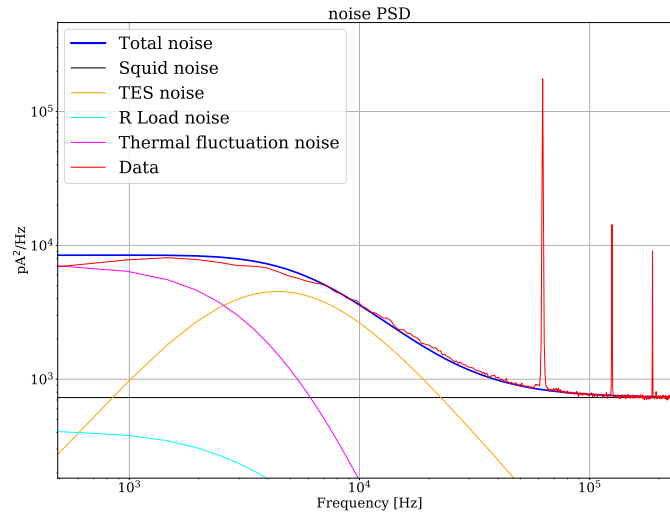


FIGURE 6.17: Simulated noise power spectrum for TES 8 of Run 37, measurement 14 (*holmesDRIE*) compared with the acquired data.

the algorithms effectiveness with slightly different signal shapes, the physical parameters in the differential equations are chosen to describe three types of detectors:

- the detectors in [90], which are characterized by a non linear response and one thermal body.
- the target detectors of HOLMES [64] (*holmesDRIE*) which have nearly linear response and behave according to a two thermal body model.

- c. same nominal design as b. except for the production process, causing a significantly weaker link toward the thermal bath (*holmesKOH Au*). Thus, the signals have a slower decay time and a lower signal amplitude respect to b. Despite this difference, the detectors show a linear response to energy deposition with a two-body feature.

The goal was to replicate the measured signals as close as possible, and Figure 6.18 shows the comparison between the simulated pulses with the measured one for the detector of type b.

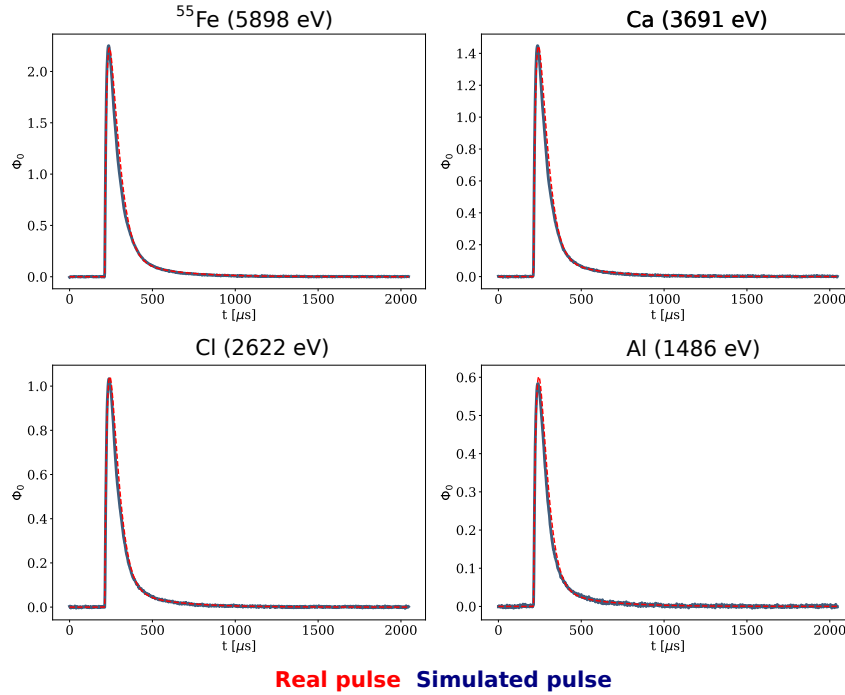


FIGURE 6.18: Simulated signals compared with acquired data.

The detectors of type b., with their fast response time and excellent energy resolution, are the most promising for the HOLMES goals. Therefore, for this detector three different configurations were tested, in which the rise time was changed, adjusting the inductance of the circuit and keeping the other detector parameters constant. Table ?? summarizes the parameters of the TESs used in these simulations.

Both the algorithms need a dataset in which the number of single pulses is greater than the number of pile-up pulses. This was indicated in 4.4.3 as training region \vec{T} for the DSVP and the region in which to define the average signal for the Wiener Filter. In the case of Holmes, the idea is to use the events at the M1 peak ($E \sim 2$ keV) because it is the peak closest to the ROI, thus reducing the non-linearity effects on the algorithms and because the f_{pp} in this range is expected to be of the order of $\sim 10^{-3}$, which can be further reduced with a *raw cleaning with PCA*, as described in section 4.4.3.

To simulate a pseudo-real dataset useful for this goal, I simulate the energies according to the spectrum (2.4) and create the resulting signals expected with a 300 Hz activity and acquired with our acquisition system. For example, in a dataset for detector of type b. the ~ 700000 signals were divided in single pulses (61%), double pulses (31%), triple pulses (6%) and quadruple pulses (2%). This is the expected dataset recorded in one hour with one detector.

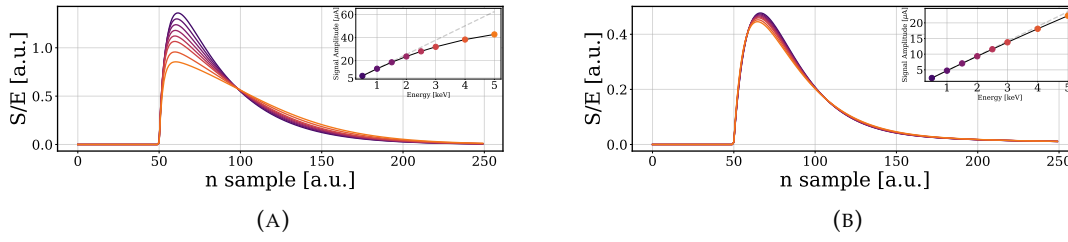


FIGURE 6.19: Pulse profiles corresponding to different energies from 0.5 to 5 keV for two different detectors with non-linear (det. [a]), and nearly-linear response (det. [b]). In order to compare the signals, all the pulses are normalized by dividing their amplitude by the energy.

It is also necessary to simulate a different dataset in which the effective time resolution is evaluated, i.e. a dataset containing the events in the ROI, which has been considered, in this context, to be the region between 2650 and 2900 eV. The expected f_{pp} in this region can be calculated as the ratio of the probability to find a pile-up pulse c_p to the probability of a single pulse c_s

$$f_{pp} = \frac{c_p}{c_s}$$

$$c_p = \text{Poisson}(1|\lambda_p) \times \int_{2650}^{2900} (Ho * Ho)(E)dE \quad (6.24)$$

$$c_s = \text{Poisson}(0|\lambda_s) \times \int_{2650}^{2900} Ho(E)dE$$

with $\lambda_{p,s}$ given by

$$\begin{aligned} \lambda_p &= A \times \tau_R \\ \lambda_s &= A \times w_l \end{aligned} \quad (6.25)$$

where A is the detector activity, τ_R is the time resolution and w_l is the length of the recorded window. Assuming that a time resolution of 10 μs can be achieved with the first level data reduction, the f_{pp} in the ROI was initially fixed at 2 while 40000 (\sim 80000) single (double) pulse events were generated, simulating the statistic expected for a single detector with an activity of 300 Hz over two years of data taking. The arrival time of the pile-up pulses is uniformly distributed between 0 and 10 μs .

6.2.2 DSVP and Holmes

In order to apply the DSVP algorithm, the \vec{M} matrix, which contains the ROI events, must have $N_A > N_B$, thus f_{pp}^{ROI} needs to be lowered below one.

To reduce this ratio many different strategies can be adopted. In the following a non exhaustive list is reported.

- *Adding an additional calibration source.* By adding a source characterized by a monochromatic X-ray emission in the ROI, the number of single pulses in the ROI can be increased while keeping the number of pile-up pulses unchanged. This approach can be very useful because it reshapes the energy spectrum, potentially reducing the probability of discarding single events with energy very close to the end-point. A similar approach was investigated by Alpert et al. [90].

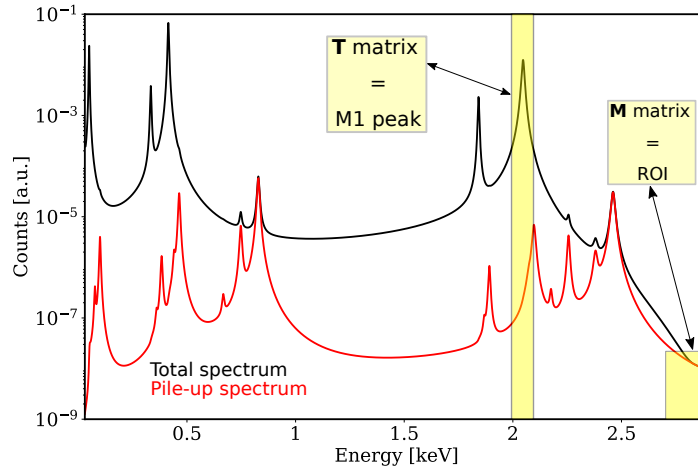


FIGURE 6.20: De-excitation simulated spectra of ^{163}Ho with $f_{pp}^{tot} = 3 \times 10^{-3}$. Near the end-point the single pulse counts are outnumbered by pile-up counts.

	type a.	type b.	type c.
n	3.25	2.25	3
n_d	-	2	3
C [pJ/K]	0.5	0.8	1.43
C_d [pJ/K]	-	0.25	0.3
G [pW/K]	406	700	450
G_d [pW/K]	-	1200	5500
α	200	100	100
β	2	2	2
T_C [K]	0.1	0.1	0.1
T_{bath} [K]	0.07	0.04	0.06
R_L [m Ω]	0.3	0.3	0.3
R_N [m Ω]	10	7.7	8
R_0 [m Ω]	2	1.4	1.41
L [nH]	48	30/50/60	55
w_l [sample]	250	1024	1024

TABLE 6.2: TES paramaters used in the simulations.

- *Volumetric cuts.* The events of the training dataset \vec{T} are distributed in a finite volume in the k -dimensional projection space. The single pulses in the ROI reasonably lie within the same portion of space, while the pile-up are expected to be distributed in a different region. Thus if we select only the points in the projection space lying inside the volume which includes the training dataset, we could easily eliminate a large fraction of pile-up events.

Before evaluating their projection on the \vec{T} right singular vectors, the \vec{T} and ROI events are normalized to set their amplitude equal to one. Then, we define the region in the k -space in which the \vec{T} events are distributed. We increase it by a little amount in order to account small non-linearity effects. Finally, we select only the events in

the ROI included inside this region. This method can achieve good time resolution, but it works only if the detector response does not depart from linearity too much, so in our simulation in detectors *b.*, *c.* but not *a.* .

- *Filtering.* Few filtering techniques allow to achieve effective time resolution close to the sampling time. Among these, a particular Wiener filter based algorithm, as described in 4.4.3, is probably the best technique to achieve this goal.

For the Holmes purposes, in order to fulfill the $N_A > N_B$ condition in the ROI the most suitable and practical method are the 'Wiener filter' and the 'volumetric cuts'. As indicated in Table 6.3, applying these algorithms to the ROI events, the f_{pp}^{ROI} can be reduced around 0.6. Most of our simulations are therefore aimed to test their applications. Nevertheless, in sec 6.2.4 the performance of the DSVP technique with an external calibration source is also shown.

To quantify the efficiency of the pile-up discrimination algorithms, we define an effective time resolution τ_{eff} as the ratio of the number of retained piled-up records to single-pulse records after the algorithm divided by the same ratio referred to raw data, times $10 \mu s$.

6.2.3 DSVP time resolution with Wiener Filter

The wiener filter transfer function is evaluated with a dataset containing roughly mono-energetic single pulses, i.e. the pulses from the M1 peak. Then, the Wiener filter is applied both to the M1 and to the ROI. Each event will be described by three values: the WF_w (the width of the delta function), WF_{pts} (the number of points which compose the delta) and the WF_{delay} (the time when the delta reaches its maximum).

The problem is that the region of these new parameters space that contains the M1 events, which are mostly single pulses, is not the same compared to the one that contains the single pulses in the ROI. Finding the boundary of this region is the same as finding the value of the WF_w that discriminates the most pile-up events in the ROI. As suggested by the simulations, WF_{delay} and WF_{pts} do not present a strong energy dependency and their boundary values do not change between the ROI and the M1.

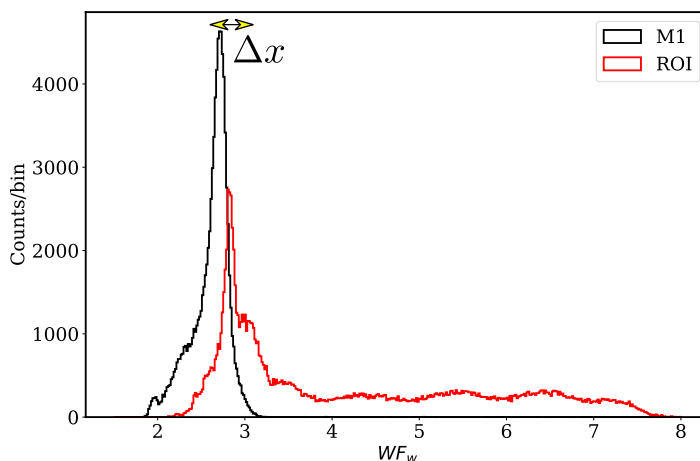


FIGURE 6.21: Distributions of the WF_w for the M1 (\simeq single pulses) and ROI events (single pulses + pile-ups). The maximum of the distribution of the single pulses is shifted of a quantity Δx from M1 to the ROI.

If we assume that the values of the WF_w of the single pulse in the ROI have a similar narrow distribution of the WF_w in the M1 but only a different mean value and that the pile-up pulses in the ROI present a broad distribution of the WF_w , we can find the new boundary by looking at the difference Δx of the maximum position of the distribution of the WF_w in the ROI and in the M1. Then, calling WF_w^{min} and WF_w^{max} the value that contains the M1 events, the values of the WF_w that discriminate between the pile-up pulses and the single pulses in the ROI are

$$WF_w^{min,max}(ROI) = WF_w^{min,max}(M1) + \Delta x \quad (6.26)$$

With this cuts we lowered the f_{pp}^{ROI} below one and, allowing us to finally apply the DSVP technique on the resulting dataset. Furthermore, before being processed by the DSVP algorithm, the signals were also whitened, i.e. their noise was transformed to whiten noise by a fast Cholesky-factor backsolve procedure [73].

The results are reported in Table 6.3. All the simulations showed that the DSVP is able to reach a time resolution lower than the sampling time of the signal. Table 6.3 shows that the time resolution is strongly dependent on the sampling time, the faster the better, but also on the rise time of the pulse. While the sampling frequency is constrained by the readout resources, there is more scope to change the rise time of the detectors, acting on the electrical time constant of the biasing circuit. Changing the rise time by a factor two may be achieved by reducing the inductance of the TES circuit by a similar factor. This change the noise spectrum too but usually it does not worsen the energy resolution. Also, the non-linear detector response generally improves the efficiency of pile-up recognition algorithms. When two near-coincident energy depositions happen inside the TES, the detector will have different starting conditions. The shape of the pile-up pulse will be much more different from the single pulse for a non-linear TES than for a linear one, thus allowing the algorithms to recognize them more efficiently. As we stressed in section 4.4.3, the only external parameter required by the DSVP algorithm is the number of events that it should discard at most, N_B . To quantify the influence of this parameter on the effectiveness of the algorithm, we fixed the dataset \vec{M} and varied N_B , computing the effective time resolution each time.

Figure 6.22 shows that no false positive was detected even if we get the number of event to eliminate wrong up to 50%.

We note that in our simulations no single pulse event was mistaken as pile-up. The DSVP technique described is designed to leave unaffected the A events.

6.2.4 DSVP time resolution with an external calibration source

We have also tested if the performance of the DSVP technique remains unchanged reducing the f_{pp}^{ROI} by adding an external source of single events with energy inside the region of interest instead of using preliminary filters. We added a source from $L\alpha$ x-ray emission lines of Pd (2.833, 2.839 keV).

Figure 6.23 shows that increasing the number of photons of the Pd source (thus decreasing f_{pp}^{ROI}) the effective time resolution of the DSVP improves. Moreover, τ_{eff} always remains below the sampling time even for a pile-up fraction up to 0.9.

To sum up, the DSVP algorithm, in combination with a Wiener Filter or an external calibration source, represents a very powerful technique to decrease the number of pile-up events in the ROI.

With the target detector of HOLMES, the DSVP techniques allows us to reduce the total fraction of pile-up events from 10^{-3} ($\sim \tau_{eff} 3 \mu s$) to 10^{-4} ($\sim \tau_{eff} 1.5 \mu s$), thus improving the neutrino mass sensitivity from 2 eV to about 1.4 eV. To put this result in perspective,

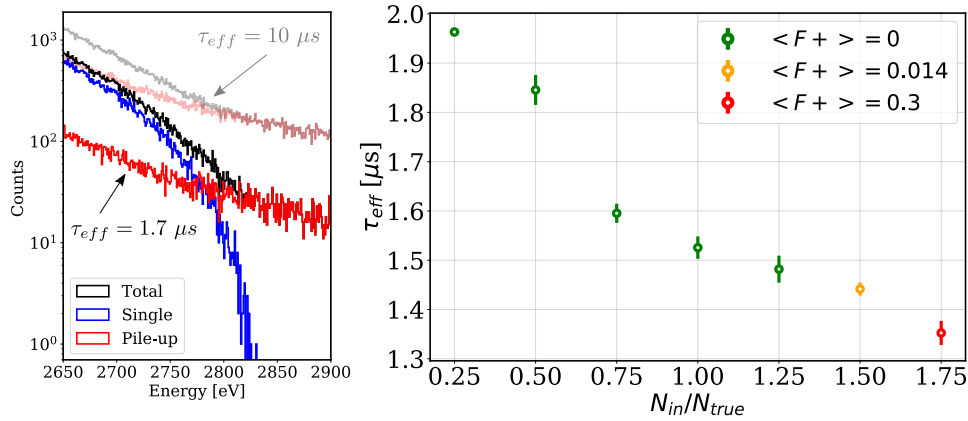


FIGURE 6.22: *Left*: ROI energy spectrum before and after the application of the WF/Volumetric cuts and the DSVP technique. Light line represents the energy spectrum with τ_{eff} of $10 \mu s$, while the solid line with a τ_{eff} of $1.7 \mu s$. *Right*: The dependence of τ_{eff} and the average percentage of false positive $F+$ from the input parameter N_B (N_{in}), which is normalized by the number of pile-up pulses present in the ROI (N_{true}).

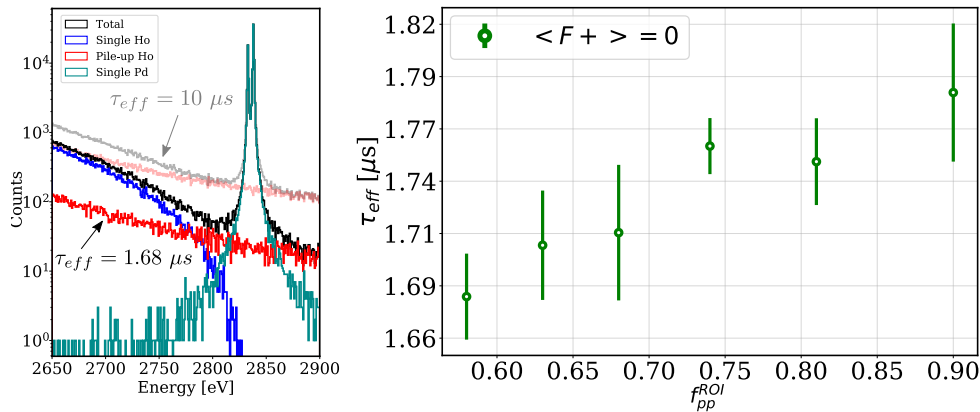


FIGURE 6.23: *Left*: ROI energy spectrum with Pd $L\alpha$ peaks before and after the application of the DSVP technique. The initial f_{pp}^{ROI} was set to 0.58. *Right*: The dependence of τ_{eff} from the f_{pp}^{ROI} is shown for the detector b . with a rise time of $17 \mu s$ and a sampling time of $2 \mu s$. In this case, N_B was equal to the number of pile-up pulses in the ROI.

achieving the same improvement would require to increase the acquisition time by a factor 4: from 3 to 12 years.

TABLE 6.3: Effective time resolution of the DSVP with Wiener Filter and Volumetric cuts. We indicated with (*) the algorithm used in that simulation to lower the ratio of f_{pp}^{ROI} below one. For simplicity, we always set N_B equal to the exact number of pile-up pulses in the ROI. The errors associated with the DSVP τ_{eff} are $\leq 5\%$ and are due to the random nature of the modified minimization RANSAC algorithm.

Detector type	Rise Time [μs]	t_{sample} [μs]	τ_{eff} Wiener Filter	τ_{eff} Volumetric cuts	τ_{eff} with DSVP
b.	11	2	2.26	2.12 (*)	1.55
b.	17	2	2.37 (*)	2.60	1.55
b.	22	2	2.94	2.90 (*)	2.01
b.	17	1	1.66 (*)	2.00	0.94
a.	10	2	1.82 (*)	-	1.24
c.	19	2	2.70 (*)	3.54	1.82

Chapter 7

Conclusions

Holmes is an ambitious project that aims to verify the feasibility of the calorimetric approach to the neutrino mass determination. This is necessary both to cross check the results of the current state of the art experiment, removing the influence of any systematic effects in the measurement, and to define a new way to probe the sub-eV neutrino mass scale.

Once the required number of recorded events is defined, the elements that are essential for the success of this technique can be summarized in the following. First, a high single pixel activity is necessary to keep the number of detectors manageable. This will also reduce the complexity of the data acquisition and analysis and decreasing the influence of the natural radioactivity and cosmic ray background on the experimental sensitivity. Second, the detectors need to show very good performance in terms of energy resolution and time response, presenting fast rising and falling edges.

These elements are strongly interconnected: the single pixel activity fixes the number of detectors, that in turn influences the readout bandwidth allocated per channel, which ultimately defines the pulse time profile that can be correctly sampled without spoiling the good energy resolution of the detector. This picture is further complicated by the fact that the number of Holmium nuclei implanted inside the detector absorber might potentially spoil its performances.

Holmes has adopted a high-risk/high-gain approach: with a target single pixel activity of 300 Bq the detectors and the readout will be tested to their technical limits, requiring also advanced discrimination techniques to decrease the resulting number of pile-up events.

Various fabrication steps are needed to implant the required amount of radioactive isotope inside the microcalorimeter absorbers: these needed to be tested at the beginning of this thesis work. I tuned the parameters of the target chamber in order to achieve the required uniform gold deposition with a rate of ~ 50 nm/h. As a result, about 20 hours of deposition will be necessary to enclose the ^{163}Ho between the two gold layers. I also successfully tested the KOH silicon etching procedure to homogeneously release the membrane on the detector array. After these procedures, the detectors response was checked in order to assess any variation of their performance compared to the ones fully fabricated at NIST. No significant differences were observed, at least due to the fabrications process under investigation and an energy resolution of 4.22 eV at ~ 6000 eV was achieved.

The Holmes readout is based on modules of 32 channels each. If one is able to correctly readout one single module, increasing the number of detectors is just a matter of increasing the number of modules. In this thesis, for the first time it was proven the capability of readout 32 detectors at the same time.

In its final phase, Holmes will deploy 1000 TES detectors. TES microcalorimeters detectors are sensitive thermometers that require a careful analysis pixel by pixel in order to preserve their excellent energy resolution. I developed a software for the analysis and the signal processing of microcalorimeters events, alongside a dedicated GUI for ease of use.

Different classes were written for the data reduction and for extracting the relevant parameters from the signals, while new routines were defined to correct the gain drift of the detectors. To speed the analysis up, most of these methods required little input from the user but for the most critical part an expert eye is still required.

The expected background contribution will change depending on the activity per pixel. If the activity is low (< 10 Bq, as expected in the first phase of Holmes) the background budget is expected to be dominated by natural radioactivity and cosmic rays, while for higher activity by pile-up events. In order to study the former, I performed a month long measurement. As a result, the background rate in the ROI is expected to be smooth and with a level lower than 1×10^{-4} counts $\text{eV}^{-1} \text{ day}^{-1} \text{ det}^{-1}$. This value is due to both the natural radioactivity in the detectors surrounding and cosmic rays. Thus, a further reduction on the total background rate of a factor of roughly 25% can be easily achieved by realizing an active muon veto similar to the one tested with this measurement.

For studying the pile-ups, I wrote a simulation routine to simulate and to solve the differential equations that describe the detectors response. The goal was to emulate the measured detector response in the energy range of interest. On the resulting simulated dataset, I tested two different algorithms for pile-up discrimination: a modified version of the Wiener Filter and a new technique based on the Singular Value Discrimination. The combined use of both technique seems to be a very powerful tool, and a time resolution of $\sim 1.5 \mu\text{s}$ with a sampling time of $2 \mu\text{s}$ was achieved.

The results of this work, both software and hardware, lays the grounds for the first phase of the Holmes experiment: a low dose implantation of a 2×32 pixel array. The influence of the ^{163}Ho on the detector response will be assessed, and a resolute calorimetric spectrum of the ^{163}Ho decay will be produced that should help to validate or disprove the different theoretical models. A first limit on the neutrino mass will be reached of the order of $\mathcal{O}(10)$ eV.

Upon these results, it will be clear how much activity per pixel can be implanted inside the detector and thus if the calorimetric approach can still be considered a feasible way to reach the required sub-eV sensitivity on the neutrino mass.

Bibliography

- [1] Clyde L Cowan Jr, Frederick Reines, FB Harrison, HW Kruse, and AD McGuire. Detection of the free neutrino: a confirmation. *Science*, 124(3212):103–104, 1956.
- [2] Raymond Davis Jr, Don S Harmer, and Kenneth C Hoffman. Search for neutrinos from the sun. *Physical Review Letters*, 20(21):1205, 1968.
- [3] John N Bahcall, Neta A Bahcall, and Giora Shaviv. Present status of the theoretical predictions for the cl 37 solar-neutrino experiment. *Physical Review Letters*, 20(21):1209, 1968.
- [4] Angelo Nucciotti. The use of low temperature detectors for direct measurements of the mass of the electron neutrino. *Advances in High Energy Physics*, 2016, 2016.
- [5] The SLD Electroweak, Heavy Flavour Groups, ALEPH Collaboration, DELPHI Collaboration, L3 Collaboration, OPAL Collaboration, SLD Collaboration, LEP Electroweak Working Group, et al. Precision electroweak measurements on the z resonance. *Physics Reports*, 427(5-6):257–454, 2006.
- [6] C Athanassopoulos, LB Auerbach, RL Burman, DO Caldwell, ED Church, I Cohen, JB Donahue, A Fazely, FJ Federspiel, GT Garvey, et al. Evidence for $\nu_{\mu} \rightarrow \nu_e$ neutrino oscillations from lsnd. *arXiv preprint nucl-ex/9709006*, 1997.
- [7] AA Aguilar-Arevalo, CE Anderson, SJ Brice, BC Brown, L Bugel, JM Conrad, R Dharmapalan, Z Djurcic, BT Fleming, R Ford, et al. Event excess in the miniboone search for $\nu_{\mu} \rightarrow \nu_e$ oscillations. *Physical review letters*, 105(18):181801, 2010.
- [8] G Mention, M Fechner, Th Lasserre, Th A Mueller, D Lhuillier, M Cribier, and A Loutourneau. Reactor antineutrino anomaly. *Physical Review D*, 83(7):073006, 2011.
- [9] Jan Hamann, Steen Hannestad, Georg G Raffelt, Irene Tamborra, and Yvonne YY Wong. Cosmology seeking friendship with sterile neutrinos. *Nuclear Physics B- Proceedings Supplements*, 217(1):72–74, 2011.
- [10] Peter Minkowski. $\mu \rightarrow e\gamma$ at a rate of one out of 109 muon decays? *Physics Letters B*, 67(4):421–428, 1977.
- [11] Joachim Kopp, Pedro AN Machado, Michele Maltoni, and Thomas Schwetz. Sterile neutrino oscillations: the global picture. *Journal of High Energy Physics*, 2013(5):1–52, 2013.
- [12] Pablo Fernández de Salas, DV Forero, Christoph Andreas Ternes, Mariam Tórtola, and José WF Valle. Status of neutrino oscillations 2018: 3σ hint for normal mass ordering and improved cp sensitivity. *Physics Letters B*, 782:633–640, 2018.
- [13] Fengpeng An, Guangpeng An, Qi An, Vito Antonelli, Eric Baussan, John Beacom, Leonid Bezrukov, Simon Blyth, Riccardo Brugnera, Margherita Buizza Avanzini, et al. Neutrino physics with junos. *Journal of Physics G: Nuclear and Particle Physics*, 43(3):030401, 2016.

- [14] Steen Hannestad. Neutrinos in cosmology. *New Journal of Physics*, 6(1):108, 2004.
- [15] Zoltan Fodor, Sandor D Katz, and Andreas Ringwald. Relic neutrino masses and the highest energy cosmic rays. *Journal of High Energy Physics*, 2002(06):046, 2002.
- [16] Nabila Aghanim, Yashar Akrami, Mark Ashdown, J Aumont, C Baccigalupi, M Ballardini, AJ Banday, RB Barreiro, N Bartolo, S Basak, et al. Planck 2018 results-vi. cosmological parameters. *Astronomy & Astrophysics*, 641:A6, 2020.
- [17] Michelle J Dolinski, Alan WP Poon, and Werner Rodejohann. Neutrinoless double-beta decay: status and prospects. *Annual Review of Nuclear and Particle Science*, 69: 219–251, 2019.
- [18] Kai Zuber. *Neutrino physics*. Taylor & Francis, 2003.
- [19] EG Myers, A Wagner, H Kracke, and BA Wesson. Atomic masses of tritium and helium-3. *Physical review letters*, 114(1):013003, 2015.
- [20] Ch Kraus, B Bornschein, L Bornschein, J Bonn, B Flatt, A Kovalik, B Ostrick, EW Otten, JP Schall, Th Thümmler, et al. Final results from phase ii of the mainz neutrino mass search in tritium decay. *The European Physical Journal C-Particles and Fields*, 40(4): 447–468, 2005.
- [21] VN Aseev, AI Belesev, AI Berlev, EV Geraskin, AA Golubev, NA Likhovid, VM Lobashev, AA Nozik, VS Pantuev, VI Parfenov, et al. Upper limit on the electron antineutrino mass from the troitsk experiment. *Physical Review D*, 84(11):112003, 2011.
- [22] A Osipowicz, H Blümer, and G Drexlin. Katrin-a next generation tritium beta decay experiment with sub-ev sensitivity for the electron neutrino mass. Technical report, Forschungszentrum Karlsruhe GmbH Technik und Umwelt (Germany). Inst. fuer . . . , 2001.
- [23] FM Fränkle, Anna Schaller, Christian Weinheimer, Guido Drexlin, Susanne Mertens, Klaus Blaum, Ernst Otten, Volker Hannen, Lutz Bornschein, Joachim Wolf, et al. Katrin background due to surface radioimpurities. *arXiv preprint arXiv:2011.05107*, 2020.
- [24] Max Aker, K Altenmüller, M Arenz, M Babutzka, J Barrett, S Bauer, M Beck, A Beglarian, J Behrens, T Bergmann, et al. Improved upper limit on the neutrino mass from a direct kinematic method by katrin. *Physical review letters*, 123(22):221802, 2019.
- [25] JA Formaggio, Project 8 Collaboration, et al. Project 8: using radio-frequency techniques to measure neutrino mass. *Nuclear Physics B-Proceedings Supplements*, 229:371–375, 2012.
- [26] de Viveiros Luiz. Project 8: A neutrino mass experiment using cyclotron radiation emission spectroscopy, aps mid-atlantic section fall meeting 2020. Technical report, 2020.
- [27] A Ashtari Esfahani, Vikas Bansal, S Böser, N Buzinsky, Raphael Cervantes, C Claessens, Luiz de Viveiros, Peter J Doe, M Fertl, JA Formaggio, et al. Electron radiated power in cyclotron radiation emission spectroscopy experiments. *Physical Review C*, 99(5):055501, 2019.
- [28] Ali Ashtari Esfahani, David M Asner, Sebastian Böser, Raphael Cervantes, Christine Claessens, Luiz De Viveiros, Peter J Doe, Shepard Doleman, Justin L Fernandes, Martin Fertl, et al. Determining the neutrino mass with cyclotron radiation emission

- spectroscopy—project 8. *Journal of Physics G: Nuclear and Particle Physics*, 44(5):054004, 2017.
- [29] JJ Simpson. Measurement of the β -energy spectrum of ^3H to determine the antineutrino mass. *Physical Review D*, 23(3):649, 1981.
- [30] Alvaro De Rújula. A new way to measure neutrino masses. *Nuclear Physics B*, 188(3):414–458, 1981.
- [31] P Filianin, Chunhai Lyu, M Door, K Blaum, WJ Huang, M Haverkort, P Indelicato, CH Keitel, K Kromer, D Lange, et al. Direct q -value determination of the β -decay of ^{187}Re . *Physical Review Letters*, 127(7):072502, 2021.
- [32] Massimiliano Galeazzi, F Fontanelli, F Gatti, and S Vitale. End-point energy and half-life of the ^{187}Re β decay. *Physical Review C*, 63(1):014302, 2000.
- [33] M Sisti, C Arnaboldi, C Brofferio, G Ceruti, O Cremonesi, E Fiorini, A Giuliani, Benno Margesin, L Martensson, A Nucciotti, et al. New limits from the milano neutrino mass experiment with thermal microcalorimeters. *Nuclear Instruments and Methods in Physics Research Section A: Accelerators, Spectrometers, Detectors and Associated Equipment*, 520(1-3):125–131, 2004.
- [34] Steven E Koonin. Environmental fine structure in low-energy β -particle spectra. *Nature*, 354(6353):468–470, 1991.
- [35] Sergey Eliseev, Klaus Blaum, M Block, S Chenmarev, H Dorrer, Ch E Düllmann, C Enss, PE Filianin, L Gastaldo, Mikhail Goncharov, et al. Direct measurement of the mass difference of ^{163}Ho and ^{163}Dy solves the q -value puzzle for the neutrino mass determination. *Physical review letters*, 115(6):062501, 2015.
- [36] Alvaro De Rújula and Maurizio Lusignoli. Calorimetric measurements of $^{163}\text{holmium}$ decay as tools to determine the electron neutrino mass. *Physics Letters B*, 118(4-6):429–434, 1982.
- [37] CL Bennett, AL Hallin, RA Naumann, PT Springer, MS Witherell, RE Chrien, PA Baisden, and DH Sisson. The x-ray spectrum following ^{163}Ho m electron capture. *Physics Letters B*, 107(1-2):19–22, 1981.
- [38] Alvaro De Rújula and Maurizio Lusignoli. Single electron ejection in electron capture as a tool to measure the electron neutrino mass. *Nuclear Physics B*, 219(2):277–301, 1983.
- [39] L Gastaldo, Klaus Blaum, Andreas Dörr, Ch E Düllmann, K Eberhardt, Sergey Eliseev, C Enss, Amand Faessler, A Fleischmann, S Kempf, et al. The electron capture ^{163}Ho experiment echo. *Journal of Low Temperature Physics*, 176(5):876–884, 2014.
- [40] B Alpert, M Balata, D Bennett, M Biasotti, C Boragno, Chiara Brofferio, V Ceriale, D Corsini, Peter Kenneth Day, M De Gerone, et al. Holmes. *The European Physical Journal C*, 75(3):1–11, 2015.
- [41] Z Ge, T Eronen, KS Tyrin, J Kotila, J Kostensalo, DA Nesterenko, O Beliuskina, R de Groote, A de Roubin, S Geldhof, et al. ^{159}Dy electron-capture: A new candidate for neutrino mass determination. *Physical Review Letters*, 127(27):272301, 2021.
- [42] Amand Faessler, Christian Enss, Loredana Gastaldo, and F Šimkovic. Determination of the neutrino mass by electron capture in ^{163}Ho and the role of the three-hole states in ^{163}Dy . *Physical Review C*, 91(6):064302, 2015.

- [43] RGH Robertson. Examination of the calorimetric spectrum to determine the neutrino mass in low-energy electron capture decay. *Physical Review C*, 91(3):035504, 2015.
- [44] A De Rújula and M Lusignoli. The calorimetric spectrum of the electron-capture decay of ^{163}Ho : the spectral endpoint region. *Journal of High Energy Physics*, 2016(5): 1–26, 2016.
- [45] M Braß, C Enss, L Gastaldo, RJ Green, and MW Haverkort. Ab initio calculation of the calorimetric electron-capture spectrum of ^{163}Ho : Intra-atomic decay into bound states. *Physical Review C*, 97(5):054620, 2018.
- [46] M Braß and MW Haverkort. Ab initio calculation of the electron capture spectrum of ^{163}Ho : Auger–meitner decay into continuum states. *New Journal of Physics*, 22(9): 093018, 2020.
- [47] Maurizio Lusignoli and Marco Vignati. Relic antineutrino capture on ^{163}Ho decaying nuclei. *Physics Letters B*, 697(1):11–14, 2011.
- [48] PC-O Ranitzsch, C Hassel, M Wegner, S Kempf, A Fleischmann, C Enss, L Gastaldo, A Herlert, and K Johnston. First calorimetric measurement of oi-line in the electron capture spectrum of ^{163}Ho . *arXiv preprint arXiv:1409.0071*, 2014.
- [49] C Velte, F Ahrens, A Barth, K Blaum, M Braß, Menno Door, H Dorrer, Ch E Düllmann, S Eliseev, C Enss, et al. High-resolution and low-background ^{163}Ho spectrum: interpretation of the resonance tails. *The European Physical Journal C*, 79(12):1–8, 2019.
- [50] Angelo Nucciotti. Statistical sensitivity of ^{163}Ho electron capture neutrino mass experiments. *The European Physical Journal C*, 74(11):1–6, 2014.
- [51] A Nucciotti, E Ferri, and O Cremonesi. Expectations for a new calorimetric neutrino mass experiment. *Astroparticle Physics*, 34(2):80–89, 2010.
- [52] Kent D Irwin and Gene C Hilton. Transition-edge sensors. *Cryogenic particle detection*, pages 63–150, 2005.
- [53] Joel N Ullom and Douglas A Bennett. Review of superconducting transition-edge sensors for x-ray and gamma-ray spectroscopy. *Superconductor Science and Technology*, 28(8):084003, 2015.
- [54] A Kozorezov, Alexandre Avraamovitch Golubov, DDE Martin, PAJ de Korte, Mark A Lindeman, RA Hijmering, J van der Kuur, HFC Hoovers, L Gottardi, M Yu Kupriyanov, et al. Modelling the resistive state in a transition edge sensor. *Applied physics letters*, 99(6):063503, 2011.
- [55] WJ Skocpol, MR Beasley, and M Tinkham. Phase-slip centers and nonequilibrium processes in superconducting tin microbridges. *Journal of Low Temperature Physics*, 16(1):145–167, 1974.
- [56] GR Berdiyrov, AK Elmurodov, FM Peeters, and DY Vodolazov. Finite-size effect on the resistive state in a mesoscopic type-II superconducting stripe. *Physical Review B*, 79(17):174506, 2009.
- [57] Kent D Irwin, Gene C Hilton, David A Wollman, and John M Martinis. Thermal-response time of superconducting transition-edge microcalorimeters. *Journal of Applied Physics*, 83(8):3978–3985, 1998.

- [58] Douglas A Bennett, Daniel S Swetz, Robert D Horansky, Daniel R Schmidt, and Joel N Ullom. A two-fluid model for the transition shape in transition-edge sensors. *Journal of Low Temperature Physics*, 167(3):102–107, 2012.
- [59] M Tinkham. The interaction of phase-slip centers in superconducting filaments. *Journal of Low Temperature Physics*, 35(1):147–151, 1979.
- [60] Douglas A Bennett, Daniel R Schmidt, Daniel S Swetz, and Joel N Ullom. Phase-slip lines as a resistance mechanism in transition-edge sensors. *Applied Physics Letters*, 104(4):042602, 2014.
- [61] B Cabrera. Introduction to tes physics. *Journal of Low Temperature Physics*, 151(1):82–93, 2008.
- [62] DT Becker, Douglas A Bennett, M Biasotti, M Borghesi, V Ceriale, M De Gerone, M Faverzani, E Ferri, JW Fowler, G Gallucci, et al. Working principle and demonstrator of microwave-multiplexing for the holmes experiment microcalorimeters. *Journal of Instrumentation*, 14(10):P10035, 2019.
- [63] John Arthur Benson Mates. *The microwave SQUID multiplexer*. PhD thesis, University of Colorado, 2011.
- [64] B Alpert, D Becker, D Bennet, M Biasotti, M Borghesi, G Gallucci, M De Gerone, M Faverzani, E Ferri, J Fowler, et al. High-resolution high-speed microwave-multiplexed low temperature microcalorimeters for the holmes experiment. *The European Physical Journal C*, 79(4):1–8, 2019.
- [65] Joel N Ullom, William B Doriese, Gene C Hilton, James A Beall, Steven Deiker, WD Duncan, L Ferreira, Kent D Irwin, Carl D Reintsema, and Leila R Vale. Characterization and reduction of unexplained noise in superconducting transition-edge sensors. *Applied Physics Letters*, 84(21):4206–4208, 2004.
- [66] T Kühn and IJ Maasilta. Maximizing phonon thermal conductance for ballistic membranes. In *Journal of Physics: Conference Series*, volume 92, page 012082. IOP Publishing, 2007.
- [67] James P Hays-Wehle, Daniel R Schmidt, Joel N Ullom, and Daniel S Swetz. Thermal conductance engineering for high-speed tes microcalorimeters. *Journal of Low Temperature Physics*, 184(1):492–497, 2016.
- [68] Ilari J Maasilta. Complex impedance, responsivity and noise of transition-edge sensors: Analytical solutions for two-and three-block thermal models. *Aip Advances*, 2(4):042110, 2012.
- [69] M Krusius, AC Anderson, and B Holmström. Calorimetric investigation of hyperfine interactions in metallic ho and tb. *Physical Review*, 177(2):910, 1969.
- [70] K Prasai, E Alves, D Bagliani, S Basak Yanardag, M Biasotti, M Galeazzi, F Gatti, M Ribeiro Gomes, J Rocha, and Y Uprety. Thermal properties of holmium-implanted gold films. *Journal of low temperature physics*, 176(5-6):979–985, 2014.
- [71] Matthew Herbst, Andreas Reifenberger, Clemens Velte, Holger Dorrer, Christoph E Düllmann, Christian Enss, Andreas Fleischmann, Loredana Gastaldo, Sebastian Kempf, Tom Kieck, et al. Specific heat of holmium in gold and silver at low temperatures. *Journal of Low Temperature Physics*, 202(1):106–120, 2021.

- [72] P Sortais, T Lamy, J Médard, J Angot, L Latrasse, and T Thuillier. Ultracompact/ultralow power electron cyclotron resonance ion source for multipurpose applications. *Review of Scientific Instruments*, 81(2):02B314, 2010.
- [73] Joseph W Fowler, Bradley K Alpert, William B Doriese, DA Fischer, Chemo Jaye, Young-Il Joe, GC O’Neil, DS Swetz, and JN Ullom. Microcalorimeter spectroscopy at high pulse rates: A multi-pulse fitting technique. *The Astrophysical Journal Supplement Series*, 219(2):35, 2015.
- [74] Matteo Borghesi, Marco Faverzani, Cecilia Ferrari, Elena Ferri, Andrea Giachero, Angelo Nucciotti, and Luca Origo. The matrix optimum filter for low temperature detectors dead-time reduction. *arXiv preprint arXiv:2201.05549*, 2022.
- [75] Kelsey M Morgan, Daniel T Becker, Douglas A Bennett, Johnathon D Gard, Jozsef Imrek, JAB Mates, Christine G Pappas, Carl D Reintsema, Daniel R Schmidt, Joel N Ullom, et al. Expanding the capability of microwave multiplexed readout for fast signals in microcalorimeters. *Journal of low temperature physics*, pages 1–7, 2019.
- [76] Joseph W Fowler, Christine G Pappas, Bradley K Alpert, William B Doriese, Galen C O’Neil, Joel N Ullom, and Daniel S Swetz. Approaches to the optimal nonlinear analysis of microcalorimeter pulses. *Journal of Low Temperature Physics*, 193(3):539–546, 2018.
- [77] Emilio Gatti and Pier Francesco Manfredi. Processing the signals from solid-state detectors in elementary-particle physics. *La Rivista del Nuovo Cimento (1978-1999)*, 9(1):1–146, 1986.
- [78] Marco Andrea Carrettoni. *Data analysis for neutrinoless double beta decay*. PhD thesis, Citeseer, 2011.
- [79] Alan V Oppenheim and George C Verghese. *Signals, systems and inference*. Pearson, 2015.
- [80] M Borghesi, M De Gerone, M Faverzani, M Fedkevych, E Ferri, G Gallucci, A Giachero, A Nucciotti, and A Puiu. A novel approach for nearly-coincident events rejection. *The European Physical Journal C*, 81(5):1–9, 2021.
- [81] B. Alpert et al. Algorithms for Identification of Nearly-Coincident Events in Calorimetric Sensors. *J. Low. Temp. Phys.*, 184(1-2):263–273, 2016. doi: 10.1007/s10909-015-1402-y.
- [82] Paolo Carniti, Lorenzo Cassina, Marco Faverzani, Elena Ferri, Andrea Giachero, Claudio Gotti, Matteo Maino, Angelo Nucciotti, Gianluigi Pessina, and Andrei Puiu. Transformer coupling and its modelling for the flux-ramp modulation of rf-squids. *Instruments*, 3(1):3, 2019.
- [83] H Akamatsu, D Vaccaro, L Gottardi, J Van Der Kuur, CP De Vries, Mikko Kiviranta, Kevin Ravensberg, M D’Andrea, E Taralli, M De Wit, et al. Demonstration of mhz frequency domain multiplexing readout of 37 transition edge sensors for high-resolution x-ray imaging spectrometers. *Applied Physics Letters*, 119(18):182601, 2021.
- [84] Elena Ferri, B Alpert, D Bennett, Marco Faverzani, J Fowler, Andrea Giachero, J Hays-Wehle, Matteo Maino, A Nucciotti, A Puiu, et al. Pile-up discrimination algorithms for the holmes experiment. *Journal of Low Temperature Physics*, 184(1):405–411, 2016.

-
- [85] Sala. Development of low level counting systems for high sensitivity measurements. 2014.
- [86] Particle Data Group et al. Review of particle physics. *Journal of Physics G: Nuclear and particle physics*, 33(1):001, 2006.
- [87] Pall Theodorsson. *Measurement of weak radioactivity*. World scientific, 1996.
- [88] Giulio D’agostini. *Bayesian reasoning in data analysis: A critical introduction*. World Scientific, 2003.
- [89] Andrew Gelman, Daniel Lee, and Jiqiang Guo. Stan: A probabilistic programming language for bayesian inference and optimization. *Journal of Educational and Behavioral Statistics*, 40(5):530–543, 2015.
- [90] Bradley Alpert, Elena Ferri, Douglas Bennett, Marco Faverzani, Joseph Fowler, Andrea Giachero, James Hays-Wehle, Matteo Maino, A Nucciotti, A Puiu, et al. Algorithms for identification of nearly-coincident events in calorimetric sensors. *Journal of low temperature physics*, 184(1):263–273, 2016.